THERMAL STRIPING

An experimental investigation on mixing of jets.

Part Ⅲ : Remaining hydrodynamic results from initial experiments

(Research Report)

June, 1999

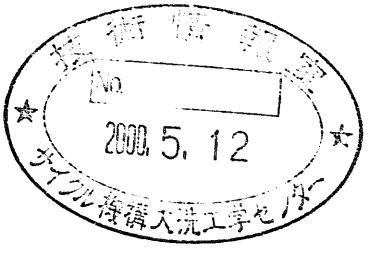

Japan Nuclear Cycle Development Institute

O-arai Engineering Center

Ⓚ

THERMAL STRIPING

An experimental investigation on mixing of jets.
Part III: Remaining hydrodynamic results from initial experiments

A. T. Tokuhiro[1], N. Kimura[2], H. Miyakoshi[2]

Abstract

Experiments were performed using the WAJECO facility to investigate the thermohydraulic mixing of multiple jets flowing out of a LMFBR core. Mixing is the root of the thermal striping problem. The multiple jets are typically at different velocities and temperatures and may induce thermal stresses upon components they impinge. In our study we modeled the mixing of three vertical jets, the central at a lower temperature than the two adjacent jets at equal temperatures. The jets are quasi-planar. The parameters were the average exit jet velocities ($U_{o,av}$) and the temperature difference between the "cold" and "hot" jets ($\Delta T_{hc}=T_{hot}-T_{cold}$). Measurements of the liquid velocity, initially using laser Doppler velocimetry (LDV) and later ultrasound Doppler velocimetry (UDV), for both our *reference* single-jet and the triple-jet configuration, comprised Phase I of the experiments (up to 1994). Two reports (TN9410 96-181 and TN9410 96-296; in Japanese) reported on the hydraulic and heat transfer aspects. This is the final report of Phase I data.

From a *hydrodynamic* perspective, our single-jet data behaved in satisfactory agreeeent with past single-jet data. By comparison, the triple-jet exhibited, for both equal/unequal average exit velocities, a convergence of the right and left jets upon the central jet, accompanied by side-to-

---

[1] JNC International Fellow, Reactor Engineering Group, Oarai Engineering Center

[2] Reactor Engineering Group, Oarai Engineering Center

side oscillation of all three jets that initiated the mixing of the jets. In particular, the flow fluctuations as expressed by the root-mean-square (*rms*) velocities were enhanced in between the hot and cold jets. For the isovelocity case ($r=U_{cold}/U_{hot}=1$), given at $U_{o,av}$ =0.5 m/s and ΔT_{hc} =5°C, we found the mixing predominantly takes place at z/D_h = 2.0 to 4.5, where D_h is the hydraulic diameter of the exit nozzle. Spanwise this mixing takes place over $x/D_h \sim 2.25$, centered about the "cold" jet. The dominant frequency of oscillation was f=2.25Hz in the mixing zone and 0.7Hz in the post-mixing region. Non-isovelocity axially delays the initiation of convective mixing, but mixing does occur. The post-mixing temperature was higher in these cases. Non-isovelocity dispersed the frequency of fluctuations; however,mostly in between $2.2<f<2.3$ Hz. Finally, the flow fluctuations remained further downstream for ΔT_{hc}=5°C, than the ΔT_{hc} =0°C case.

１９９９年６月

サーマルストライピングを対象とした噴流間混合現象に関する実験研究 －フェーズ１試験結果に関する第３報－ (研究報告書)

A. Tokuhiro[1]、木村　暢之[2]、宮越　博幸[2]

要旨

高速炉のサーマルストライピング現象について熱流動に関する実験シリーズが水流動試験装置を用いて行われた。ここで言うサーマルストライピング現象とは、炉心出口部において、制御棒チャンネルや集合体から流出する温度・速度の異なる噴流が十分に混合せずに炉心上部構造材に衝突することにより構造材に熱疲労を与える現象である。

本試験体系は、鉛直噴流を平行に３本配置しており、中心噴流が低温、左右の噴流が高温である。噴流は、矩形ノズルから試験容器中に準２次元形状で吐出している。試験パラメータは、噴流の平均吐出流速（$U_{o,av}$）と中心噴流と周辺噴流の吐出温度差（$\Delta T_{hc}=T_{hot}-T_{cold}$）である。流速測定はレーザードップラー流速計（LDV）と超音波流速計（UDV）を用いて行った。本試験は、中心噴流を吐出させた単一噴流条件と３本の矩形噴流を吐出させた三噴流条件で行った。第１報は主にUDV計測結果、第２報は主に温度計測結果をまとめ、これらの結果を踏まえ、本報においてフェーズ１試験のまとめを行った。

単一噴流条件における流速測定結果は、噴流出口領域から下流において、LDVとUDVとも既知の試験結果と良い一致を示した。

三噴流試験条件において、３つの噴流の吐出速度が等速の場合、噴流が左右に振動することにより対流混合が行われていることが明らかとなった。また、速度変動は、流れに垂直方向において、左右の噴流と中心噴流の間の領域で大きくなっていることがわかった。UDVによる速度変動および温度変動から得られた噴流振動の卓越周波数は、噴流が主に混合する領域（混合領域）で f=2.25Hz、噴流の混合がほぼ終了した領域では f=0.7Hz であった。

左右の噴流吐出速度が中心噴流吐出速度より大きい場合、混合領域が下流側にシフトし、混合領域の流れ方向長さが短くなっていることがわかった。

[1]大洗工学センター　ナトリウム・安全工学試験部　原子炉工学グループ
国際特別研究員

[2]大洗工学センター　ナトリウム・安全工学試験部　原子炉工学グループ

Contents

I. Introduction 1

II. Experiment 3

II.1 Experimental facility 3
II.1.1 Ultrasound Velocity Profile monitor (UVP), (ultrasound Doppler velocimeter) 4
II.2.2. Laser Doppler Velocimeter (LDV) 5
II.2 Experimental test cases 6
II.2.1 Conditions of LDA measurements 6
II.2.2 Conditions of UVP measurements 6

III. Results and discussion 7

III.1 Flow visualization data: photographs and video images 7
III.2 Single-jet velocity data 8
III.2.1 Average exit velocity U_0=1.0 [m/s] 8
III.2.2 Average exit velocity U_0=2.0 [m/s] 10
III.2.3 Single-jet calculated vector field 13

III.3 Triple-jet velocity data
III.2.1 Triple-jet calculated vector field 14
III.2.2 Triple-jet with ΔT_{hc}=5°C and ΔT_{hc}=0° 14
III.2.3 Triple-jet axial component and trends 16
III.2.4 Triple-jet spectral data 19

IV. Summary and conclusions 20

Nomenclature 23
Greek Symbols 23

References 24

Acknowledgments 26

Appendix A Ultrasound Doppler velocimetry principles and UVP operational parameters 73

Appendix B Specifications of Expancel 091-80 tracer particle 79

Appendix C Table of documented photographs and video prints 80

Appendix D A brief review of fundamental jet parameters 81

Appendix E List and short description of test cases 84

List of Tables

Table 1. Summary of single- and triple-jet cases for which UDV data was taken 28

Table 2. Experimental conditions 29

List of Figures

II. Experiment
II.1 Experimental facility

Figure 1. Schematic of experimental loop 30

Figure 2. Schematic of experimental apparatus 31

Figure 3. Schematic of instrumentation set-up. Close-up of the UVP transducer orientation and traversing thermocouple array 32

Figure 4. Flow visualization of single-jet. One digitized frame of cases noted 33

Figure 5. Flow visualization of triple-jet. One digitized frame of cases noted 34

Figure 6. Flow visualization of triple-jet. One digitized frame of cases noted 35

Figure 7. Digitized images of the triple-jet at 1/15th-0f-a-second intervals under different $U_{cold,exit}$, $U_{hot,exit}$ and $T_{hc}(=T_{hot}-T_{cold})$ conditions 36

Figure 8. Vector plot of the single-jet superimposed on its magnitude 37

Figure 9. Vector plot of the single-jet superimposed on its magnitude in color 38

Figure 10. Average velocity profiles with axial distance as parameter 39

Figure 11. Average velocity profiles with axial distance as parameter....40

Figure 12. Average standard deviation of velocity profiles with axial distance as parameter....41

Figure 13. Average standard deviation of velocity profiles with axial distance as parameter....42

Figure 14. Spanwise profiles of Uy-component of average velocity....43

Figure 15. Comparison of velocity profiles taken by LDA and UVP at selected axial locations....44

Figure 16. Decay of the centerline velocity defined as the ratio of average exit to maximum centerline velocities, U_o/U_m, versus axial distance.... 45

Figure 17. Comparison of jet half-radii from present and past experiments 46

Figure 18. Radial velocity of a planar jet versus Kataoka's axisymmtricjet correlations....47

Figure 19. Jet half-radius versus axial location, calculated from far-field UVP measurments....48

Figure 20(a). Axial development of estimated "mass-flux" of single-jet....49

Figure 20(b). Axial development of the estimated"mass-flux" beyond the core length....50

Figure 21. Calculated composite "average"vector field for a single-jet....51

Figure 22. Calculated vector field superimposed on isocontours....52

Figure 23. Calculated vector field for a triple-jet, superimposed on isocontours....53

Figure 24. Magnitude of velocity of the triple-jet in grayscale....54

Figure 25(a). Standard deviation of velocity, of the transverse component, superimposed on isocontours of its magnitude with ΔT_{hc}=5°C....55

Figure 25(b). Standard deviation of velocity, of the transverse component, superimposed on isocontours of its magnitude with ΔT_{hc}=0°C....56

Figure 26. Difference in standard deviation of velocity, of the transverse component, superimposed on isocontours of its magnitude; [ΔT_{hc}=5°C - ΔT_{hc}=0°C]....57

Figure 27(a). Difference in the normalized transverse velocity component at selected axial locations....58

Figure 27(b). Difference in the normalized transverse velocity component at selected axial locations....58

Figure 28(a). Spanwise difference in normalized SD at various axial locations with and without jet-to-jet temperature difference (dT5-dT0)....59

Figure 28(b). Spanwise difference in normalized SD at various axial locations with and without jet-to-jet temperature difference (dT5-dT0)....60

Figure 29. Differences in normalized axial U_{avg} and SD of the central jet in triple- and single-jet configurations....61

Figure 30. A schematic of the approximate flow development for the triple-jet with and without temperature difference....62

Figure 31. Differences in normalized axial U_{avg} and SD of the central jet in triple- and single-jet configurations....63

Figure 32. Change in the axial average velocity and its deviation for x=0 to 85 mm from the exit....64

Figure 33. Comparison of 20 pt average velocity and SD components against that measured from the side (left)....65

Figure 34. Axial distribution of the average velocity with and without jet-to-jet temperature difference....66

Figure 35. Axial distribution of the average standard deviation (SD) with and without jet-to-jet temperature difference....67

Figure 36. Average differences in normalied Uavg and SD versus axial distance with and without jet-tc-jet temperature difference 68

Figure 37. Comparison of average velocity versus axial location for single- and triple-jets 69

Figure 38. Comparison of normalized RMS versus axial distance z/D for single- and triple-jets 70

Figure 39. Normalized frequency of spanwise velocity component versus axial distance for dT=0C 71

Figure 40. Normalized frequency of spanwise velocity component versus axial distance for dT=5C 72

as of June 9, 1999

I. Introduction

In Part I of this work we mentioned that "thermal striping" was the thermal cycling of reactor structures such as the UIS (upper instrument structure), as a result of fluid-structure, thermal interaction. That is, the rather random convective and conductive heat transfer from hot and cold streams of coolant to solid structures and components. The term "striping" originates from a description of the hot and cold (thermal) *stripes* that a component must withstand, under impingement of *preferentially and/or inefficiently* mixed coolant flowing through and exiting the reactor core. The net result of this striping is undesirable since *thermal fatigue* of materials can lead to failure of specific components and structures. This being the case, thermal striping as a phenomenological problem in LMFBRs was already recognized in the early 1980s (and probably earlier) by Wood (1980), Burnings (1982) and has been given further consideration, for example, by Betts, Bourman and Sheriff (1983), Betts et al. (1988), Moriya et al. (1988), Moriya et al. (1991), Muramatsu (1994*a* and *b*), Tokuhiro, Kimura and Miyakoshi (1997) and Kimura, Tokuhiro and Miyakoshi (1997).

In LMFBR research, it has since been considered in a simplified geometry by Tenchine and Nam (1987), who investigated a coaxial sodium jet and Tenchine and Moro (1995), who further compared the results of sodium and air mixing jet experiments. We note here that, although the phenomena taken as a whole involve fluid-structure interaction, the analytical and experimental efforts have generally been divided into distinct structural and thermal-hydraulic investigations. In this report, we focus strictly on the thermal-hydraulic aspects; that is, mainly the *convective mixing* phenomena of a multiple number of jets at different velocities and temperatures. By *convective mixing* we mean the thermal transport processes of relevance in thermal striping; that is, the momentum and energy transport, the former described by hydrodynamics and the latter represented by thermal-hydraulics or convective heat transfer. It is obvious that jets of the same species (since jets can be of different species), at different temperatures, have different densities such that these types of flows may also be called *density-stratified or thermally-stratified* jets. The number of jets can range from a single-jet, which has been most extensively studied, to two jets flowing side-by-side, at a relative angle or co-axially and with a relative velocity (and/or temperature as assumed) to each other. Investigation of more than two jets seems to be rare. Therefore besides its relevance to LMFBR thermal-hydraulics, a study of a multiple number of vertical jets discharging into a larger volume (above it) of the same fluid, at either the same or different density (temperature), contributes to the knowledge base of convective heat transfer. The fundamental aspects of single-jets, often axisymmetric but also planar (2D) and of relevance to LMFBR are such topics as: 1) impinging jets, 2) jets in cross flow, 3) jet mixing in tanks and 4) turbulent mixing and diffusion of jets and 5) modeling of turbulent jets. These topics are contained in such reference books as Cheremisinoff (1986) [jets] and Gebhardt et al. (1988) [jets and plumes]. Finally, since a large volume often represents an upper or lower plenum it may also contain structures and

components, which then contribute additional boundary constraints to the flow exiting from a thermal source, while the multiple number of jets simulate the flow out of the core and subassemblies.

In the present study, we carried out water-based experiments in a test facility simulating the mixing of one centrally located, unheated jet sandwiched by two adjacent, heated jets. Since there was a temperature difference between the heated and unheated jets, the unheated jet is referred to as the "cold jet" and the heated, the "hot jet". Buoyancy of the heated jet was not a major factor as the inertial effects dominated convective heat transfer. The three jets were injected into a large tank initially at the same temperature as the cold jet. The exit geometry of the jet nozzle consisted of three identical rectangular slots protruding out of the bottom surface of a rectangular tank and defined by four rectangular blocks. The front and back portions of the exits were blocked by fixing end-plates to the blocks so that the jets were constrained to flow out in a quasi-planar jet configuration.

As for the information we hope to gain from the present thermal-striping experiment, these are several-fold. For given exit conditions of jet velocity and temperature, the combinations thereof with two hot streams and one cold stream, we require: 1) knowledge of the nature of convective mixing of the hot and cold jets under various conditions such as the length over which a fraction of the thermal mixing occurs, 2) qualitative and quantitative information on the *frequency* of the velocity and temperature fluctuations above the jets and *frequency-related* information such as the spectral content of the recorded fluctuations.

Regarding the type of experimental data obtained, both temperature and velocity measurements were taken, the latter using both Laser Doppler Velocimetry (LDV) and Ultrasonic Doppler Velocimetry (UDV). Velocity measurements of the lone (single-jet) central jet were first taken by LDA and then later replaced by UDV. In the latter, the device used for UDV is known as the Ultrasound Velocity Profile monitor (UVP). The UDV velocity measurement consisted of two groups of velocity data, each with a slightly different purpose in the overall scope of the experiment. We refer to these two groups as: 1) *pre-planned* and 2) *exploratory* measurements. We define each as follows.

Pre-planned means a *complete* set of velocity measurements consisting of a scan of the flow field of interest; that is, *complete* in the sense of purposefully traversing a fixed ultrasound transducer probe at a fine enough traverse increment along an overall span of sufficient length, such that detailed information on the velocity field would be collected. [For the *single ultrasound transducer probe* operation used in this initial phase and report, the "fine enough traverse increment" was 5 mm and the "span of sufficient length" was 550 mm.

Exploratory, on the other hand, means a smaller set of velocity measurements than the *pre-planned* set, nevertheless consisting of a scan of a flow field with a fixed probe traversed along a length at a fine or coarse traverse increment. The *exploratory* data set was often smaller than the pre-planned set because the data consisted of velocity measurements from a trial orientation of the transducer probe. Trial orientations were primarily used to explore velocity information that we considered supplemental to the pre-planned measurements.

In the present report *we mainly limit ourselves to exploratory measurements obtained by UDV* and do not include *pre-planned measurements*. The pre-planned measurements have been reported upon in Tokuhiro and Miyakoshi (1996), Kimura, Tokuhiro and Miyakoshi (1996) and in Tokuhiro, Kimura and Miyakoshi (1997) and Kimura, Tokuhiro and Miyakoshi (1997) as mentioned. We additionally limit ourselves to an identical flowrate for the triple-jet arrangement with the ultrasound transducer located to the right or to the left (a transverse position) of the jetting flow. Finally, for thermal-hydraulic considerations, an extensive set of temperature measurements were taken and analyzed.

II. Experiment

II.1 Experimental facility

Figure 1 shows the experimental loop including the test section. Except for the test section, the rest of the facility functions as a support system shared by two other experiments. The facility thus consists of the thermal striping test section (WAJECO) set within a larger rectangular tank, a loop heater/exchanger for supplying hot water, a head tank in order to control the water-level, a filter to extract contaminants within the loop, an air-to-loop heat exchanger for supplying cold or cooled water back into the loop as well as a general purpose lab water supply tank. In addition, several turbine flowmeters as well as orifice plate type devices, a system of valves and all the connecting piping are as depicted.

A perspective view of the test section itself is shown in **Figure 2**. Since Part I of this report (Tokuhiro, Kimura and Miyakoshi, 1996), the exit geometry and entrance section have been modified as described in the first report. The updated test section is immersed within a rectangular tank measuring 2438W x 2438H x 671D [W-width, H-height, D-depth, all mm], and is itself a partially enclosed rectangular region measuring 400W x 950H x 176.5D (169 mm inner width). As noted in the upper left corner, two plates sandwich the four rectangular blocks thereby restricting the spread of the exiting jet in these directions. The idea was to constrain the jet to a finite width and to "view" it as quasi-two-dimensional within this geometry. The nozzle thus measures, 20 mm x 169 mm, giving an equivalent hydraulic diameter, D_h (or simply D)=2(20)(169)/(20+169)=35.76 mm. The sides are, however, not restricted and the re-

circulating flow can thus be expected to have some small degree of influence on the exiting jetting flow, even though an overflow mechanism is used at the top of the test section (shown). A prominent feature of the tank is the large viewing glass windows on both the *front, back* and *right side* of the tank. This feature was included primarily for LDV measurements and flow visualization techniques. The jets exit from three rectangular nozzles defined by four equally rectangular blocks. The central nozzle is "cold" while the adjacent two are "hot". The hot and cold sources are now supplied by three separate pipes, the cold source being centrally situated, flowing first through an expansion and then through a rectangular constriction (not shown). The hot source, is on the other hand, is supplied from the right- and left-hand-sides into a lower chamber and enters symmetrically through a one-sided rectangular constriction. The exit of the nozzle is a block elevated 75 mm from the reference *groundplane* of the tank.

The other prominent component of the test facility is the traversing thermocouple array and the UVP transducer holder fixed to the left arm of the traversing mechanism. The moving mechanism consisted of two vertical and parallel pillars (OD 45 mm), between which a "bridge" served as a mounting bracket for the thermocouples. This bridge is fixed and moves up and down with the pillars. The pillars are externally-driven from outside the test section (not shown). The traversing thermocouple array consists of 39 thermocouples facing vertically downward and horizontally spaced 5 mm apart over a 190 mm span. The last 5 mm of each thermocouple are directly exposed to the flow, while beyond this point the T/C is insulated for a length of 50 mm. At this juncture, all 39 T/Cs are threaded and bonded to an horizontal arm 275 mm wide and attached to two vertical, cylindrical arms (pillars) 45 mm in diameter. There are 19 T/Cs contained within the left cylindrical arm, as shown in **Figure 3**, while the remaining 20 are in the right arm. The two arms enter through the top of the rectangular tank. The thermocouple type used was T-type, constantan copper-nickel with an expected measurement error of 0.5°C. The junction of the T/C was 0.5 mm diameter an thus the expected response time (in water) was roughly 0.4 sec or 2.5 Hz. Operationally three T/Cs malfunctioned (No. 5, 6, 14 numbering from left) and were not used for data acquisition. Lastly, the figure contains the sense of direction for the terms "transverse, spanwise, cross-stream" and "axial and downstream".

II.1.1 Ultrasound Velocity Profile monitor (UVP), (ultrasound Doppler velocimeter)

Velocity measurements were taken using the Met-Flow Model X-1 Ultrasound Velocity Profile (1992; see **Appendix A, Fig. A-1**) monitor with a single, Delrin-encased (temperature limit ~ 80°C) piezo-electric transducer operating at 4 MHz. The transducer had an active crystal diameter of 6 mm. The UVP works on the principle of ultrasound Doppler echography; that is, the position and velocity information are evaluated respectively from the detected time-of-flight and the Doppler-shift frequency at each of 128

locations. Thus, a componental velocity profile is constructed along the measurement line (ML) of the ultrasonic beam (see **Appendix A, Figure A-2**). By componental it is understood that the velocity vector oriented either toward or away from the face of the transducer (from the sign of the Doppler shift) and the magnitude is measured at each of the 128 "coin-like" volumetric elements during each of the 1024 measurement intervals. The real-time corresponding to 1024 measurement intervals is adjustable depending largely upon the preference (and experience) of the user, though it should be based on the phenomenon of interest in the flow; that is, based on estimates of the time-scales associated with various transport phenomena, the user is able to select either a short or long time span between measurements. The UVP can also detect transient phenomena. A further explanation on deciphering the UVP velocity profile is provided in **Appendix A, Figure A-3.**

The ultrasound is reflected from tracer particles, typically a plastic powder with a nominal size of 80 μm (Expancel DU091-80; see **Appendix B**), that are added to the test medium (water). One should note that the inherent assumptions in using this measurement technique are that: 1) the tracer particles accurately reflect the velocity profile of the liquid state and 2) the modification of the flow field due to addition of tracer particles; that is, the particle-to-fluid interaction, is of minor consequence to the measured profile. Additionally, it is assumed that particle-to-particle interactions are negligible since the concentration of tracer particles, i.e. on the order of 100 grams per 4000 liters (3988) of water, is physically very low. Finally, in the first assumption, the statement "accurately reflects the velocity profile of the liquid state" means *ideally* that there is no slip (relative) velocity between tracer particle and liquid; that is, the particle moves exactly as a fluid element would, as dictated by the initial and boundary conditions of the flow. In reality, this is likely not so, in which case the assumption is that the slip velocity is of negligible consequence and the error associated with the velocity measurement is within an acceptable range. As for the positioning of the transducer, it was held in place by a short piece of pipe through which the transducer was threaded (and held) and the output signal travels through a 4 m long cable. Though the UVP operating parameters were varied, the most common setting was as noted in **Appendix A, Table A-1.** The typical measurement time was of the order of 1-3 minutes.

II.1.2 Laser Doppler Velocimeter (LDV)

Laser Doppler velocimetry was conducted using a forward scatter, two-component TSI System 3300 LDV. The system consisted of the following: 1) NEC GLG 3302 4W argon ion laser, 2) NEC GLS 3300 power supply, 3) two TSI Model 9186A LV frequency shifters, 4) two TSI Model 9162 photomultipliers, 5) two TSI Model 9162 photomultiplier power supplies, 6) two TSI Intelligent Flow Analyzer Model 550s and 7) TSI optics. The tracer particle used was a 30μm "pearl" powder made from

ground mica . The data was recorded onto 5-1/4" floppy diskettes initially and later transferred in text format to a optical diskette (MO format). The beam was introduced into the measurement region through two windows.

II.2 Experimental test cases

As mentioned, photographs, video images, Laser Doppler Velocimetry velocity measurements, ultrasound Doppler velocimetry measurements and temperature measurements were taken during the first phase of this experiment. Here we mainly present the results of the LDV, UDV and temperature along with a few digitized video images to facilitate the discussion.

II.2.1 Conditions of LDV measurements

LDV measurements were only conducted for an isothermal single-jet at average exit velocities of V_{exit}= 1.0 and 2.0 m/s. The measurements were conducted with the test fluid at ambient temperature; that is, in the range 10°-20°C depending on the time of year.

II.2.2 Conditions of UVP measurements

For the data presented in this report, the average exit velocity of both the single- and triple-jet experiments was 0.5 m/s with an estimated error of 0.1 m/s. The temperature difference between the cold and each of the hot jets was held to 5°C in all cases with an estimated error of 0.75°C. UVP measurements were conducted with one transducer fixed at either the right or left locations with respect to the jet(s) (see **Figure 3**). The data taken at these locations are simply designated as "R" for right and "L" for left. Measurements were taken axially, vertically along the z-axis, at 5 mm intervals up to approximately 550 mm above the imaginary *"0"-datum* in most cases. At this point, there are still roughly 1300 mm to the free surface shown in **Figure 2**. The UVP transducer was oriented at an angle of 10° with respect to the horizontal and the first axial position was designated as "0" datum, as shown in **Figure 3**. This position is 75.5 mm above the *groundplane* as indicated. The front face of the transducer was approximately 215 mm from the centerline of the central nozzle. The selection of the 10° angle was in reality an experimental compromise between a sufficient number of scans, which we sought in order to follow the flow development, and the detection of the larger, axial vector component relative to the horizontal component

of the actual jetting flow. Since the UVP measures the velocity component *along* its ultrasound beam, a slight inclination would detect the contribution from the axial component. The axial velocity component is expected to be larger in general than the spanwise, transverse component in this type of jetting flow. At each scanning position (z-location), measurements were taken twice in order to check reproducibility of results which we found to be the case. In **Table 1** a summary of the conditions under which the UVP data presented in this report were taken is presented. In the table sixteen (16) items of information are specified and briefly described as follows:

1) Case No. : simply the number of cases, 1 to 20; A,B,C distinguish parameter changes within a case.
2) Case Name: case name for internal reference; refer to this when asking for data sets.
3) No. of files: describes the number of data files contained in the case name.
4) No. of jets: simply describes a single(1) or triple-jet(3) configuration.
5) TDX orientation: describes the orientation of the transducer with respect to the horizontal.
6) $U_{av,exit}$: describes the average exit velocity of the jet in [m/s].
7) $T_{hot,exit}$: describes the average temperature at the exit of the hot jet in [°C].
8) $T_{cold,exit}$: describes the average temperature at the exit of the cold jet in [°C].
9) Traverse range: describes the transverse range and increment in parenthesis "( )".
10) Traverse increment: describes the traverse increment in [mm].
11) TDX facing: describes the orientation of the normal of the TDX face; that is, right or left.
12) Channel distance: describes the "thickness" of each of 128 measurement volumes (channels) in [mm].
13) Starting Channel [mm]: gives the spatial distance from the head of the TDX where measurement begins.
14)Ending Channel [mm]: gives the end channel
15)Primary Frequency [Hz]: describes the frequency at which the pulses are repeated.
16) Sound Velocity [m/s]: describes the acoustic velocity in the liquid, thereby defining the test medium; taken as a constant.

III. Results and discussion

Representative results from LDV, UVP and temperature measurements of both the single- and triple-jet are presented in this section. We begin with the flow visualization data.

III.1 Flow visualization data: photographs and video images

Photographs, still video prints and video images were taken as part of flow visualization. In **Figures 4-6** we show one frame taken from video images for the case names as noted. Photographs and still video prints (one frozen frame directly printed by a Sony video-image printer) were also taken, but are not

included because they contain the same kind of visual information. The flow visualization images have for the most part been taken with laser-sheet (argon laser) illumination from the side with Uranine dye added to the test medium. A bright horizontal line tracing the laser sheet beam is clearly visible on the top surface of the nozzles. The nozzles themselves consist of four rectangular blocks as shown. In each image beginning with Fig. 4(a) we superimpose both the approximate axial and spanwise scales, centered about the jet's axis (or center jet in Fig. 5 and 6), and also trace in dotted line the apparent spreading rate for the single-jet and the exterior boundary of the merging and merged triple-jets. The average exit velocity out of the nozzle is noted as "V", while temperatures of the hot and cold jets are respectively, T_H and T_C (or T_h and T_c)

The images cannot only yield quantitative information, but are valuable qualitatively. We summarize the relevant points as follows: 1) the video images reveal the spatio-temporal nature of the jetting (single- and triple-jet configurations) flows featuring a number of visible flow structures, 2) features of the single-jet such as the jet spreading rate (~20 mm width at exit to ~80-100 mm at the top) and the largest eddy-to-eddy distances (~50 mm) clearly change with inlet velocity and 3) the triple-jet also has similar features, but of interest is the distance from the exit where the three jets visually converge; for example L~120-130 mm (case J3E-01). As we have reported previously in Tokuhiro and Miyakoshi (1997) and Kimura, Tokuhiro and Miyakoshi (1997), the axial location at which the jets converge is a region of intense flow fluctuations. The hydrodynamic fluctuations which appear first subsequently initiate thermal mixing as well. Lastly **Figure 7** shows 1/15th second interval snapshot images of the triple-jet under three different conditions. The flow conditions are described by the hot-and-cold temperature difference (ΔT_{hc}) and average exit velocities ($U_{exit,hot}$; $U_{exit,cold}$). Due to a difference in the flow visualization condition (dye concentration, laser light source) the images are not equally shaded. Qualitatively however, the change in the flow structures are apparent as depicted. **Appendix C** contains a table of filed photographs and video prints. The pair of "Hi8" video-cassettes are contained with the photographs and video prints.

III.2 Single-jet velocity data

III.2.1 LDV data: average exit velocity U_o= 1.0 m/s , U_o = 2.0 m/s

Figure 8 shows a vector plot of the single-jet with an average exit velocity of U_o= 1.0 m/s, superimposed on the iso-contours of the magnitude (speed). A similar vector plot for U_o= 2.0 m/s is shown in **Figure 9**. Fig. 8 contains some 330 vectors, corresponding to the number of measured spatial points. The grayscale range is from 0 to ~1 m/s in the figure, such that the darkest shades of gray are speeds less than 0.2 m/s. As expected the central, lightly-shaded portion is the jet itself with the largest (mostly) vectors. Equally the regions to either side of the jet qualitatively show the entrained flow as being roughly 1/10th to 1/20th as large as the jetting flow (see Fig. 9). The order of the entrained flow is confirmed in **Figures 10**

and **11** (U_o= 2.0 m/s) and **12** and **13** (also U_o= 2.0 m/s) where we respectively show the average velocity and associated standard deviation profiles at various axial (Z or z) locations. The velocity shown here is, $U=(U_x+U_y)^{½}$ where U_x and U_y are the axial and spanwise velocity components. As expected a symmetric profile spanning roughly 50 mm has a peak velocity at the center of approximately 2 m/s, while the entrained flow region shows a constant profile at roughly U~0.1 m/s. The width of the jet gradually enlarges, especially from 160<z<400 mm (Fig. 11), while the SD-profiles, taken as describing the velocity fluctuations (u'), display the twin-peaks characteristic of the edge and core of the jet. In terms of magnitude, the maximum fluctuation at the jet's edge is u'/ U_o ~0.2 (0.4/2.0), while beyond this region, at the sides, u'/ U_o ~ 0.0125 (0.025/2.0). Note too that the jet spreading is much more noticeable with the SD-profiles than with the average velocity.

As two-component LDV measurements were made, we additionally show in **Figure 14** profiles of U_y, the spanwise velocity component at various axial locations. Because the U_x-component (axial component) dominates the U_y-component in magnitude, the former component essentially mimics **Figures 10** to **13** and is therefore not shown separately. We have shown a combination of lines and symbols to distinguish the axial development of U_y. In order to facilitate our discussion, we point out a number of features, as follows: 1) because the direction of flow is in opposite directions beyond the core region of the jet, the quasi-steady velocities (±0.75 m/s) to the right and left of the central regions are symmetrically distributed as such, 2) U_y near the exit shows fluctuations (waviness in blue) near the jet's core and a double-peaked profile; the former correctly identifying the lack of a U_y-component about the center, 3) the profile of the jet gradually widens as expected (compare z=10, 200, 400) and 4) due to spanwise expansion and then entrainment of ambient fluid, the center of the jet gradually obtains a U_y-component beyond z >10.

Next as an introductory comparison of LDV and ultrasound Doppler velocimetry (UDV) which we also used for the single-jet configuration, we present in **Figure 15** a comparison of velocity profiles taken by each method at the selected axial locations. In the figure, the normalized axial component, $U_x/U_{max(mm)}$, is shown at three nearly identical axial locations (z=160/170, 275/280, 400 mm from the nozzle exit). Except for the regions corresponding to the edge and beyond, x/D≥1l, agreement is generally good. The difference is in the entrained flow region where the LDV data show pointwise U_x-components while UDV data represent a calculation of the U_x-component from measurement of the component at 10° to horizontal. Thus as the UDV profile contains directional (+ and -) values along its beamline (see Fig 3), it is not clear except by ad-hoc means from where corrections to the profiles should be made in order to more closely reflect the LDV data. That is, while the central region of the jet should physically be dominated by U_x-components, the U_x-components should diminish as we approach the edge of the jet. It is not clear at what spanwise distance, this correction should be instituted. We have thus left the profile "uncorrected" and note at least that the entrainment regions to either sides approximately reflect flow away (- ; negative values)

from the face of the transducer (left-side) and flow toward (+; positive values) it. The magnitude however, is biased toward the right-side.

The validity of the LDV-derived jet data, with respect to traditional jet characteristics (i.e. decay of centerline velocity, jet half-radius, etc.) and further comparison to UDV results, are presented in the section to follow along with ultrasound Doppler velocimetry results.

III.2.2 Comparison of LDV and UDV single-jet parameters

We assumed above that the reader is familiar with the basic aspects of a simple jet. Briefly, a jet consists of three separate flow regions proceeding axially (downstream) from the exit. In order the flow regions are called: 1) the (potential) core region, 2) the transition region and 3) the fully-developed or self-preserved region. The core region describes the flow from the exit, wherein the centerline velocity remain unchanged from the initial value and the turbulent mixing begins at the "edge" or periphery of the jet. The "core length", z_{uc}, is defined as corresponding to the axial location at which this turbulent mixing reaches the jet axis (center). Beyond this point, there is a short transition region where the velocity profiles begin to look similar, but nevertheless change with axial distance. Finally, the fully-developed or self-preserved region is characterized by a velocity profile that is similar in shape and only changing in scale. Two parameters that characterize the isothermal jet along the axial coordinate and enables one to identify these regions are: 1) the decay of the centerline velocity, U_o/U_m, where U_o and U_m are respectively the average velocity at the exit and at the jet axis (usually the maximum) and 2) the jet half-radius, $r_{1/2}/D$, where $r_{1/2}$ is the distance from the jet axis to where the velocity assumes a magnitude one-half that at the jet axis. We present these two values as a measure of validity of our experimental apparatus and additionally, as verification of UDV versus an accepted velocimetry technique in LDV. For reference a schematic of an isothermal jet and its parameters are given in **Appendix D, Figure D-1.**

We first present in **Figure 16** the axial decay of the centerline velocity, measured by both ultrasound and laser Doppler velocimetry from the present experiment, against past data represented as correlation lines. The past data were extracted from Kataoka (1986) and are represented by linear regression lines above the so-called velocity core length, z_{uc}. In the figure, the core length corresponds to the axial location below which the data assumes a quasi-constant value ($z_{uc} \sim 4$). To the best of our knowledge the past isothermal jet data can be summarized as follows: 1) Kataoka and Takami (1977) - axisymmetric jet; CO_2-into-air and air-into-air; $4900<Re_o<8300$; $5.76<U_o<12.55$ m/s, 2) Corrsin and Uberoi (1949; 1986) - axisymmetric jet; air-into-air; $31000<Re_o<37000$. We do not have details on Warren's work (1957; 1986) except that his working fluid was air and that he also studied negatively buoyant jets. We present the UDV data in two different manners, these being: 1) U_o/U_m based on the calculated velocity vector (thus UDV from two directions) about a narrow central region (symbol +), and 2) U_o/U_m simply based on the measured

component along the ultrasound beam, with the transducer (tdx) at 10° (abbreviated to "tdx@10") with respect to the horizontal (symbol o). We note that consistent with the scaling laws for jets as presented by Chen and Rodi (1980), the rate of decay is smaller for a plane jet in contrast to an axisymmetric jet. In fact, the slopes are respectively: 0.161 for Kataoka, 0.128 for Corrsin, 0.10 for Warren and (0.082 for "+"; 0.13 for "o") in our case. So, even for identical gases there are slight variations in slope and larger variations in magnitude as shown. Thus although there are differences in slope corresponding to the "o" and "+" symbols, in light of the greater discrepancy between the regression lines of Warren, Corrsin and Kataoka, our results appear to be in agreement with past jet studies.

Figure 17 shows a plot the jet half-radius, $R_{½}/D$, versus axial distance, z/D, along with correlations put forth by Hinze and (v.d. H) van der Hegge Zijnen (1949), Kataoka et al. (1968) and Donaldson et al. (1966). Our UDV/LDV data are depicted together [LDV "o" and UDV "+"] and as a polynomial regression line (gray solid with curvature) through the points. Note that the four trendlines are very similar, with only a slight difference in slope. In fact, while Hinze and v.d. H. Zijnen's data is for a slightly non-isothermal ($\rho_{\infty(ambient)}/\ \rho_{exit}=1.05$) planar air jet, Kataoka et al. investigated both iso-/non-isothermal(heated) axisymmetric exhaust gas jet injected into air, CO_2 injected into air and air/air arrangements. The correlation however, is for $\rho_{\infty(ambient)}/\rho_{exit}=1$. In order to estimate the half-radius from our velocity profiles, a polynomial regression with a coefficient of correlation greater than 0.9 (except for one or two cases) was fitted onto the velocity data, including one to two data points below the one-half velocity, $½U_m$, point The half-radius was subsequently calculated from an equation describing the regression.

Finally, **Figure 18** shows a plot of the average radial (or spanwise) velocity profile, including the correlations put forth by Kataoka et al. (1968) [axisymmetric gas jet] and the UDV/LDV data (as symbols) at nearly the same z/D-locations. Kataoka and his co-workers only presented one-half of the profile, assuming symmetry, and data only in the fully-developed region, corresponding approximately to $6\leq z/D \leq 12$. The trendline shown in solid consists of two correlations with a common point at $R/R_{½}=-1$. One can see that there is agreement between the UDV/LDV data and the correlation, though the former is slightly biased toward larger values, for $0\leq R/R_{½} \leq -1$. However beyond $R/R_{½} \leq -1$, the fully-developed or self-preserved condition, though generally obeyed for UDV and LDV points respectively, agree less overall with respect to the correlation. The difference though is not significant since there are differences between the planar and axisymmetric jet. If one consults for instance Chen and Rodi's (1980) radial profile of the relative axial turbulent intensity, comparing the axisymmetric against the planar jet, we see differences at least as large as the one in our figure. The only significant difference in the data is that between the UDV/LDV data at $-2.0 \leq R/R_{½} \leq -1.2$. At these lower velocities, on the order of several mm/s, the resolution of the LDV is superior to that of the UDV. At the same time, as the sign of the Doppler shift is contained in the UDV data, a substantial presence of oppositely directed flow will alter the average velocity

profile. The comparison of the LDV/UDV measurements to past investigations of the single-jet are contained in Tokuhiro (1999).

Figure 19 depicts the jet half-radius versus axial distance, but for data extracted from "*far-field*" UDV measurements. That is, in contrast to Fig. 17 where the measured distance and (each) channel width are respectively, L_{dist}=284 mm and l_{ch}=2.22 mm, for the far-field measurements these parameters were, L_{dist}=663 mm and l_{ch}=5.18 mm. This in effect means that a wider span of the entrained flow region to each side of the jet is measured. However, the narrow region encompassing the jet profile is measured with less than one-half the spatial resolution (2.22/5.18=0.4289). It is therefore not surprising that the jet half-radius is over-predicted and shows much more scatter beyond the jet's core length (z/D~3-4), from where the velocity profile gradually changes. The correlation coefficient, though acceptable, shows along with the data points that these particular operational UVP parameters (L_{dist}=663 mm and l_{ch}=5.18 mm) are inappropriate for validating our data against past single-jet studies. We did correctly change subsequently, the UVP parameters so that Fig. 17 depicts favorable agreement with past single-jet data. This plot thus shows the importance of choosing the correct UVP parameters, with respect to the measurement objective.

To conclude validation of the single-jet data against past studies, we show in **Figure 20(a)**, the estimated axial trend of the "mass-flowrate". The mass flowrate has been estimated from an integration of the velocity profile, fitted with a polynomial regression (usually 5th order) at each axial location. The polynomial was then integrated from the beginning of the entrained region to the jet axis. We note that the mass-flowrate is an estimate because of two sources of errors, these being: 1) correlation of the polynomial regression, ranged from r^2=0.7-0.9, such that integration inherently contains uncertainty and 2) selection of the lower limit of integration involves judgment; that is, selection of the beginning of the entrained flow region was taken some 4D from the jet's axis and discarded any physically unrealistic magnitudes. The "Integrals" are given as symbols and the polynomial regression, whose equation and correlation coefficient (R2) appear in the figure, are as shown. The figure shows the following trend in terms of three flow regions follows: 1) the exit region, $0 \le z/D \le 2$, where there appears a non-zero mass flowrate that quickly decreases, due most likely to the initial expansion of the jet, 2) the core-flow region, $2 \le z/D \le 4$, where the mass flowrate is quasi-constant and 3) the developing self-preserved region, $4 \le z/D \le 14$, where the spanwise distribution becomes self-similar and quasi-linearly increases. Thus as indicated in the self-preserved region, separately shown in **Figure 20(b)**, the linear slope of the trend beyond $z/D \ge 4$, is approximately 0.088 while Chen and Rodi predict 0.11. We thus have reasonable agreement.

III.2.3 Single-jet calculated vector field

As UDV measures the velocity component along its beam-line, if measurement is taken from *two* different directions, the vector at the virtual intersection of the two beams can be calculated. Thus minimally, if two transducers emit ultrasound beams simultaneously, then the velocity vector at that short instant in the sampling time can be calculated. In our case however, one transducer had to be traversed axially (vertically) from the left and right sides. So, the velocity components from two directions, taken at different instances in time, were taken. In this case, if one tacitly assumes that the flow is temporally (time-wise) "periodic" and spatially "quasi-steady", both of which are at best first-order approximations, we can estimate the "average" vector flow field.

Figure 21 thus shows the calculated composite "average" vector field for a single-jet. As expected the central region is characterized by the jet itself (largest vectors) while the surrounding regions, to either side, depict the entrained flow vectors of much smaller magnitude. Also shown in the figure are the chaotic flow at the entrance (z~0, 75<x<350) and an overall bias toward larger flow vectors to the right of the jet axis. The reason for this latter feature is hard to trace, except possibly that the flow, when measured from the right, was indeed larger than when measured from the left (and vice-versa). Although some 14,000 vectors (exactly 128x108; 13824) could be plotted, only about 6,6000 are shown for clarity. The representative vector and its magnitude (301.76) is given in mm/s. The next plot, **Figure 22,** shows yet fewer vectors superimposed on 10 magnitude grades of isocontours. Here the density of isocontours defines roughly 30 mm/s increments in magnitude, with the highest density of isocontour lines representing an increase to the maximum value. Note that vectors and isocontours consistently delineate the central jet, as well as entrained flow regions.

III.3 Triple-jet velocity data

3.2.1. Triple-jet calculated vector field

We next present velocity data of the triple-jet configuration. We first present in **Figure 23** the equivalent of the previous figure; that is, approximately 6600 vectors superimposed upon isocontours in 30 mm/s increments (20 levels). We note in general the following features, these being: 1) the recognizable presence of two jets (center and right) and marginally the third jet (left), 2) the convergence of the right and left jets with the central jet, 3) the entrainment of flow in-between the jets, 4) several areas of (physically) inconsistencies, such as at Z~ 350 (75<X<350) and a slightly sloped, irregular region approximately from (X~160, Z~200) to (X~210, Z~500), characterized by a concentration of isocontours and large flow vectors and 5) an overall bias (asymmetry) toward larger vectors right-of-center in contrast to left-of-center. From

looking at many of the individual velocity profiles from Z~200, the aforementioned irregular region is most likely due to a peak or drop in the echo signal. It is apparent from this figure that vector field measurement using *one* vertically traversed transducer (TDX) is deficient for several reasons, as follows: 1) traversing the TDX from one side, then the other side consumes too much time (~ 1 hr) and 2) for this reason, the meaning of the average vector field diminishes if the flow fluctuates considerably in time and space. We thus concluded that for UDV, a multiple number of TDXs are needed, as well as a confirmation of the results by a second means, such as particle image velocimetry. We have thus shown Fig. 23 to demonstrate that a vector field equivalent to Fig. 22 was estimated. However, due to the inconsistencies we cannot draw any meaningful conclusions. We can see in grayscale isocontour in **Figure 24** a largely qualitative plot of the various flow features, primarily the right and center jets, as well as the flaws mentioned above. The grayscale spans 0 (black) to 70 mm/s (very light gray).

3.2.1. Triple-jet with ΔT_{hc}=5°C and ΔT_{hc}=0°C

In the Phase I data set there were two flow configurations wherein the only difference was the hot-to-cold jet temperature condition; that is, ΔT_{hc}=5°C and ΔT_{hc}=0°C. So, a comparison of the two potentially yields information regarding the influence of buoyancy.

We begin with **Figures 25(a)** and **25(b)** that show the isocontours superimposed on a grayscale representation of the standard deviation (SD) of average velocity. Both figures depict only the SD of the *transverse* (spanwise) velocity component (w of $[u,v,w]$). Fig. 25(a) shows the X-axis in terms of UVP channels (0-127), while 25(b) depicts the X-distance in [mm]. The grayscale range, from dark (black) to light (white) correspond in velocity to approximately 1 mm/s to 105 mm/s respectively. In comparing the two, some minor differences in isocontours are apparent visually. However, in order to directly contrast the difference we present in **Figure 26** the difference itself with respect to the ΔT_{hc}=0°C case. We note that overall the difference is small, roughly spanning only ±0.4 mm/s, but there is a clearly discernible "region" or distinct spatial distribution between the two cases. That is, the flow configuration with ΔT=0°C has a larger fluctuation near the exit of the jet (~130<X<~290, ~1.0<Z/D<~3.8), but the SD diminishes such that downstream (~110<X<~270, ~5.0<Z/D<~14.0), the ΔT_{hc}=5°C case contains more fluctuations. It remains to be seen if this is the prevailing trend; that is, in summary 1) that the existence of a temperature difference has the effect of "suppressing" the velocity fluctuations from near the jet exit up to where the three jets merge, while 2) the remaining temperature difference beyond, z/D>5, "maintains" the existence of velocity fluctuations in contrast to the isothermal case. All the other regions, except a small region (~280<X<~330, ~8.0<Z/D<~9.4), show no difference in terms of flow fluctuations. It is difficult to say whether these small regions, as opposed to the clear difference as noted, represent anything of physical significance because of the following: 1) the difference in the exit flow conditions were likely of the same magnitude as figure itself,

and 2) difference itself is a very small fraction (~1/100th) of the characteristic magnitude of fluctuation in the jetting regions. We do however, assert the consistency in the aforementioned spatial distribution.

We next scrutinize the individual spanwise (transverse) profiles of the *difference*, respectively in normalized average velocity and SD in **Figures 27(a), (b)** and **28(a), (b)**. The difference here means, $U(\Delta T_{hc}=5°C)-U(\Delta T_{hc}=0°C)$ ["dT5-dT0"], where U is taken as representative velocities, either U_{avg} or u_{rms}. For clarity only four to five profiles at representative axial locations are shown, with the coordinate axis centered about the central jet. The reproducibility, though not shown was confirmed for the data shown. The axis of the three jets are located at (x/D ~ 0, ±1.95) and the width of each nozzle is x/D~0.56. We restrict ourselves to the general trends and interpret the differences as follows, consulting both U_{avg} and SD:

1) U_{av} for 20<z<100: the edge of each jet (indicated) is apparent in Fig. 27(a) and assumes peaked positive and negative values (at z=20, red) because the spatial edge of the jet apparently does not coincide for the $\Delta T_{hc}=5°C$ and $\Delta T_{hc}=0°C$ cases; axially downstream, as the jets entrain flow from each side, the peaky profile becomes less prominent and slightly narrows in width, to a region to the right and left of the central jet; finally, note that for z=80(green), 100(dotted black) the profile is approximately antisymmetric about x/D=0.

2) U_{av} for 120<z<500 (Fig. 27(b)): the relatively small differences up to z<120 become larger, positive differences for z≥200, suggesting that upon approximate completion of thermal mixing, the remaining buoyancy attributable to $\Delta T_{hc}=5°C$ is able to maintain U_{avg} in excess of the $\Delta T_{hc}=0°C$.

3) SD for 20<z<120 (Fig. 28(a)): the difference up to z~120(green) is negative as shown in the figure; that is, flow fluctuations are larger for the $\Delta T_{hc}=0°C$ case; at approximately z~60(brown) fluctuations on either sides of the central jet increase relative to the $\Delta T_{hc}=5°C$ case; this suggests that hydrodynamic mixing occurs ahead of thermal mixing.

4) SD for 20<z<120 (Fig. 28(b)): the small negative values at z=20(red),120(blue) become mostly positive values at z=200(black), 300(green), 400(purple); this additionally suggests that buoyancy is able to sustain velocity fluctuations.

We next show in **Figure 29** the difference in the normalized *axial* U_{avg} and SD component of flow spanning a distance of 91 mm (z/D=2.54), with z/D=0 representing the nozzle exit. The plot shows the difference between the triple-jet's central jet and single-jet, thus U(3j)-U(1j). So, the plot depicts the "true" nature of the triple-jet's central stream, less the single-jet characteristics, but influenced by the right and left jets. The UDV transducer in the data shown was affixed to the vertically traversing bridge and faced downward along the vertical axis of the center jet. The 6-point averaged moving is provided as a reference trendline. In **Fig. 29**, the data between ~0.2<z/D<~1.2 [7<z<43 mm], approximately corresponds to exit region of the jet. As indicated, except for ~0.2<z/D<~0.4, the small differences in the U_{avg} and SD mean that the (central) jetting flow for both single- and triple-jet are essentially alike. However beyond z/D~1.2, the right and left jets begin to converge upon the central jet, as verified from video-images, such that both U_{avg} and SD correspondingly begin to reveal oscillatory trends. The difference in U_{avg} assumes large negative values between ~1.3<z/D<~1.5 and ~1.8<z/D<~2.25 [46.5<z<53.6 and 64.4<z<80.5] and positive

values between ~1.5<z/D<1.8. These regions approximately correspond to the regions where there is an ingress of alternately the right and left jets toward the central jet. As this influx largely encompasses spanwise velocity components, the "sense of rotation" imparted on the central jet's flow structures influences the sign of the difference, as shown in the axial component. At the same time, the influx of the right and left jets enhances both the spanwise and axial flow fluctuations, here represented by the axial SD distribution. The initial increase in SD at z/D~1.5 is slightly downstream of the U_{avg}-trend because the spanwise component dominates the axial one as the jets merge. One can then see that independent of the average velocity, the approximate spatial periodicity of SD reveals the order-of-magnitude of the typical "eddy" size. That is, the roughly 0.3D (=10.7 mm) width of the fluctuating extent may be interpreted as the "scale" of thermal mixing. A simple sketch of some of the approximate features discussed is given in **Figure 30.**

Figure 31 shows the next ~2.5D of the flow beyond Fig. 29, thus ~89<Z<186 mm. Spatially this span corresponds to two region, first where the right and left jets finish converging upon the central jet (up to z/D<4) and second, where there is a flow transition to composite-like jet structure (z/D>4). For visual reference we refer the reader to Figs. 5 and 6. Generally we found the data especially difficult to interpret in terms of plausible physical arguments. We will thus only mention a few plausible characteristics. The mostly positive U_{avg} and SD distributions between, ~2.8<z/D<~4 [~100<z<~143] identifies a region where the convergence of the three jets expectedly enhances both the axial flow and its fluctuating component. We note that although the difference with respect to the single-jet is positive, the peak-to-peak distance of the SD-trend is approximately unchanged when compared to Fig. 29. This then means that the eddy size is quasi-constant up to this point. Beyond z/D>~4 however, there is another region of flow that corresponds to the "gray" region above the jets in Fig. 26. Here as shown the difference in SD roughly diminished to zero; that is, with respect to flow fluctuations themselves and development (spatio-temporally) the triple- and single-jets are very similar. The U_{avg} points however, fluctuates dramatically indicating that composite-like jet, at least at the center, is quite unlike the single-jet. We draw no further conclusions with respect to Fig. 31 at this point.

III.2.3 Triple-jet axial component and trends

Figures 32 is a plot of axial velocity component (*w*-component), U_z and SD_z, from the jet exit to 85 mm from it, given as symbols and as 10 pt. moving averages, all with respect to normalization factor $U_{av,0}$. The data only represents the central jet of the triple-jet configuration, but clearly shows the axial location where the hydrodynamic mixing of the right and left jets, into the central jet begins. The data and trendlines show the following: 1) that axial exit velocity and its fluctuation, at roughly 1/10th the average, is maintained up to approximately z/D~1.2 (42.9 mm), 2) that at z/D~1.2 the entrainment of the side jets

decreases the axial average velocity, while increasing the relative SD of the flow; that is, signifying the entrainment of the right and left jets, and 3) the trend beyond z/D~1.5 (53.6 mm) is difficult to understand, because the dominant phenomena is the merging of the jets and the side-to-side oscillation, the latter of which is ill-represented by an averaged distribution like that shown. Both are spanwise phenomena that one expects will have a influence on the axial average velocity and its fluctuating component.

Figures 33 is a composite plot of the axial velocity component (*w*-component) of the central jet of our triple-jet configuration. As the data was taken in approximately 85 mm increments (2.38D) axially, these were joined end-to-end in order to construct the distribution shown. In the figure, the symbol and three trendlines representing 48 pt. moving average are shown, depicting the following: 1) (circles) the spanwise averaged standard deviation of velocity, at a given z-location, $SD_x(z)$, normalized by the spanwise averaged velocity at z=45 mm from the exit, $U_{av}(z45)$, 2) (dark solid line) the axial $SD_z(z)$ normalized by the average exit velocity, $U_{0,av}$, 3) (dotted line) the axial centerline velocity, $U_z(z)$, normalized by the average exit velocity and 4) (dark gray line) the axial $SD_z(z)$ normalized by the SD at the exit, SD_0. The 48 pt. moving average has been determined as a compromise between smoothing the actual erratic trend and depicting its trend. The lower three trendlines in the figure foremost depict the oscillatory nature of the jets, with the periodicity representing a measure of the characteristic spatial extent (something akin to the jet radius) corresponding to one cycle of the side-to-side oscillation. That is, as simply depicted in two hypothetical positions, Fig. 30 (upper right), the ultrasound beam intersects different parts of the oscillating jet, so that the 2D to 3D spatial periodicity approximately represents twice the width of the mixing zone to one side of the jet. We note that this is consistent with the heat transfer results [Cf. 18] which indicate intense thermal mixing over 2.25D centered about the central axis. Additionally, $SD_x(z)/U_{av}(z45)$ and $SD_z(z)/U_{0,av}$, which show similar information, but respectively for x- and z-components of flow, are noticeably more than one order of magnitude different in magnitude, the axial being much smaller than the transverse component as expected. We also note that the minimum $U_z(z)$ of the peak-to-peak change increases relative to the nearly constant maximum with axial distance. This is an indirect indication that three jets merge and form a composite jet. Simultaneously, as the jets sway side-to-side and induces thermal mixing, the primarily axially flowing composite jet gradually develops. As for the trend in $SD_z(z)$, we see two regions, these being: 1) $1.3<z/D<\sim8.8$ and 2) $\sim8.8<z/D<14$. In the former, fluctuations relative to the value at the exit, SD_0, are initially large due to the merging of the jets and remain periodically so due to the oscillation-induced mixing. The relative minimum value stepwise decreases as the mixing proceeds (roughly at z/D~3.6, 6.1, 8.8). Here as the oscillation-induced mixing proceeds (dominated by spanwise mixing), we physically expect the fluctuations to decrease. Beyond z/D~8.8, as the thermal mixing is essentially complete, both the relative maximum and minimum appear to stabilize as well as the trend in between.

In **Figures 34** and **35** we contrast the axial development of the spanwise averaged velocity, U_{avg}, and its associated SD respectively. The data represent the spanwise (transverse) component of velocity (*w* of *u,v,w*), while the lines in both figures represent polynomial regression curves with a correlation coefficient of at least 0.85. Generally there are three axial flow regions distinctly characterized by their quasi-constant slope, these being: 1) the exit region, 0.4<z/D<2.4 [14.3<z<85.8; mm], 2) the developing region, 2.4<z/D<6 [85.8<z<214.6] and 3) the quasi-developed region, 6<z/D<14 [214.6<z<500.7]. We note the following similarities and dissimilarities for the average velocity (Fig. 34), as follows: 1) the overall trend for both ΔT=0°C and ΔT=5°C are very similar, with the difference between the two initially increasing but holding steady beyond z>2, 2) the exit and developing regions are physically explained by the initial expansion of the jets, followed by their convergence so that U_{avg} recovers and 3) the quasi-developed region is noted by the quasi-steady velocity. In Fig. 35, we note the following: 1) again a similarity in trend for both cases with the difference gradually increasing downstream, 2) as the jets merge in the exit region, the fluctuations markedly increase, while completion of the mixing in the developing region sees a transition to a plateau, followed by 3) a decrease and leveling-off in the quasi-developed region. The small differences, at least for spanwise averaged velocities, indicate that the influence of buoyancy corresponding to ΔT=5°C is minor with respect to the flow.

In **Figure 36** we plot the difference in the normalized U_{avg} and SD, that is [U_{avg} (ΔT=5°C) - U_{avg} (ΔT=0°C)], with the matching solid/blank symbols representing two separate trials (t1 and t2) and the polynomial regression curves indicating the approximate trend. The normalization factor adopted over the spanwise distribution was the range of the spanwise velocity, expressed as (U_{max}-U_{min}). The distributions in the previous two figures, in contrast are the axial variation of the *spanwise averaged* values. We first note that except for a few pairs of points, the two trials yield largely similar values. As mentioned in a previous context, since the flow conditions were not exactly the same in the two runs, we expect some discrepancies. We then note as in the discussion of Fig. 26, that the difference in SD is negative as the velocity associated with ΔT=0°C is larger than for ΔT=5°C, from 0<z/D<3.6 (to 5.2 for U_{avg}). Since there is obviously no thermal mixing in the former case, other than the initial expansion of the jets which appears to be relatively larger for the isothermal case, the recovery of the difference supports the view that *hydrodynamic* mixing, consisting of first the convergence of the jets, begins from around z/D~2.0 . Furthermore as the SD-trend increases and assumes positive values beyond z/D~3.6, there is evidence that thermally-based flow fluctuations are maintained up to and beyond the end of the mixing region (z/D~6).

We present in **Figures 37** and **38** axial distribution plots of U_{avg} and the estimated Root-Mean-Square (corresponding to the SD) respectively, as measured from the right (R) and left (L) sides, and separately expressed as the ratio of triple- to single-jet data. A similar plot was given in Part I [Cf. 18]. We note that here, the transducer is oriented at an angle 10° from horizontal so that the velocity component

detected is nearly the spanwise one. In **Fig. 37**, triple-jet data taken with the UDV-transducer positioned to the right and left of the jets are given, as well as the single-jet trend. One can see that for both jet configurations U_{avg} initially decreases, due to the immediate expansion of the jet(s), and then sharply increases, especially in the case of the triple-jet as the right and left jets converge upon the center. In fact, relative to the single-jet the average and RMS velocities respectively reach in magnitude, approximately five-times and seven-times the single-jet value. As previously reported [Cf. 18], while the spanwise averaged RMS gives some measure of triple-jet flow fluctuations, the RMS in the region in-between the hot-and-cold jets is of particular importance as this is the region where initial hydrodynamic mixing initiates thermal mixing. We reported that the triple-jet RMS was locally as much as 20 times as large as the single-jet RMS at the same axial location. Subsequently, while the single-jet average steadily increases up to approximately z~125 (z/D~3.5), the triple-jet slightly dips before increasing again between ~100<z<~170 (2.8<z/D<4.75). The dip in magnitude approximately corresponds not only to where the mixing concludes, but where the composite jet develops, equally characterized by high intensity of fluctuation. This is evident in **Fig. 38**, where we show the axial distribution of single- and triple-jet RMS-values, spanwise averaged and normalized by the maximum spanwise velocity. We note that the triple-jet raw data increases from a local minimum at z/D~1.25 (z~44.7) to an absolute maximum at z/D~2.75 (z~100). From here, for z/D>2.75, the RMS gradually decays over 12 diameters. In both figures, a comparison of measurements taken from the right and left transducer positions show approximate agreement, certainly in the trend but not in absolute value. We are satisfied with the similarity in trend because the experimental conditions for "triple-R" and "triple-L" were not identical. As for RMS/U_{max} note that an immediate increase (triple-jet) as opposed to a gradual increase (single-jet) is the significant axial difference between the two configurations. In fact, the triple-jet RMS/U_{max} attains its end value (RMS/U_{max} ~0.8) reached beyond z/D>8.75, within 0<z/D<~2.5 and only exceeds this value in-between, 4.5<z/D<~7. This latter region is just beyond the noted thermal mixing region and further supports the view that a non-zero ΔT maintains flow fluctuations. In other words, the side-to-side oscillation thermally mixes the jets rather than the inherent turbulence associated with the jets.

III.2.4 Triple-jet spectral data

Finally **Figures 39** and **40** show the normalized frequencies of the spanwise velocity component under the conditions, ΔT=0°C and ΔT=5°C. The normalization factor was the maximum frequency amongst the first 20 peaks ordered in terms of spectral power at a given axial location. In both cases, the maximum frequency described the side-to-side oscillation of the jets in the mixing region; that is, the dominant frequency of oscillation was approximately f ~2.2-2.3 Hz. As we can see the overall trend is very similar, whether ordered in terms of the first, second or third dominant peaks. We note the main features as follows, these being: 1) the appearance of a number of frequencies at the exit (z/D<1.2), but shortly thereafter, 2) an

approximately constant frequency, though slightly different for the two cases spanning much of the mixing region, ~1.2<z/D<~6 (to 8 for ΔT=5°C), and 3) a transition to a lower frequency initially very similar in range for the two cases. That is, for z/D>8, ΔT=5°C to f/f_{max} ~0.15-0.35 Hz and for z/D~6, ΔT=0°C, f/f_{max} ~0.2-0.35 Hz. What is hidden in the figures is the fact that, especially through the transition the maximum frequency drops to approximately 1 Hz. Thus in Fig. 39, relative to f_{max}, the ordered peaks assumed increasing values at z/D~11.2, 13.9 (2nd, 3rd peaks) while increasing and decreasing for the 1st peak. For ΔT=5°C however, although f_{max} incrementally decreased at z/D~8.4,11.2 and 13.9, the ordered peaks did not change as much in contrast to Fig. 39. In fact, the normalized value f/f_{max} is quasi-constant. Thus besides our assertion that the fluctuations of thermal origins appear further downstream than the isothermal case, the relative fraction with respect to the maximum, of the first three ordered peaks is preserved in the non-isothermal (ΔT=5°C) case.

IV. Summary and conclusions

An experimental study on the thermalhydraulics of the thermal striping phenomena was initiated. The data analyses and discussions given here and in the previous two reports [Cf. 18, 19] encompass and conclude Phase I of the ongoing study.

The conclusions as far as the thermalhydraulics are concerned, based on Phase I data are summarized as follows. First regarding the objectives of the investigation and thermalhydraulic conditions.

1) The facility was designed as a experimental apparatus to study the basic convective mixing phenomena of quasi-planar, vertical jets at different temperatures and velocities. The three-jet, hot-cold-hot thermal configuration provides the minimal (in terms of number of jets) representative arrangement of multiple jets, thus simulating the flow out of the core of an actual fast reactor. The hot-cold-hot configuration is more likely than the reverse.
2) The primary objective in terms of mitigating the undesired thermal-structural consequences, such as thermal fatigue, is for the jets to be thoroughly thermally mixed state at the solid boundary where it impinges. Thus the distance from the core to the thermally mixed state also of relevance. Equally, if mixing is incomplete and thus temperature differences between hot and cold streams exist, the frequencies of temperature fluctuations at the solid boundary should not contribute to thermal fatigue of the material.
3) Two primary test cases were: i) equal (average exit velocity) jet velocities (called isovelocity; $r=U_{cold}/U_{hot}=1$) and ii) unequal jet velocities (called non-isovelocity; $r\neq1$). The average exit velocities were U=0.2, 0.5, 0.7, 1.0 and 2.0 m/s, while the temperature difference between the hot and cold jets was, ΔT_{hc}=0°, 5°, 10°C. A complete data set, meaning both velocity and temperature measurements,

was only available for U=0.5 m/s and ΔT_{hc}=5°C; all other U and ΔT_{hc} combinations either had only velocity, temperature or an incomplete set of both.

4) The results should establish a basis on which to develop the computational simulation of the same thermalhydraulic problem. Numerical simulations that can accurately simulate the experimental results are needed in order to investigate additional parameters, many of which cannot be covered experiment due to time constraints.

Given the objectives and conditions above, the Phase I experiments revealed the following in terms of the thermalhydraulic phenomena; that is, the conclusions concerning the convective mixing process under the given test parameters are as follows:

1) The right and left jets were entrained toward the center jet in all cases (all three jet configurations) investigated. This is because the mass-flux of the central jet with respect to the right or left is unequal. Thus the right and left jets are entrained.
2) For both isovelocity and non-isovelocity cases, most of the convective mixing occurred in between the cold and hot jets. Under isovelocity (r=1.0), mixing occurred over approximately 2<z/D<5; under non-isovelocity the onset of mixing was delayed, but mixing did occur over a slightly compacted axial distance, roughly 4<z/D<7. The post-mixing temperature under non-isovelocity was higher than under isovelocity.
3) Spectral velocity data, supported by flow visualization indicate that the dominant flow oscillation under isovelocity is the side-to-side swaying of the jets. In fact, as this oscillation at f=2.25 Hz dominates over the convective mixing zone, it is thought to be the primary mechanism of thermal mixing relative to the turbulence-based mixing. In the post-mixing zone, the dominant frequency distinctively changes to f=0.7 Hz. Under non-isovelocity, the frequencies are dispersed (no dominant frequency), but primarily contain harmonics and sub-harmonics of the side-to-side oscillatory motion at approximately 2.2Hz<f<2.3 Hz.
4) Thus in terms of the frequency and amplitude of temperature fluctuations, under isovelocity conditions, the dominant oscillation frequency is 2.25 Hz with ΔT typically approaching 80% of ΔT_{hc} (5°, 10° C). Under non-isovelocity conditions, which is more likely the flow out of the core, the frequency and amplitude of temperature fluctuations will be harmonics/sub-harmonics of the side-to-side oscillation frequency (f~2.2-2.3Hz) and equally approaching 80% of ΔT_{hc}.

Finally an assessment of the applicability of ultrasound Doppler velocimetry was one of the objectives in terms of measurement techniques. UDV of course is the most promising measurement technique for an sodium-cooled fast breeder reactor. We thus note the following experiences and evaluation of our UDV trials, as follows:

1) Both laser (LDV) and ultrasound Doppler (UDV) velocimetries, can be applied to this type of flow in water. Both LDV and UDV produced data in good agreement with past data for single, isothermal jet characteristics. LDV measurements were limited to the single-jet and superseded by UDV. UDV could measure the triple-jet flow in sufficient detail, except for the nearest jet (near channels) which was distorted. The source of the distortion could not be resolved. Furthermore, operationally a *single* transducer could not satisfactorily deduce the two-dimensional vector field; multiple transducers (10 or greater) are needed along both sides of the jets in order to minimize traverse time.
2) For the triple-jet configuration the transducer was place at a 10° with respect to horizontal, as a compromise of two factors, these being: i) to capture most of the spanwise component expected to be important in mixing and part of the expectedly larger vertical flow component and ii) to keep the angle small so that approximately equal segments axially of each jet could be measured; that is, with a larger angle the ultrasound beam cuts different axial segments of each jet.
3) UDV measurements were made with a single Delrin-encased (up to 80°C) transducer (Imasonic-France) placed in-situ (underwater) and affixed to a vertically traversing bridge. Experience accumulated has shown the following: i) injection of Expancel tracer particles, 80 μm in nominal size at trace amounts (approximately 100g/3988 liters), upstream of the nozzle was sufficient to record the desired velocity profiles, ii) the Delrin casing is hygroscopic, absorbs and swells as a result of water retention such that after 6 months to 1 year of continuous immersion, the transducer may irreversibly malfunction, iii) the same Expancel particles could be used for both UDV and PIV and iv) wetting of the transducer's face was not a problem.
4) Two stainless-steel encased transducers (Imasonic-France) were placed in-situ and affixed to a holder. We could only acquire partially satisfactory velocity data due to electrical noise. The stainless-steel casing conducts electrical noise, from the electrical pump and other sources directly into the signal processor of the UVP and overwhelms the velocity echoes. Thus, electrical isolation is necessary to detect the velocity signal when using a stainless-steel casing.

This concludes analysis of the Phase I data set.

In the period following Phase I, additional data were taken while simultaneously installing a second independent velocimetry technique, Particle Image Velocimetry (PIV). The second velocimetry technique serves several purposes, these being: 1) to foremost verify UDV data in water which we cannot do in opaque sodium and 2) enhance our analysis via acquisition of planar data with PIV, as opposed to data along the ultrasound beam.

Nomenclature

c: acoustic velocity in medium, [m/s]
D_h: hydraulics diameter of the inlet channel [mm]; = $4A/P_w$ where A is area and P_w, the wetted perimeter
dT0, dT5: same as ΔT_{hc}=0°C and ΔT_{hc}=5°C respectively
f (*f*), f_{max} : frequency of jet oscillation, maximum frequency (based on power), [Hz]
f_d, f_0: Doppler shift frequency, initial frequency of ultrasound
Gr: Grashof number, = $(g\beta\Delta T\, z^3 / \nu^2)$
L, L_{dist}, l_{ch} : measurement distance, channel distance, both pertain to UVP, length of the inlet channel [mm]
Pr: Prandtl number, = (ν / α)
r: velocity ratio, =U_{hot}/U_{cold}
r^2 (R^2, R2 in figure): correlation coefficient
R, $r_{1/2}$ (r-1/2, $R_{1/2}$, R1/2, R-1/2): radius, jet half-radius; pertains to single-jet
Re, Re_0: Reynolds number of inlet channel, Reynolds at inlet, = (UD/*v*) or (Uz/ *v*)
T: jet and ambient temperature; Figs. 4-6
T_{hot} (T_h ,T_H, TH) T_{cold} (T_c ,T_C, TC), ΔT_{hc} (ΔT): temperature of "hot" jet relative to the "cold" jet, temperature of the "cold" jet and the temperature difference between the two at the exit, [°C]
U_{av} (or U_{avg}),$U_{hot,exit}$,$U_{cold,exit}$: Average velocity, velocity of hot cold) jet at exit, [mm/s]
$U_{ctr,max}$,U_{max} (U_m): Maximum centerline velocity of the velocity profile, maximum velocity, [mm/s]
U_o, $U_{o,av}$: Velocity at the exit of the nozzle, average velocity at exit[mm/s]
U, U_x , U_y: magnitude of velocity, axial and spanwise velocities, =$(U_x+U_y)^{1/2}$
U(ΔT_{hc}=*xx*°C): velocity pertaining to triple-jet with hot-to-cold jet temperature difference of *xx*°C
U(z), U_{av}(z45): velocity as a function of z, average velocity at z=45 mm from the jet exit
u_{rms}, u' root-mean-square velocity, fluctuating component of velocity
u, v, w (*u,v,w*): the x, y and z components of velocity
V, V_{exit}, V_H, V_C : generic velocity, jet exit velocity, velocity of hot and cold jets respectively, [m/s]
x, X, x/D|$_{ctr}$: : transverse or spanwise axis, x/D=0 designates the centerline
z, Z, z_{uc}: axial distance down the channel as measured from the inlet's exit, core length of single jet [mm]

Greek Symbols

ρ, $\rho_{\infty(ambient)}$, ρ_{exit} : density, ambient density, density at exit, [kg/m^3]
v: kinematic viscosity, [m^2/ s]

Abbreviations and notations

LDV, LDA: laser Doppler velocimetry, laser Doppler anemometry
ML: measurement line of ultrasound beam
OD: outer diameter
poly.: refers to "polynomial" regression
RMS, rms: root-mean-square
SD, SD_z , SD_z(z): standard deviation, standard deviation of z-component of velocity, SD_z as a function of z
-t1, -t2: trial one and two; Fig. 36.
T/C: thermocouple
TDX, tdx: transducer
UDV: ultrasound Doppler velocimetry
UVP: utrasonic velocity profile monitor
U(1j), U(3J): velocity pertaining to the single- and triple-jet respectively
U(1j), U(3J): velocity pertaining to the single- and triple-jet respectively
US: ultrasound
1j,3j: refer to single and triple-jet respectively
1JR, 3JR, 3JL: single-jet UVP data taken from right, triple-jet UVP data taken from right and left respectively

References

1. D.S. Wood, Proposal for design against thermal striping, Nuclear Energy, vol. 19, no. 6, 433-437, 1980.

2. J. E. Burnings, LMFBR thermal-striping evaluation, Interim report, EPRI-NP-2672, Research Project 1704-11, prepared by Rockwell International Energy Systems Group, 8900 De Soto Avenue, Canoga Park, CA, USA, 91304, October 1982. Prepared for EPRI. EPRI Project Manager: J. Matte III.

3. C. Betts, C. Bourman and N. Sheriff, Thermal striping in liquid metal cooled fast breeder reactors, 2nd Int'l Topical Mtg. on Nuclear Reactor Thermal Hydraulics, NURETH-2, Santa Barbara, CA, USA, vol. 2, 1292-1301, 1983.

4. C. Betts et al., Air as an analogue fluid for liquid sodium in thermal striping phenomena, 4th Int'l Conf. on Liquid Metal Engineering and Technology, Avignon, France, 17-21 October 1988.

5. S. Moriya et al., Thermal striping in coaxial jets of sodium, water and air, 4th Int'l Conf. on Liquid Metal Engineering and Technology, Avignon, France, 17-21 October 1988.

6. S. Moriya, S. Ushijima, N. Tanaka, S. Adachi and I. Ohshima, Prediction of Thermal Striping in Reactors, Int'l Conf. Fast Reactors and Related Fuel Cycles, Oct. 28 - Nov. 1, Kyoto, Japan, vol. 1, 10.6.1 - 10.6.10, 1991.

7. T. Muramatsu, "Development of thermohydraulics computer programs for thermal striping phenomena", Specialists meeting on correlation between material properties and thermohydraulics conditions in LMFRs, IAEA Working Group on Fast Reactors, IWGFR/90, Aix-en-Provence, France, November 22-24, 1994.

8. T. Muramatsu, Investigation of Sodium Temperature Fluctuation Characteristics Related to Thermal Striping Phenomena Using the DINUS-3 Code, Proc. ASME PVP Conf., Vol. 270, Minnesota, USA, 1994.

9. A. Tokuhiro and H. Miyakoshi, An experimental investigation on mixing of a vertical cooled jet with two adjacent heated jets. Part I: Some initial results of Ultrasound Doppler Velocimetry measurements, 8th Int'l. Topical Meeting Nuclear Reactor Thermal-Hydraulics, Kyoto, Japan 30 September - 4 October 1997.

10. N. Kimura, A. Tokuhiro and H. Miyakoshi, An experimental investigation on mixing of a vertical cooled jet with two adjacent heated jets. Part II: Some initial heat transfer and temperature measurement results, 8th Int'l. Topical Meeting Nuclear Reactor Thermal-Hydraulics, Kyoto, Japan 30 September - 4 October 1997.

11. D. Tenchine and H.-Y. Nam, Thermal hydraulics of co-axial sodium jets, Am. Inst. Chem. Engrs. Symp. Ser., vol. 83, no. 257, 151-156, 1987.

12. D. Tenchine and J.-P. Moro, Comparative analysis of sodium and air mixing jets experiments, 8th IAHR Working Group Mtg. Adv. Nucl. React. Thermohydraulics, June 13-15, Rez, Czech Rep., 1995.

13. N. P. Cheremisinoff, editor, Encyclopedia of Fluid Mechanics, Dynamics of Single-Fluid Flows and Mixing, vol. 2, Gulf Publishing Co., Houston, 1986.

14. B. Gebhardt, Y. Jaluria, R. L. Mahajan and B. Sammakia, Buoyancy-Induced Flows and Transport, Reference Edition, Hemisphere Publishing Corporation, New York , 1988, pp. 657-697.

15. C.J. Chen and W. Rodi, Vertical turbulent buoyant jets - A review of experimental data, Pergamon Press, Oxford, England (1980).

16. H. Schlichting, Boundary-layer theory, McGraw-Hill, New York (4th ed.), 1960.

17. Ultrasound Velocity Profile (UVP) monitor, Model X-1, Met-Flow SA, Lausanne, Switzerland, 1992.

18. A. T. Tokuhiro and H. Miyakoshi, Thermal Striping --- An experimental investigation on mixing of a vertical cooled jet with two adjacent heated jets. Part I: Some initial results of Ultrasound Doppler Velocimetry measurements, PNC ZN9410 96-126, April 1996.

19. N. Kimura, A. Tokuhiro and H. Miyakoshi, Experimental study for thermal striping phenomena of parallel triple-jet --- Effects of the difference between hot jets and cold jet in discharged temperatures and velocity on convective mixing ---, PNC TN9410 96-296, October 1996 (in Japanese).

20. A. T. Tokuhiro, Experimental investigation of a vertical planar jet by ultrasound and laser Doppler velocimetry, J. Nucl. Sci. and Technol., 36[6], June 1999 (to appear).

21. Kataoka, K. : "Modeling turbulent jets with variable density", in "*Encyclopedia of Fluid Mechanics, Dynamics of Single-Fluid Flows and Mixing* ", Cheremisinoff, N.P., Ed., vol. 2, chapter 20, Gulf Publishing Co., Houston, USA (1986).

22. K. Kataoka and T. Takami, Experimental study of eddy diffusion model for heated turbulent free jets, Am. Inst. Chem. Engrs. J., vol. 23, 889-896 November 1977. present report used data of author contained in Ref. 13)

23. S. Corrsin and M. S. Uberoi, Further experiments on the flow and heat transfer in a heated turbulent air jet, NACA TN 1865 1949. (present report used data of authors contained in Ref. 13)

24. W. R. Warren, An analytical and experimental study of compressible free jets, Ph.D. thesis, Princeton University, Princeton, N.J., USA 1957. (present report used data of author contained in Ref. 13)

25. Hinze, J.O., van der Hegge Zijnen, B.G. : *Appl. Sci. Res.*, **1A**, 435 (1949).

26. Kataoka, K., Shundoh, H., Matsuo, H. : *J. Chem. Eng. Japan*, **15**, 17 (1968).

27. Donaldson, C. duP., Gray, A.E.: *AIAA J.*, 4, 2017 (1966).

Acknowledgments

The first author would like to thank JNC for his appointment as JNC International Fellow. The authors also appreciate the efforts of Mr. Ito, Mr. Onuma and others of Joyo Sangyo who diligently conducted the experimental measurements, maintained the data and prepared the UVP and temperature data which were analyzed in order to prepare this report. The author also acknowledges the assistance of Ms. Kawashima of NESI in data analysis.

Tables, Figures and Appendices A-E.

Table 1. Summary of single- and triple-jet cases for which UDV data was taken.

Case No.	Case Name	No. of files	No. of Jets	TDX Orient.	Uav,exit	Thot,exit	Tcold,exit	Traverse range	Traverse increments	TDX facing	Channel Distance	Starting Channel	Ending Channel	Primary Frequency	Sound Velocity
				[deg]	[m/s]	[C]	[C]	[mm]	[mm]		[mm]	[mm]	[mm]	[Hz]	[m/s]
1A	J1E_R	54	1	10	0.5	NA	25		5	Right	2.22	76	360	1953	1480
1B	J1E_R	see above	1	10	0.5	NA	25		5	Right	5.18	76	739	976	1480
1C	J1E_R	see above	1	10	0.5	NA	25		5	Right	5.18	5	668	976	1480
2A	J1E_R2	78	1	10	0.5	NA	25		5	Right	2.22	76	360	1953	1480
2B	J1E_R2	see above	1	10	0.5	NA	25		5	Right	5.18	5	668	976	1480
3	J1E_R3	68	1	10	0.5	NA	25		5	Right	5.18	5	668	976	1480
4	J1E_R4	90	1	10	0.5	NA	25		5	Right	5.18	5	668	976	1480
5	J1E_L1	72	1	10	0.5	NA	25	0-175	5	Left	2.22	76	360	1953	1480
6	J1E_L2	146	1	10	0.5	NA	25	180-540	5	Left	2.22	76	360	1953	1480
7	J1E_R6	102	1	10	0.5	NA	25	0-250	5	Right	2.22	76	360	1953	1480
8	J1E_R7	108	1	10	0.5	NA	25	255-520	5	Right	2.22	76	360	1953	1480
9	J1E_S1	12	1	90	0.5	NA	30	85-510(85)	85	facing down	0.74	5	91	7812	1480
10	J1E_S2	17	1	90	0.5	NA	30	85-510(85)	85	facing down	2.22	76	360	1953	1480
11	J1E_S3	6	1	90	0.5	NA	30	85-510(85)	85	facing down	2.22	76	360	1953	1480
12	J3D_F1	20	3	0	0.5	42-43	35-40								
13	J3D_L1	90	3	10	0.5	30	25	0-220	5	Left	2.22	76	360	1953	1480
14	J3D_L2	128	3	10	0.5	30	25	220-530	5	Left	2.22	76	360	1953	1480
15	J3D_R1	126	3	10	0.5	30	25	0-310	5	Right	2.22	76	360	1953	1480
16	J3D_R2	92	3	10	0.5	30	25	315-540	5	Right	2.22	76	360	1953	1480
17	J3E_F1	20	3	0	0.5	30	30	20-500	20,40,60,80, 100,120,200, 300,400,500		2.22	76	360	1953	1480
18	J3E_S1	12	3	90	0.5	30	30	85-510(85)	85	facing down	0.74	5	91	7812	1480
19	WORK	9	1			NA					5.18	76	739	976	1480
20	WORK2	8	1			NA					2.22	76	360	1953	1480

NA= not available

Table 1. Experimental conditions

Case		T05V0505	T05V1010	T10V0505	T10V1010	T05V1005	T10V1005	T10V1007	T05V1007
Hot jets	Velocity [m/sec]	0.5	1.0	0.5	1.0	1.0	1.0	1.0	1.0
	Temperature [℃]	30	35	42	42	30	40	40	32
Cold jet	Velocity [m/sec]	0.5	1.0	0.5	1.0	0.5	0.5	0.7	0.7
	Temperature [℃]	25	30	32	33	25	30	30	27
Discharged temperature difference [℃]		5	5	10	9	5	10	10	5
Discharged velocity ratio V_{cold}/V_{hot} [-]		1.0	1.0	1.0	1.0	0.5	0.5	0.7	0.7

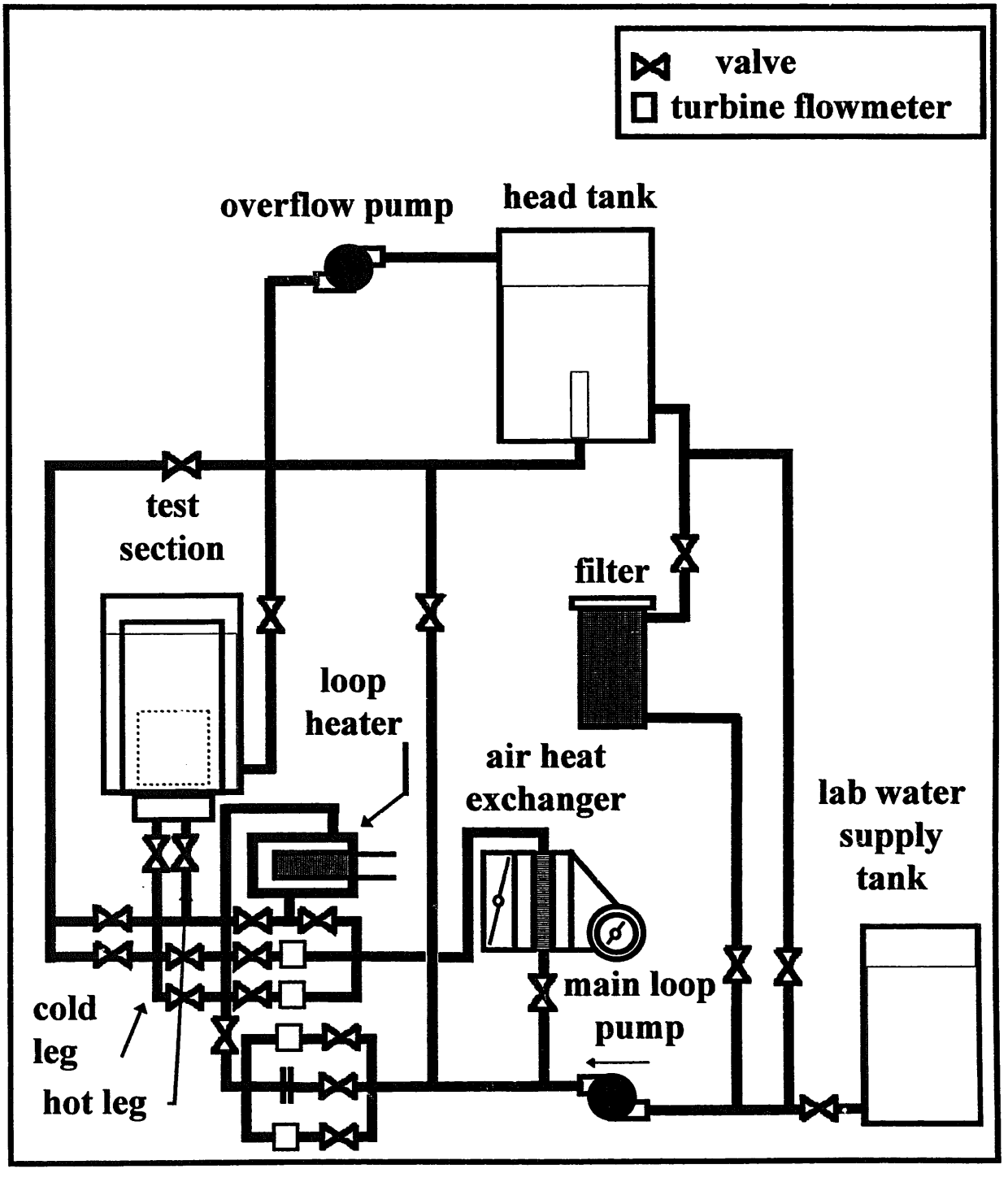

Figure 1. Schematic of experimental loop.

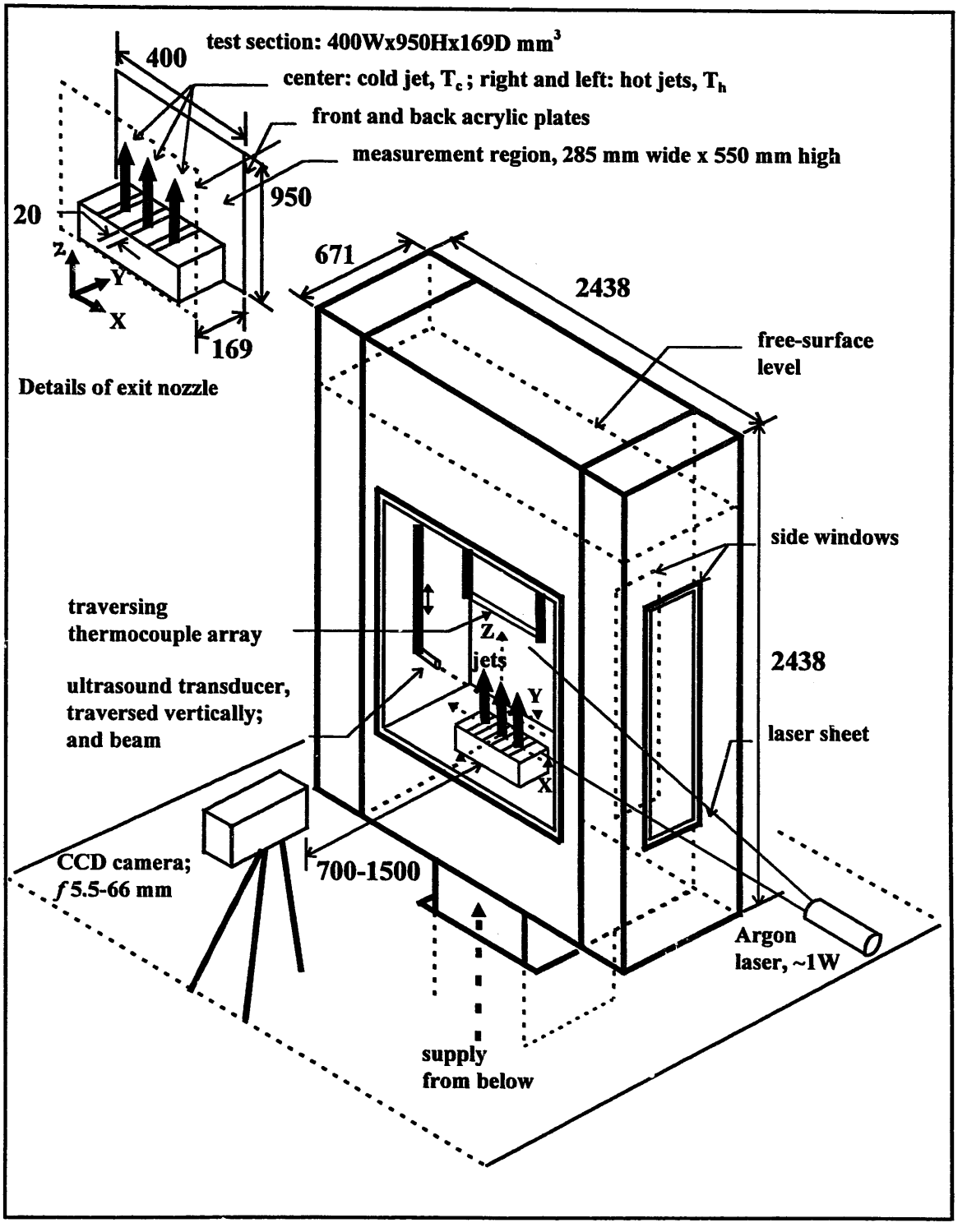

Figure 2. Schematic of experimental apparatus.

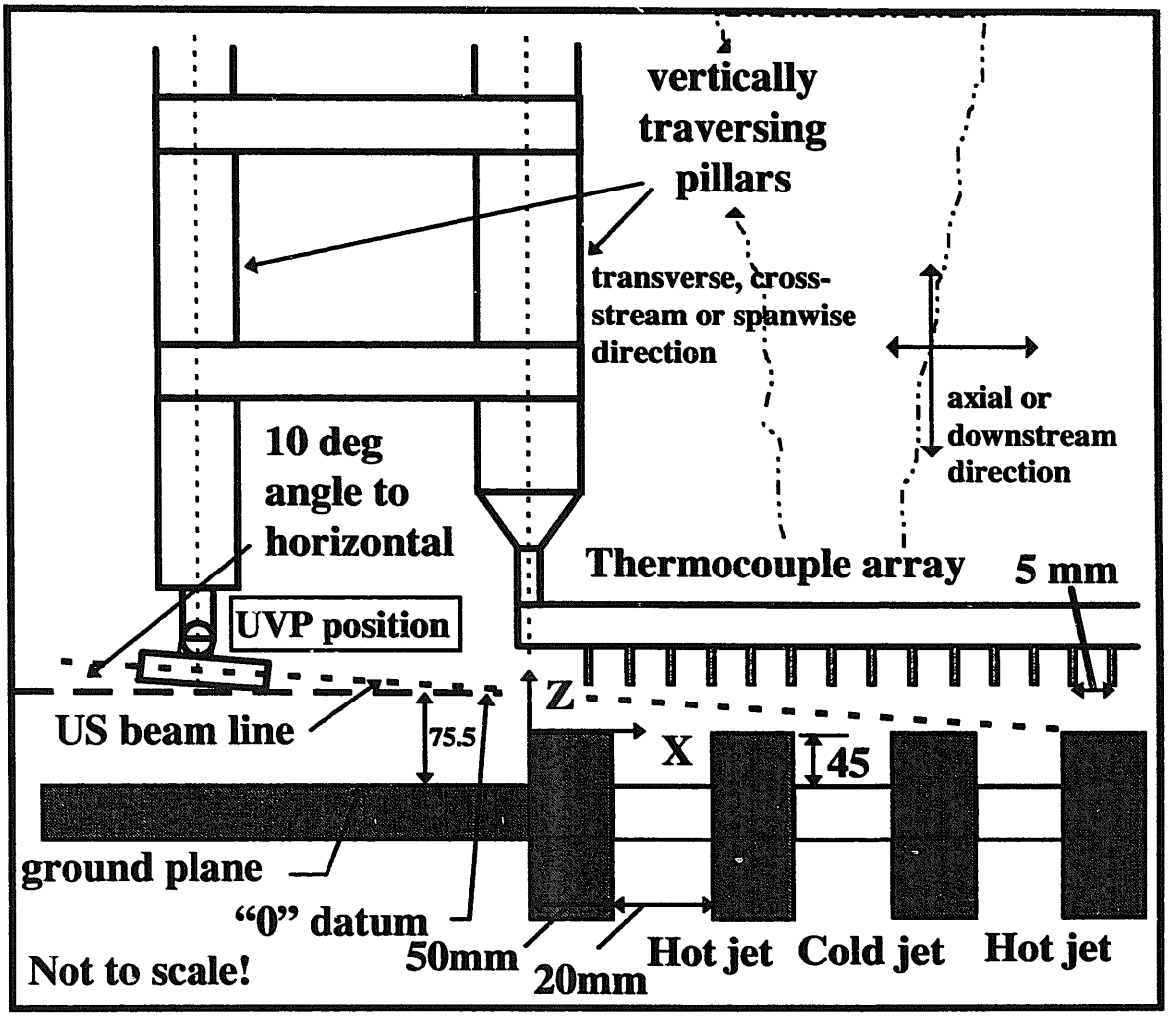

Figure 3. Schematic of instrumentation set-up. Close-up of the UVP transducer orientation and traversing thermocouple array.

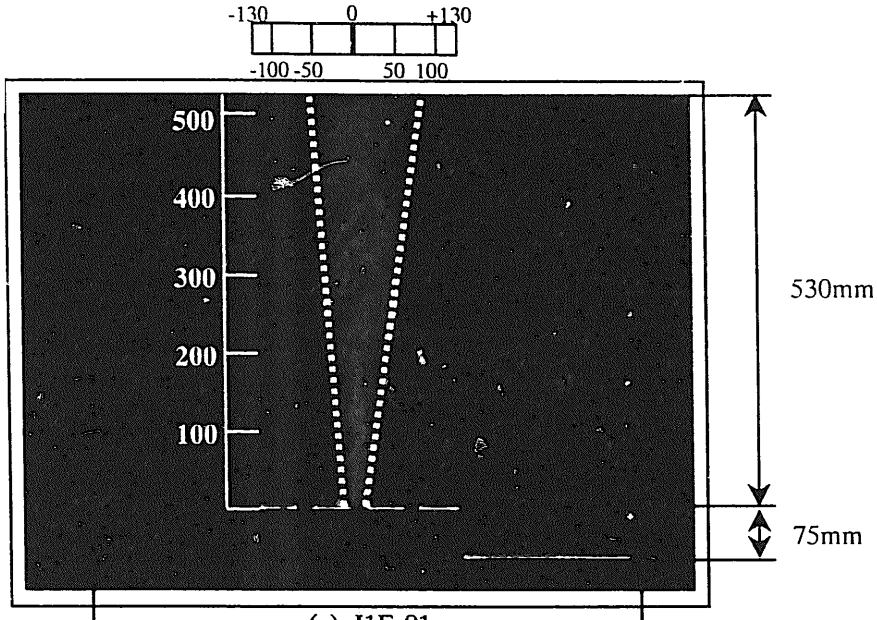

(a) J1E-01
V:0.5m/s T:30℃
700mm

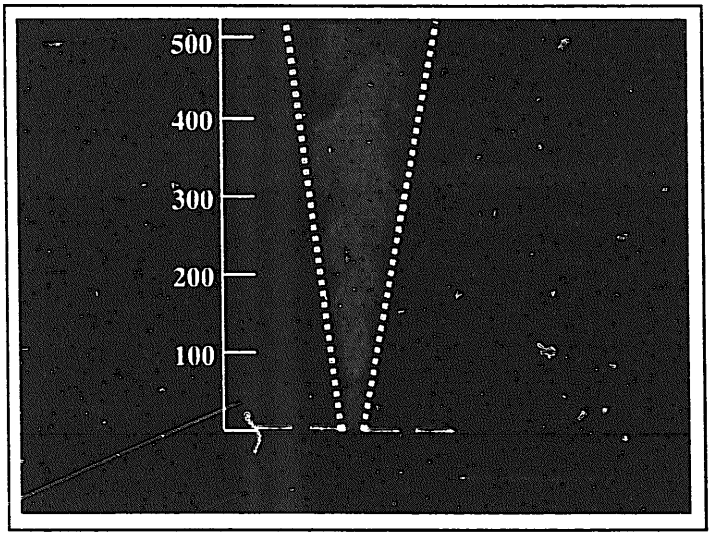

(b) J1E-02
V:1.0m/s T:30℃

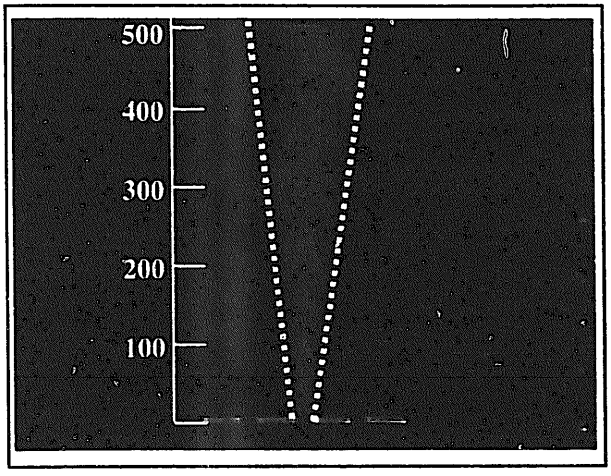

(c) J1E-03
V:2.0m/s T:30℃

Figure 4

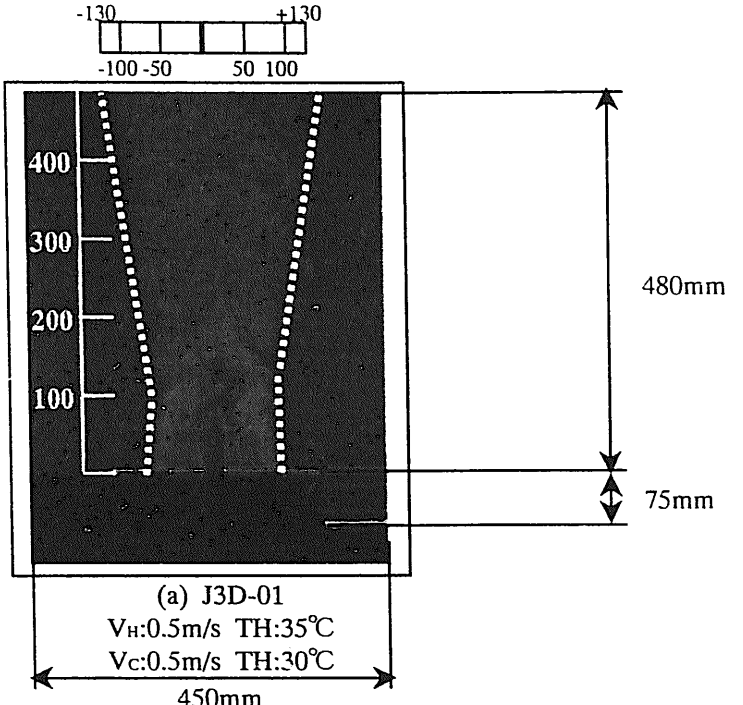

(a) J3D-01
V_H:0.5m/s TH:35℃
V_C:0.5m/s TH:30℃

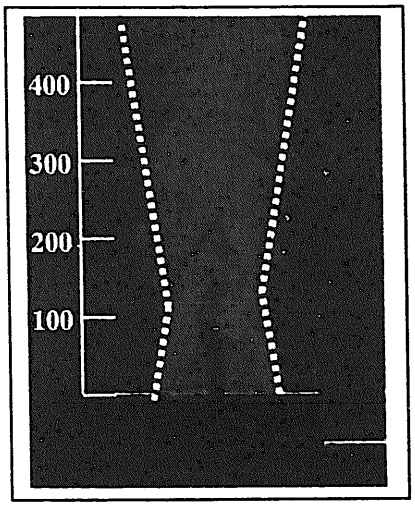

(b) J3D-07
V_H:0.5m/s TH:40℃
V_C:0.5m/s TH:30℃

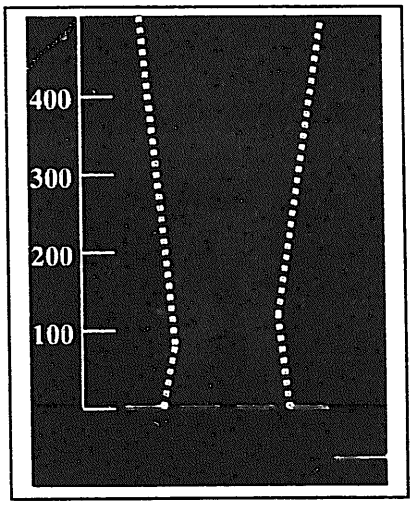

(c) J3D-08
V_H:1.0m/s TH:40℃
V_C:0.5m/s TH:30℃

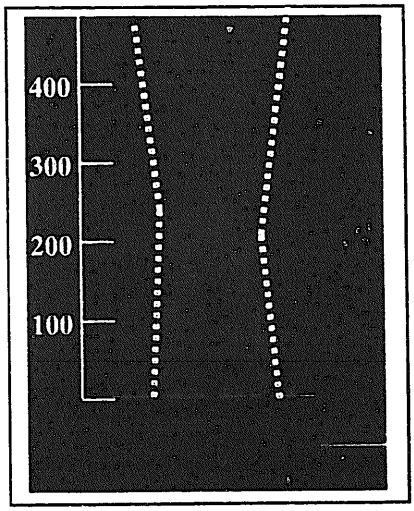

(d) J3D-14
V_H:1.0m/s TH:35℃
V_C:0.5m/s TH:30℃

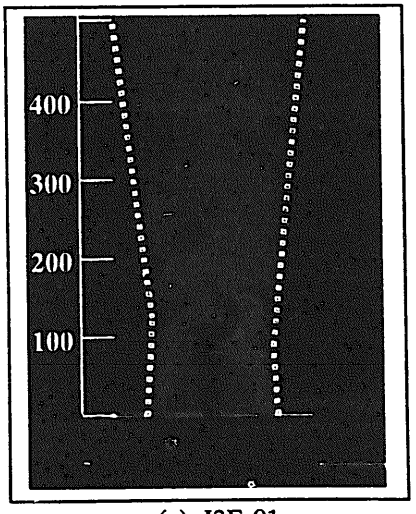

(e) J3E-01
V_H:0.5m/s TH:30℃
V_C:0.5m/s TH:30℃

Figure 5

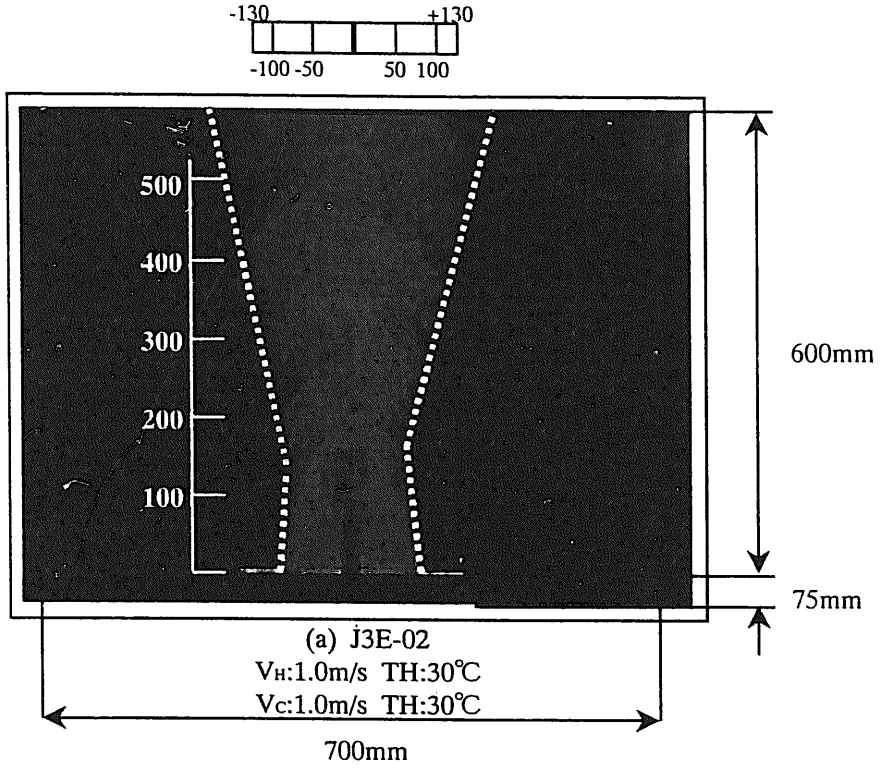
-130
+130
-100 -50
50 100
500
400
300
200
100
600mm
75mm
(a) J3E-02
VH:1.0m/s TH:30℃
Vc:1.0m/s TH:30℃
700mm

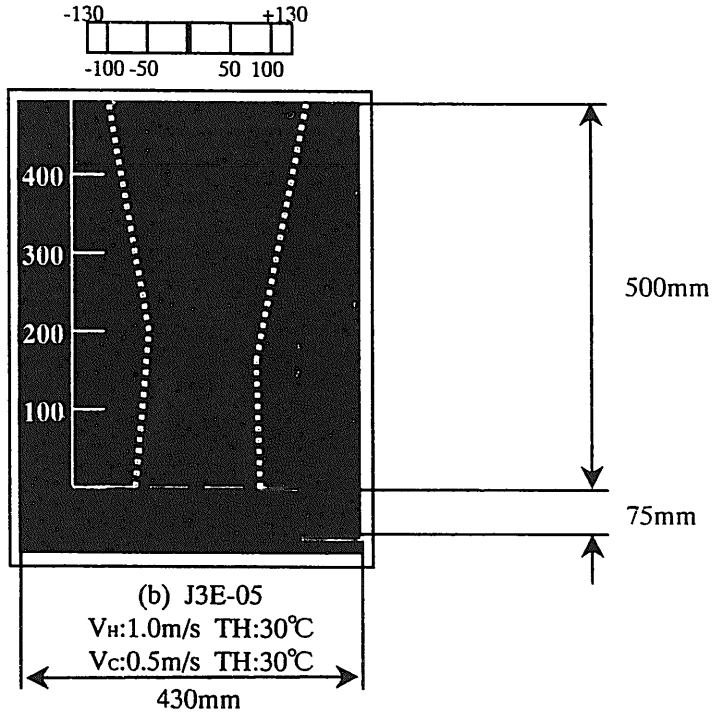
-130
+130
-100 -50
50 100
400
300
200
100
500mm
75mm
(b) J3E-05
VH:1.0m/s TH:30℃
Vc:0.5m/s TH:30℃
430mm

Figure 6

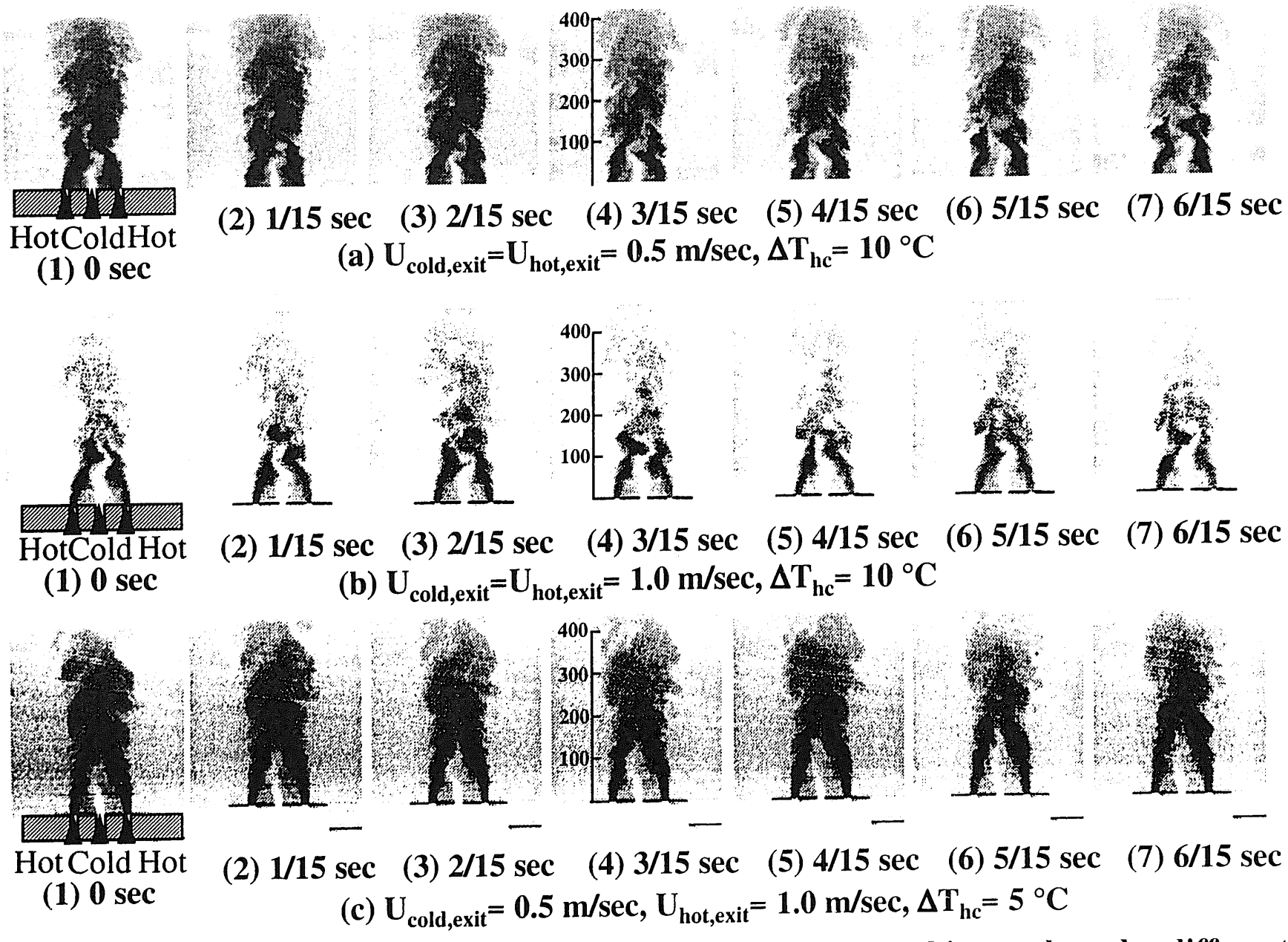

Figure 7. Digitized images of the triple-jet at 1/15th-of-a-second intervals under different $U_{cold,exit}$, $U_{hot,exit}$ and $\Delta T_{hc}(=T_{hot}-T_{cold})$ conditions.

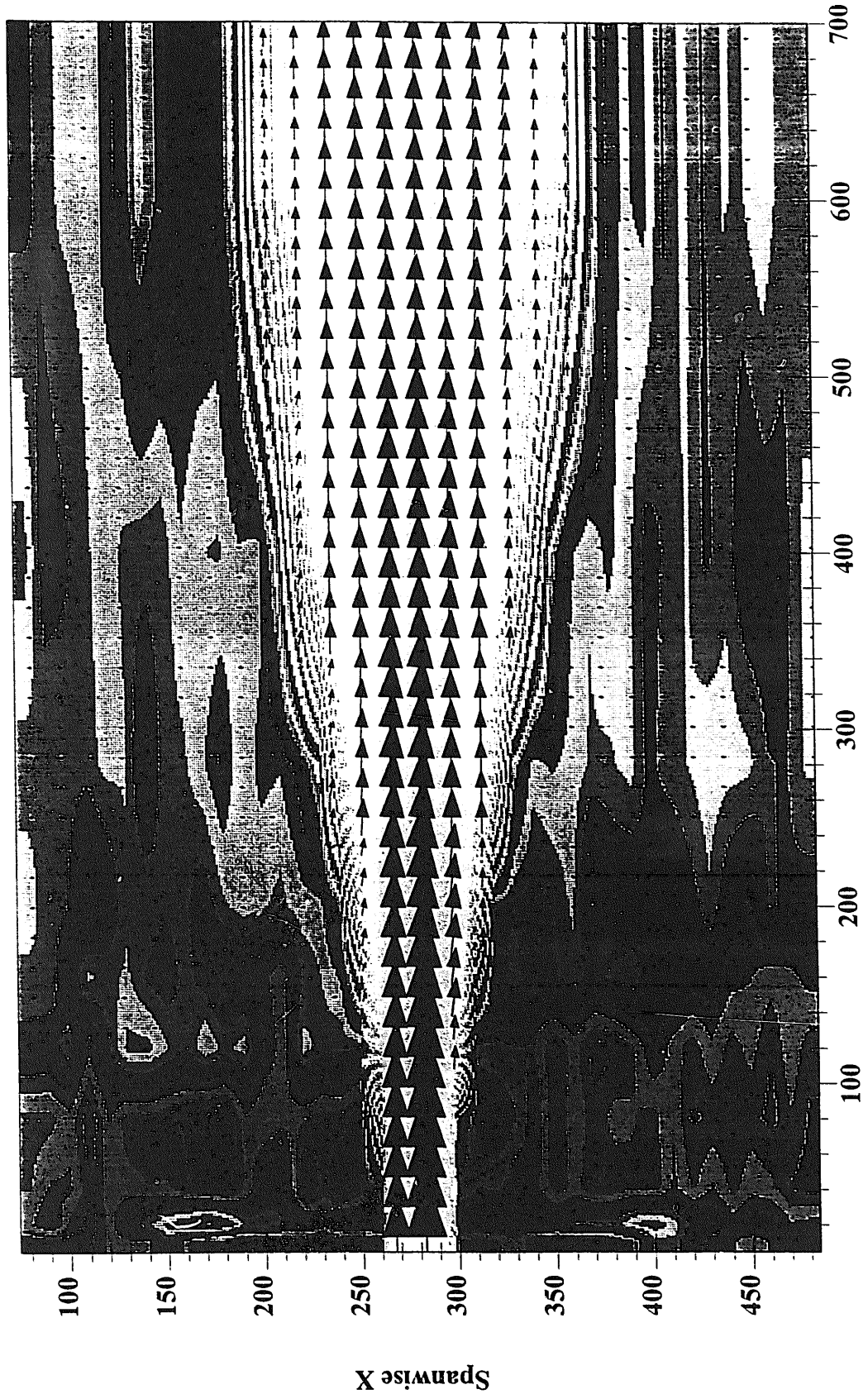
Spanwise X
100
150
200
250
300
350
400
450
Axial Z
100
200
300
400
500
600
700

Figure 8

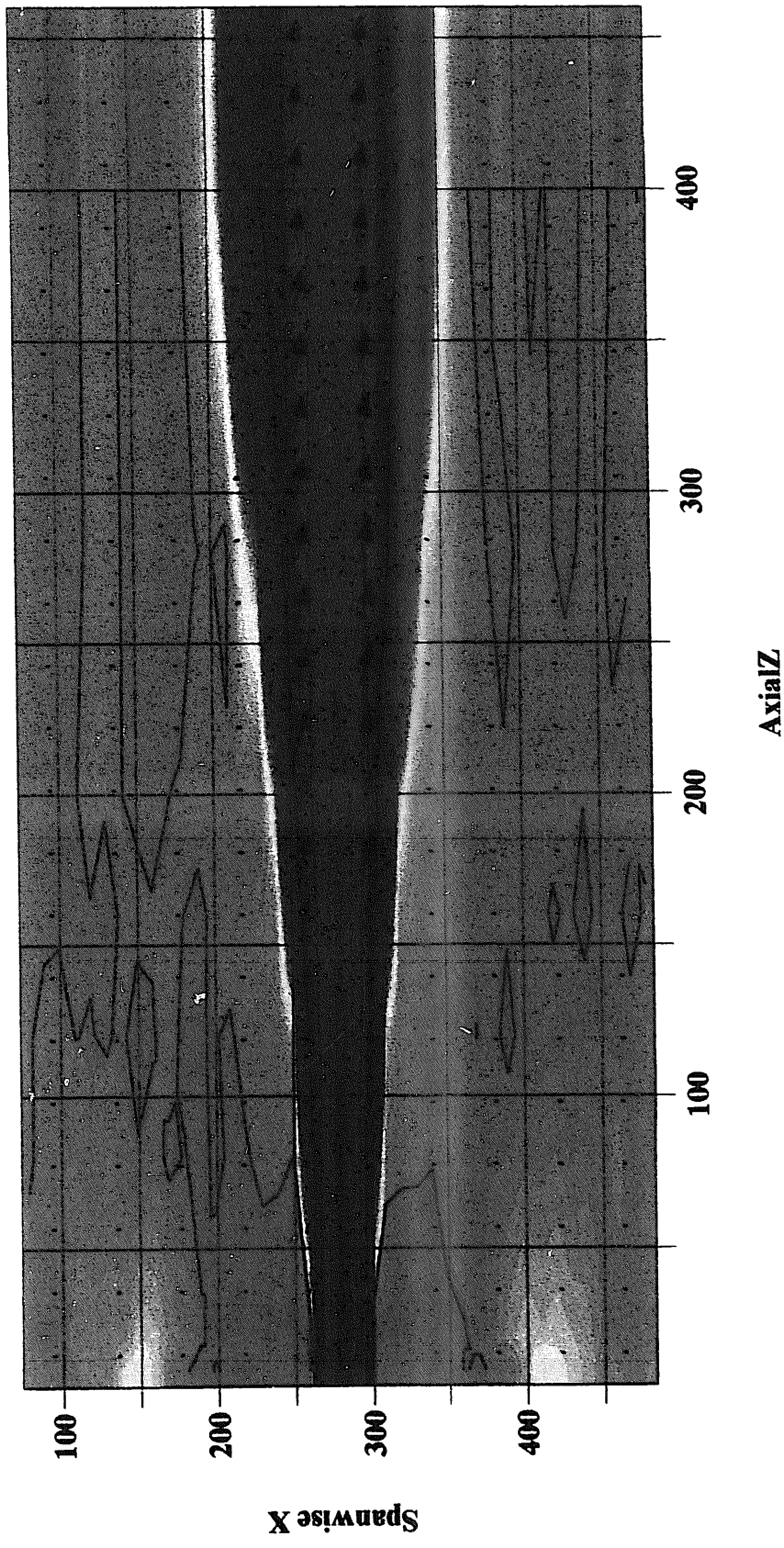

Figure 9

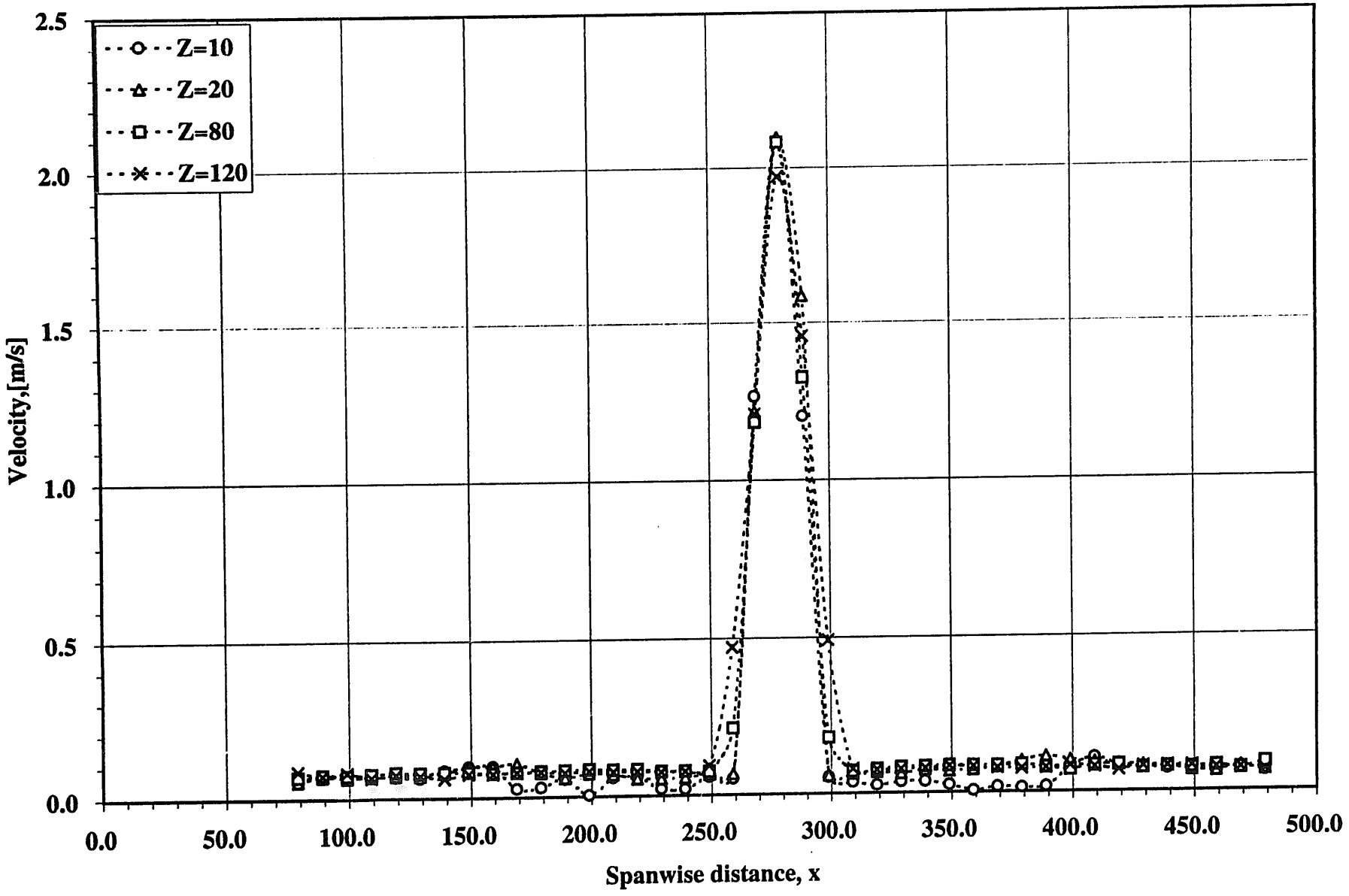

Figure 10. **Average velocity profiles with axial distance as parameter.**

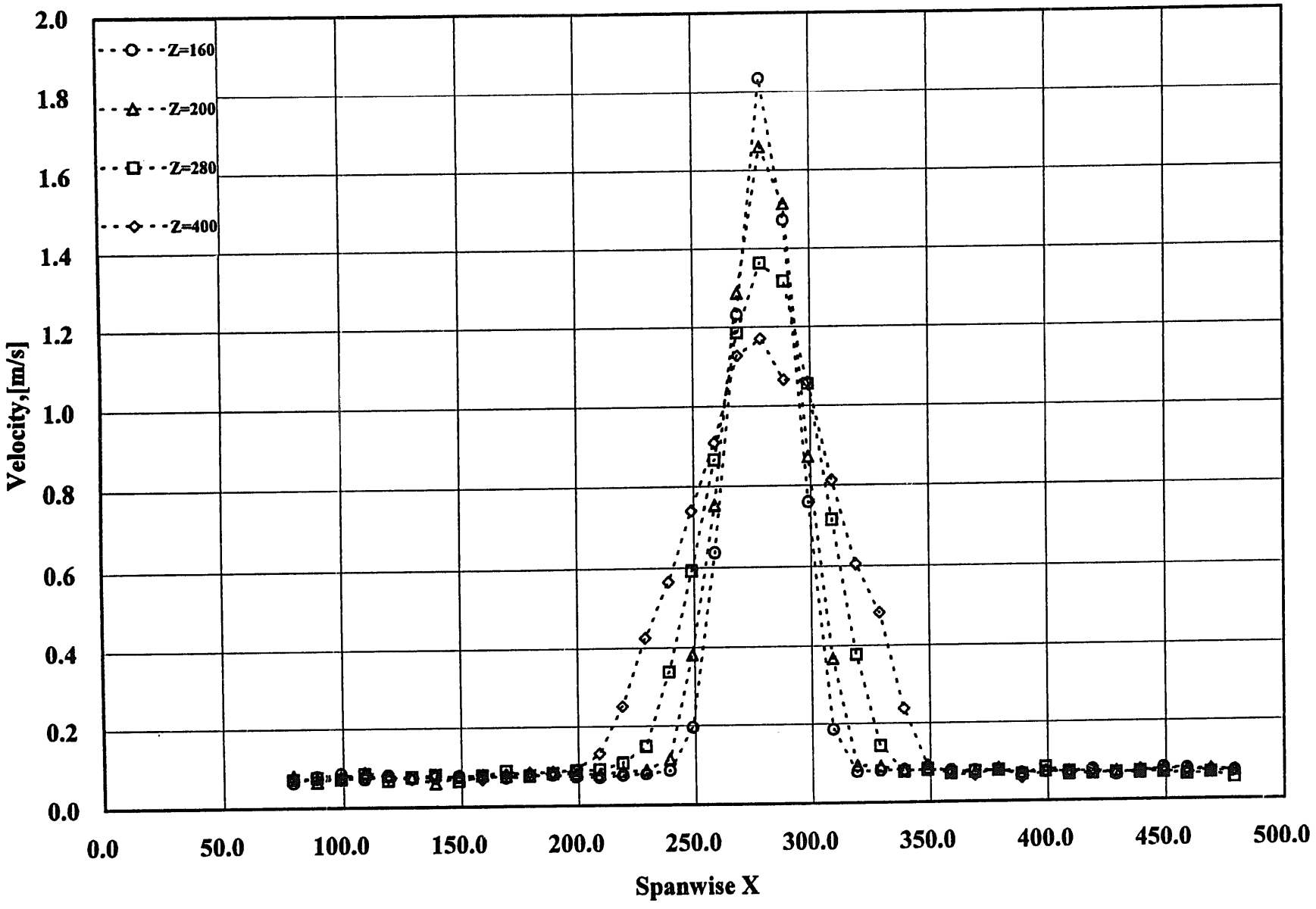
Z=160
Z=200
Z=280
Z=400
Velocity,[m/s]
2.0
1.8
1.6
1.4
1.2
1.0
0.8
0.6
0.4
0.2
0.0
0.0
50.0
100.0
150.0
200.0
250.0
300.0
350.0
400.0
450.0
500.0
Spanwise X

Figure 11

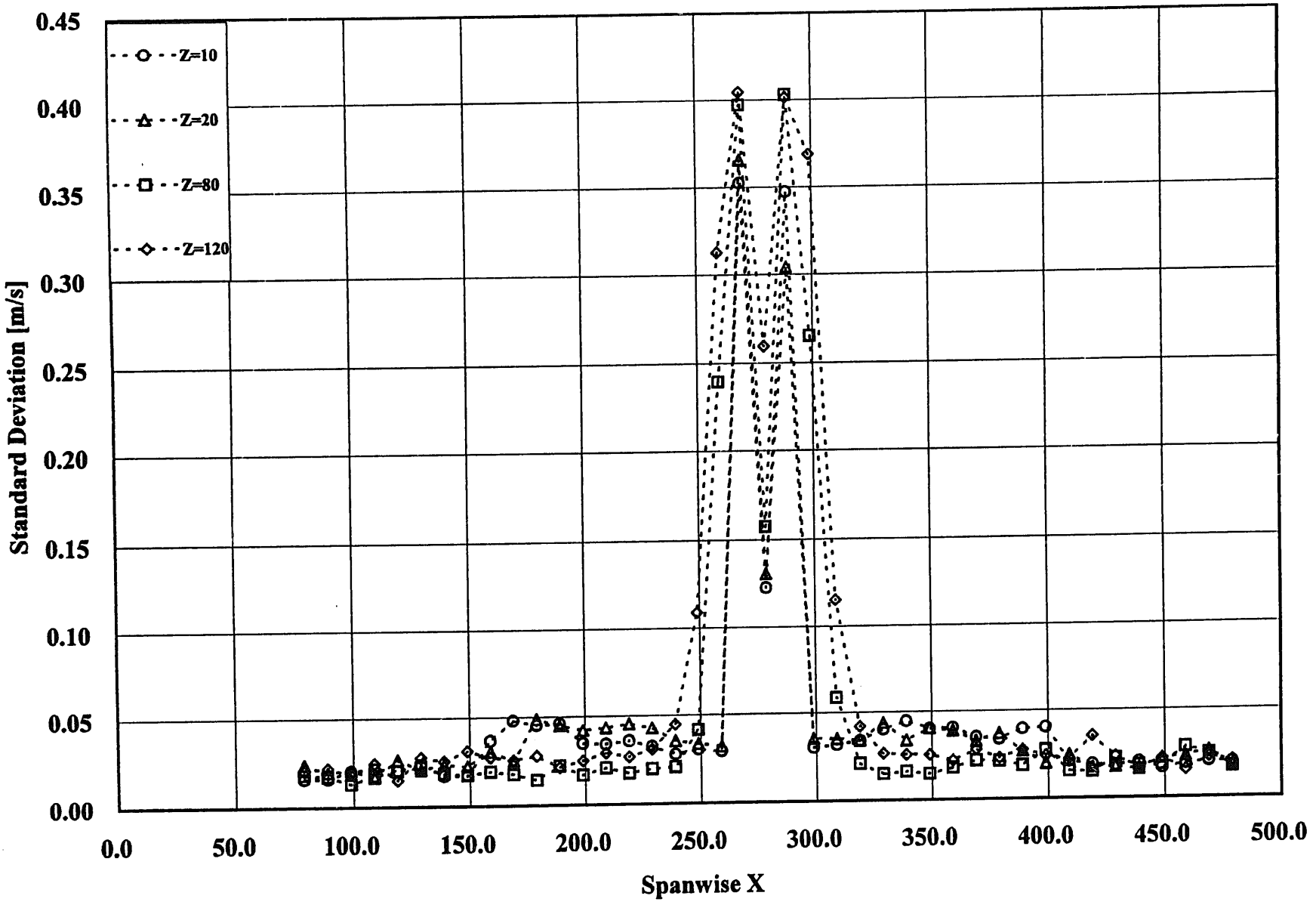
Z=10
Z=20
Z=80
Z=120
Standard Deviation [m/s]
0.45
0.40
0.35
0.30
0.25
0.20
0.15
0.10
0.05
0.00
0.0
50.0
100.0
150.0
200.0
250.0
300.0
350.0
400.0
450.0
500.0
Spanwise X

Figure 12

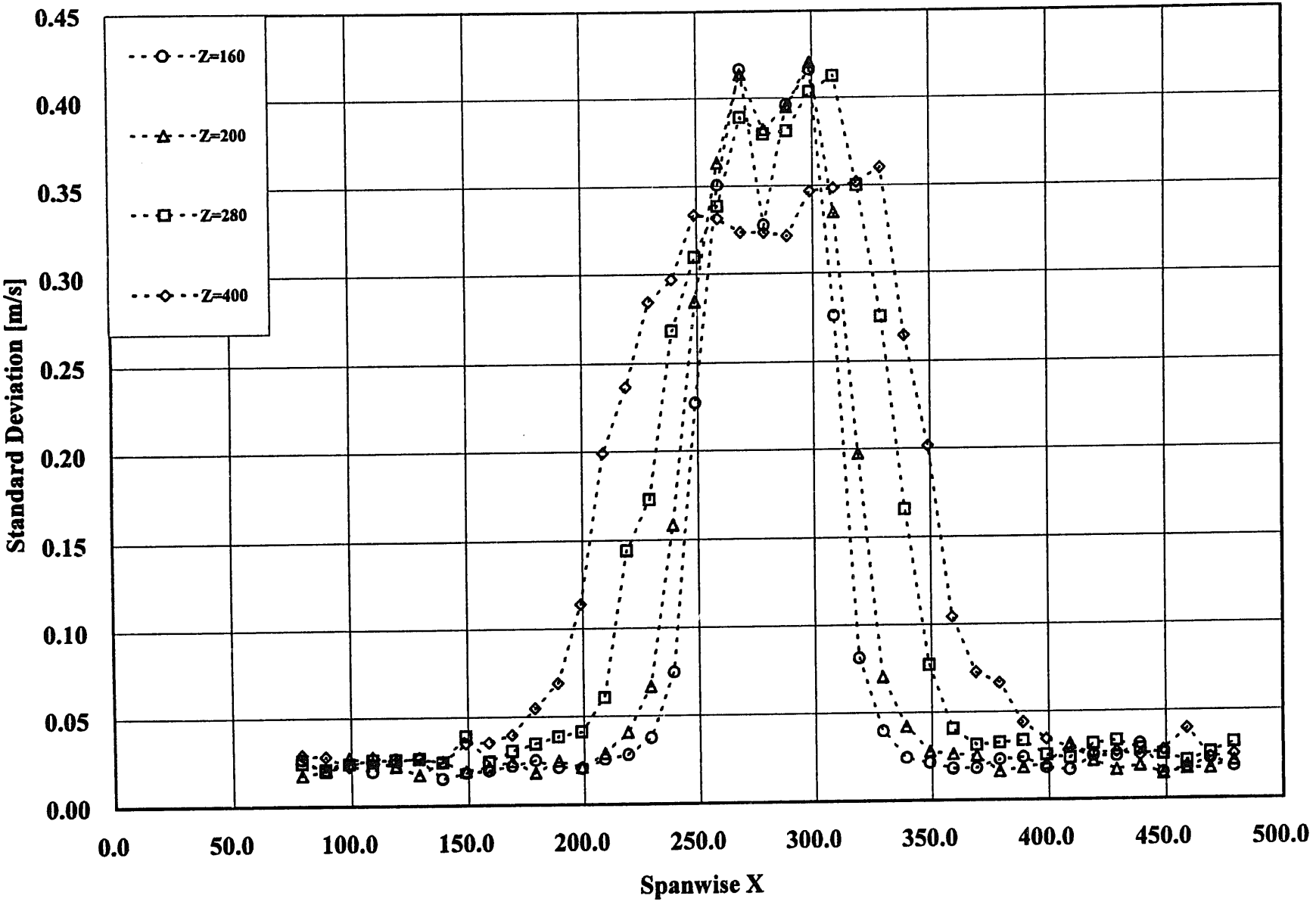
Z=160
Z=200
Z=280
Z=400
Standard Deviation [m/s]
0.45
0.40
0.35
0.30
0.25
0.20
0.15
0.10
0.05
0.00
0.0
50.0
100.0
150.0
200.0
250.0
300.0
350.0
400.0
450.0
500.0
Spanwise X

Figure 13

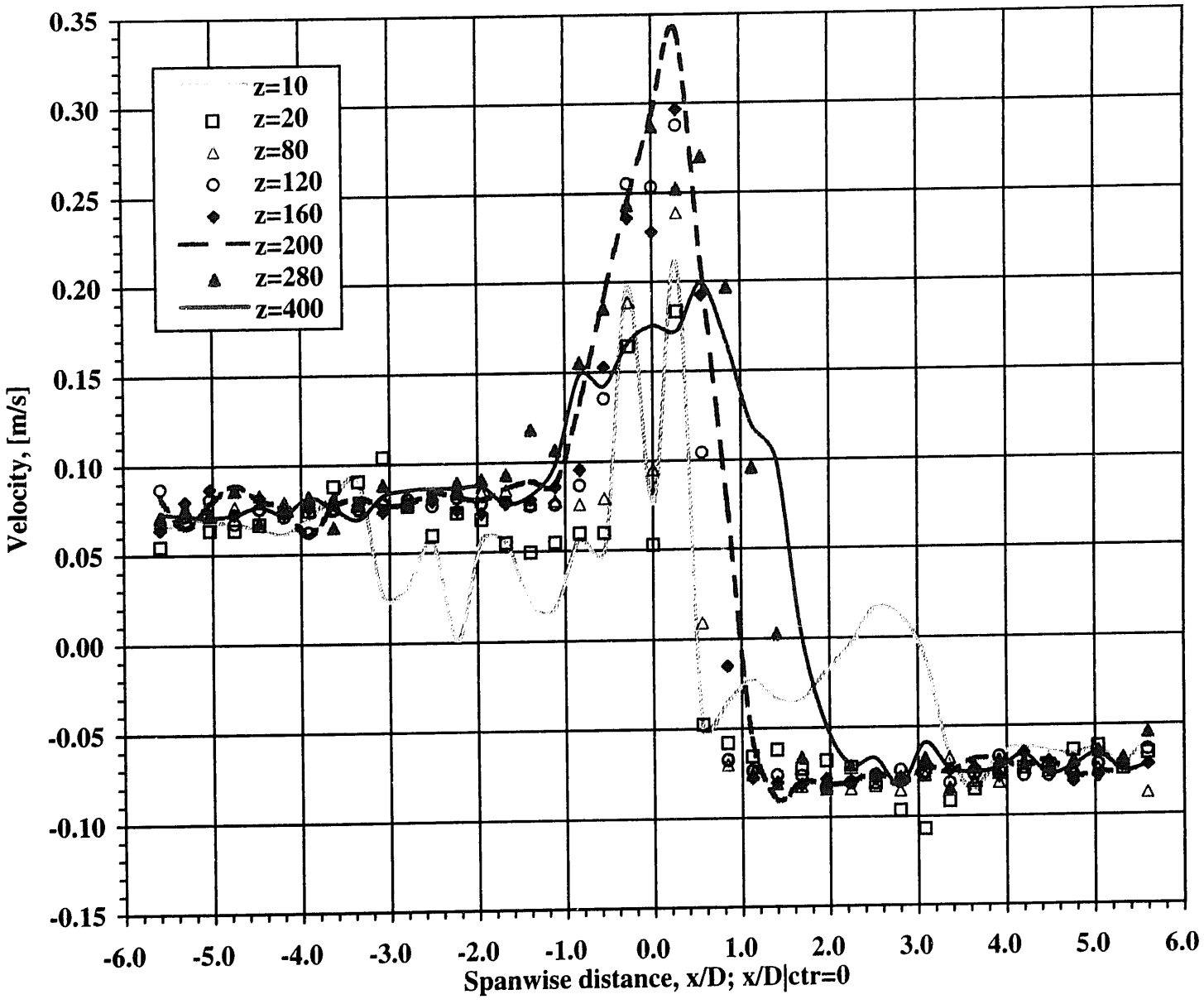

Figure 14. **Spanwise profiles of Uy-component of average velocity.**

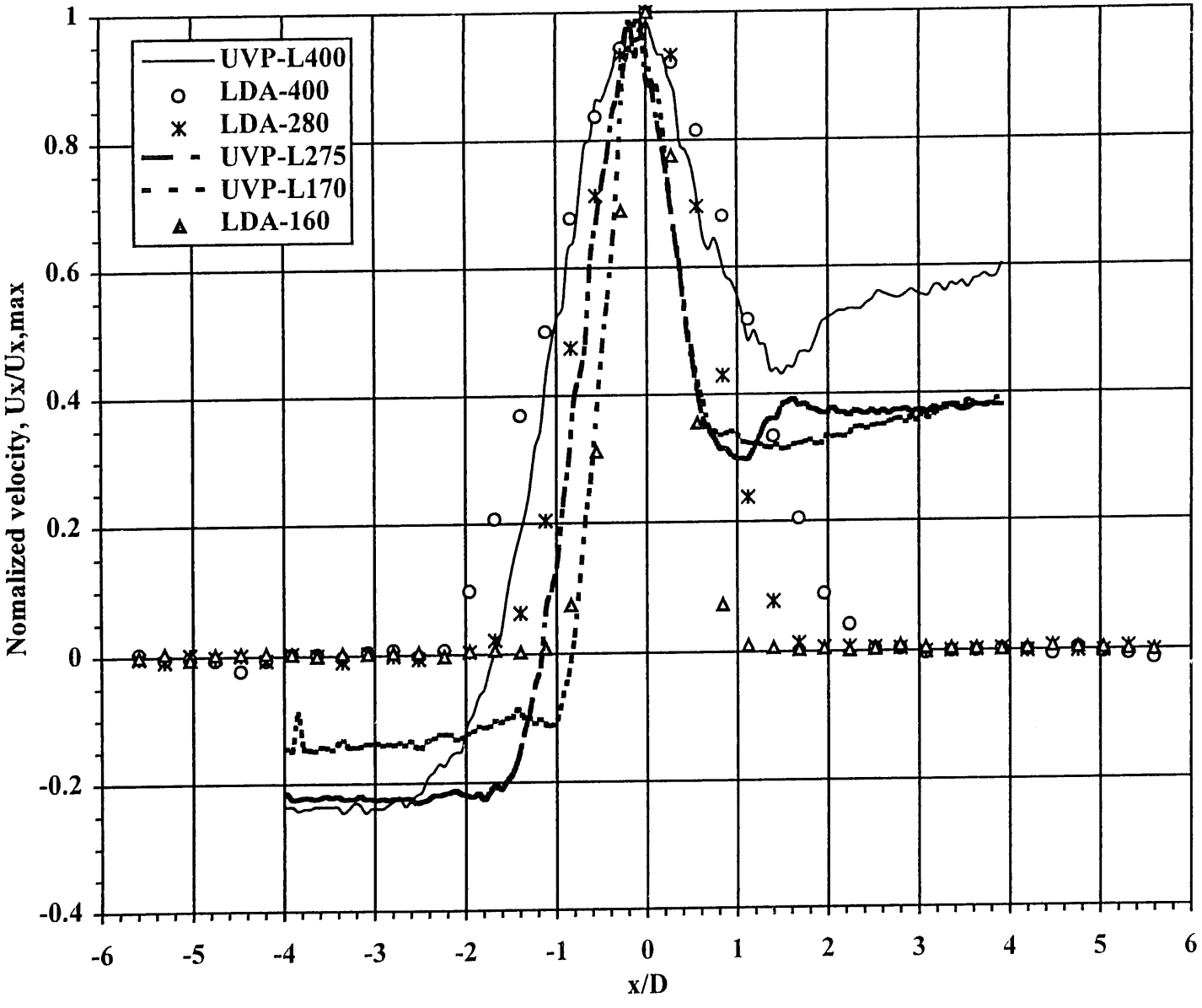

Figure 15. **Comparison of velocity profiles taken by LDA and UVP at selected axial locations.**

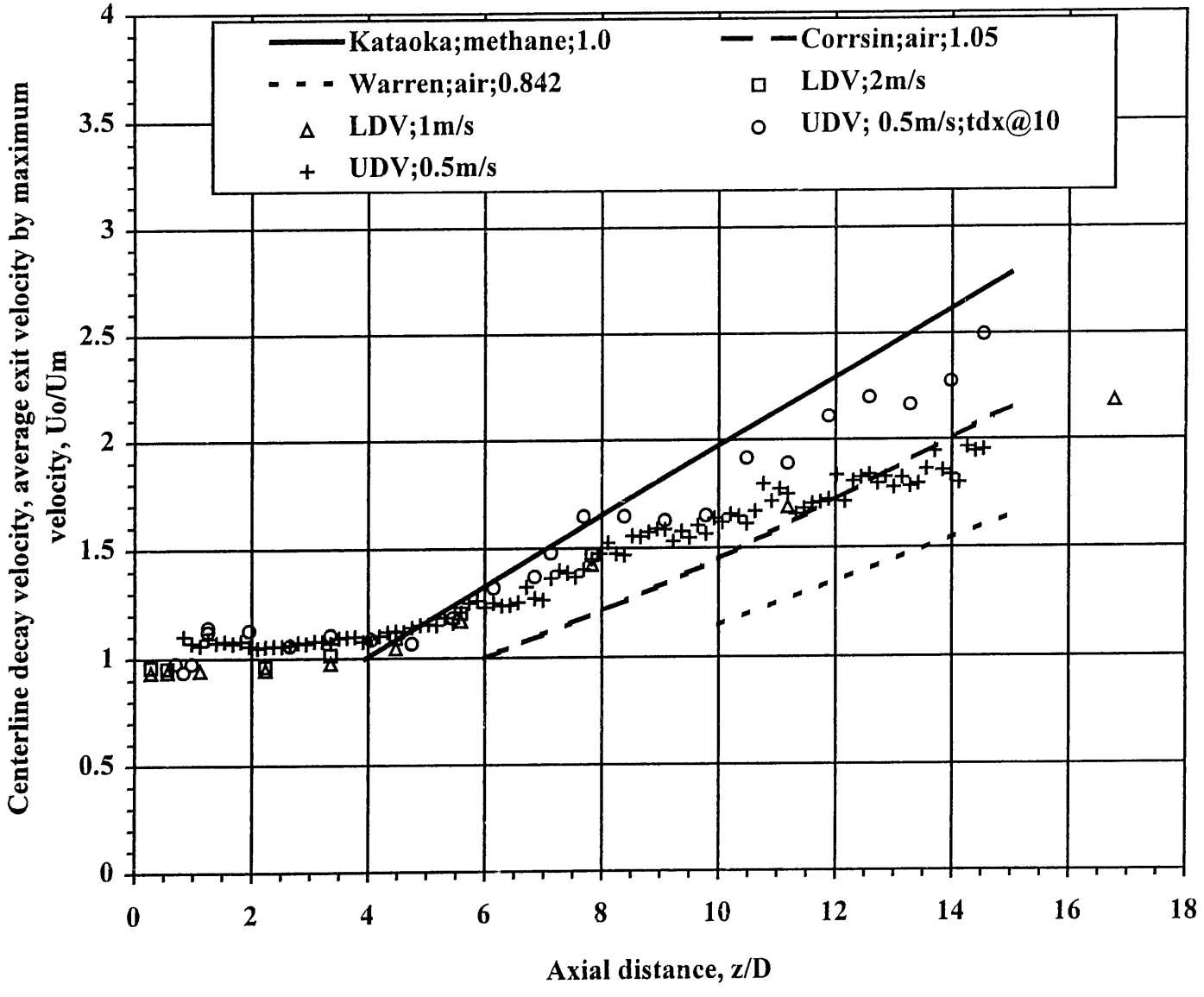

Figure 16. **Decay of the centerline velocity defined as the ratio of average exit to maximum centerline velocities, Uo/Um, versus axial distance.**

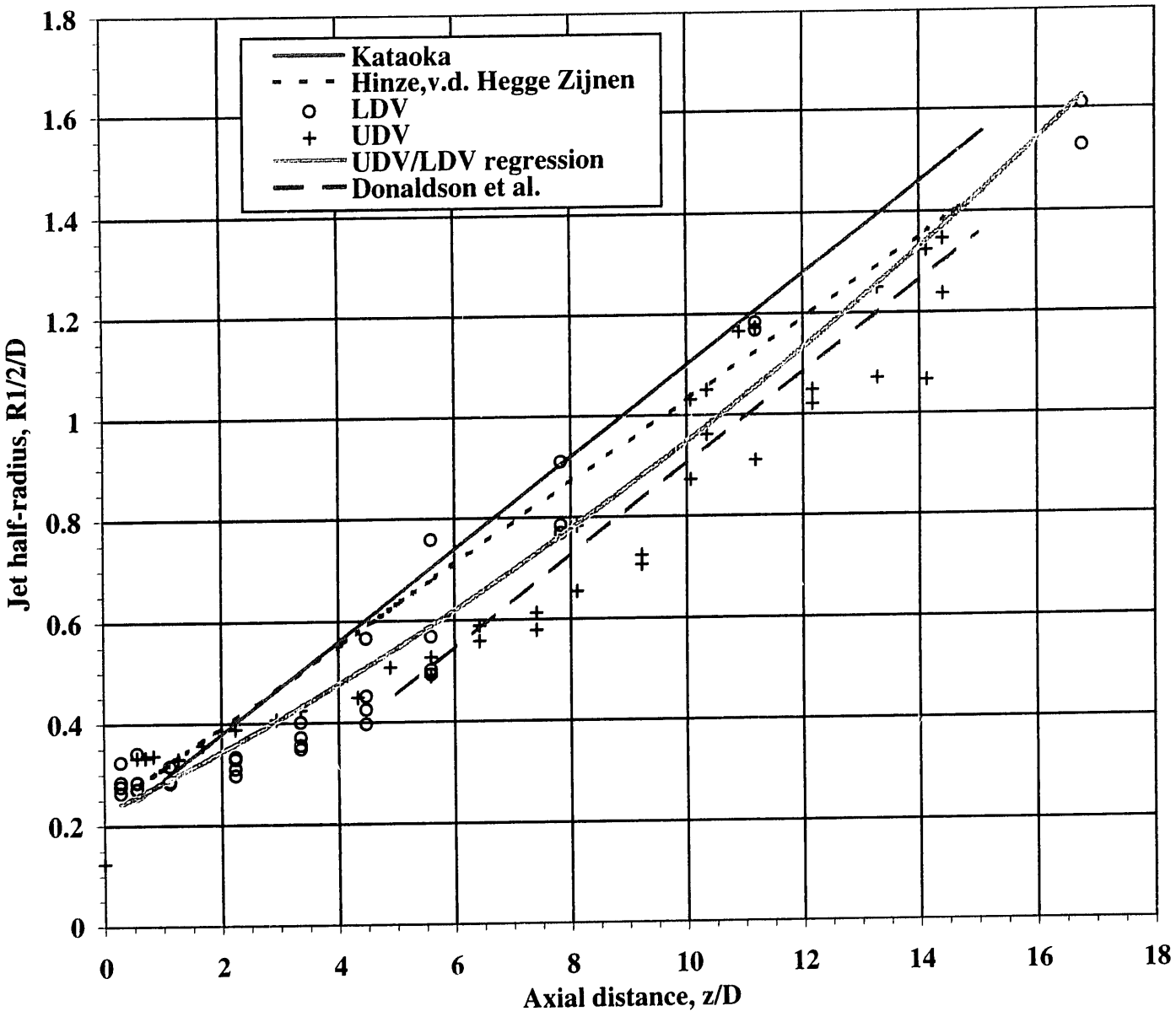

Figure 17. **Comparison of jet half-radii from present and past experiments.**

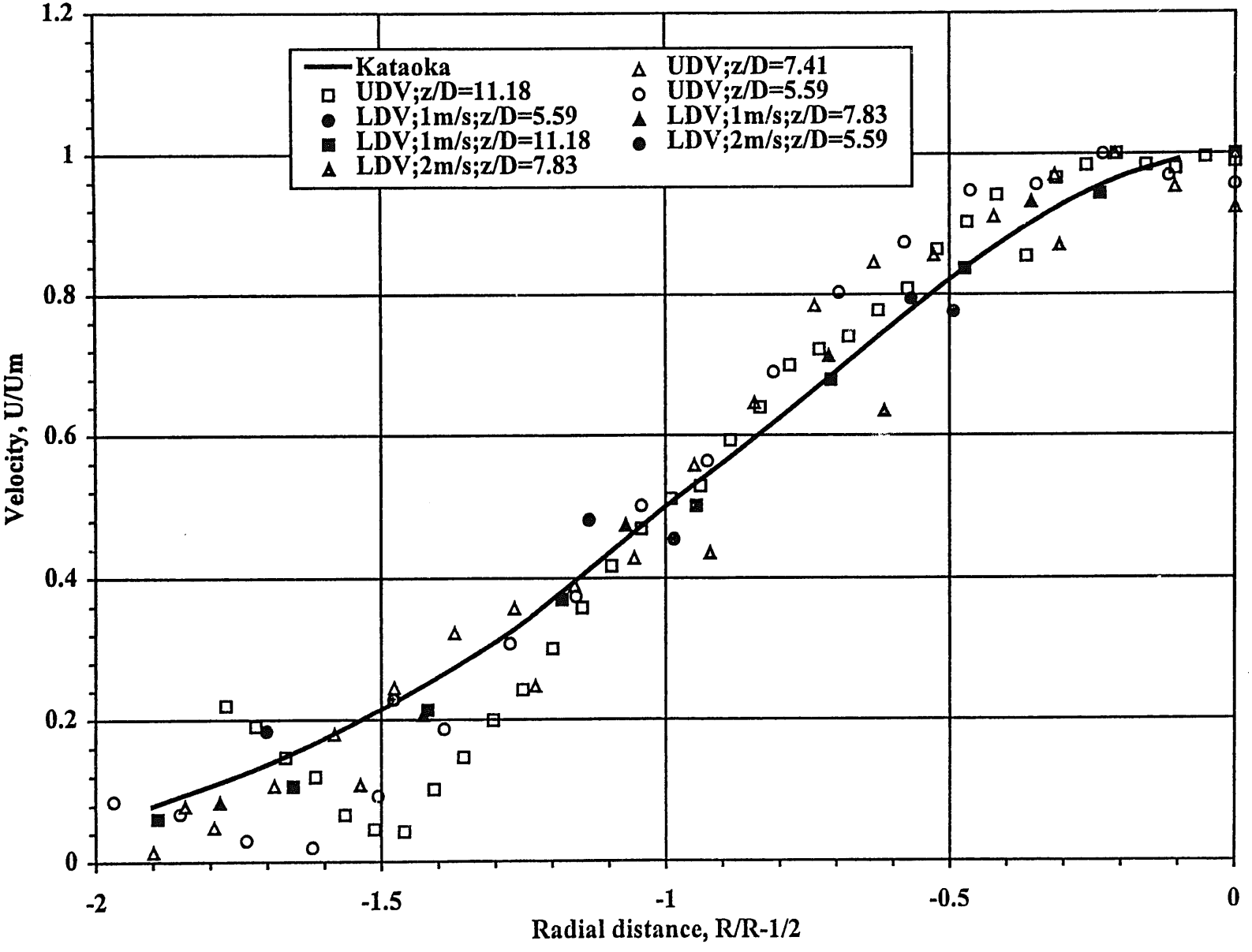

Figure 18. Radial velocity profile of a planar jet versus Kataoka's axisymmetric jet correlations.

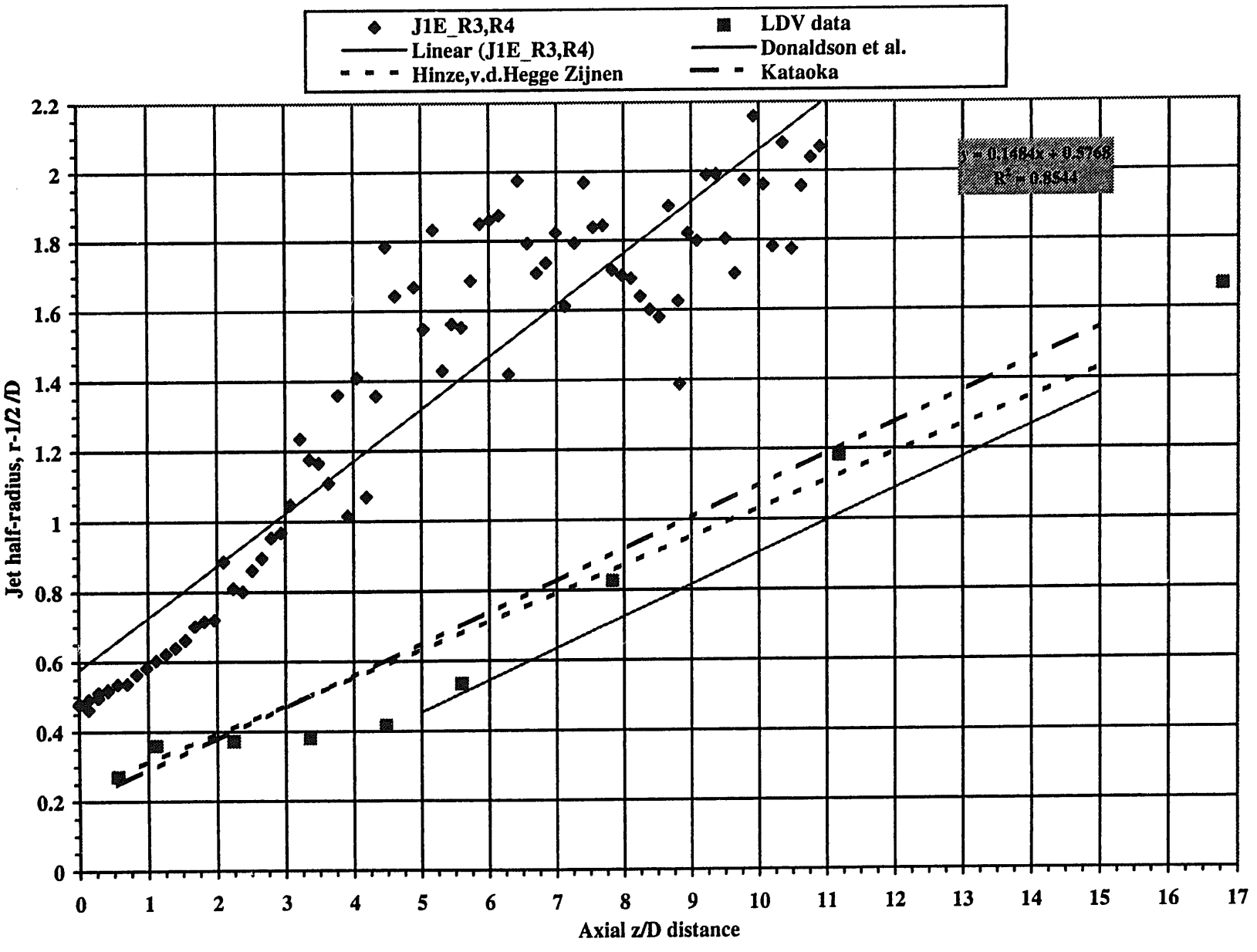

Figure 19. **Jet half-radius versus axial location, calculated from far-field UVP measurements.**

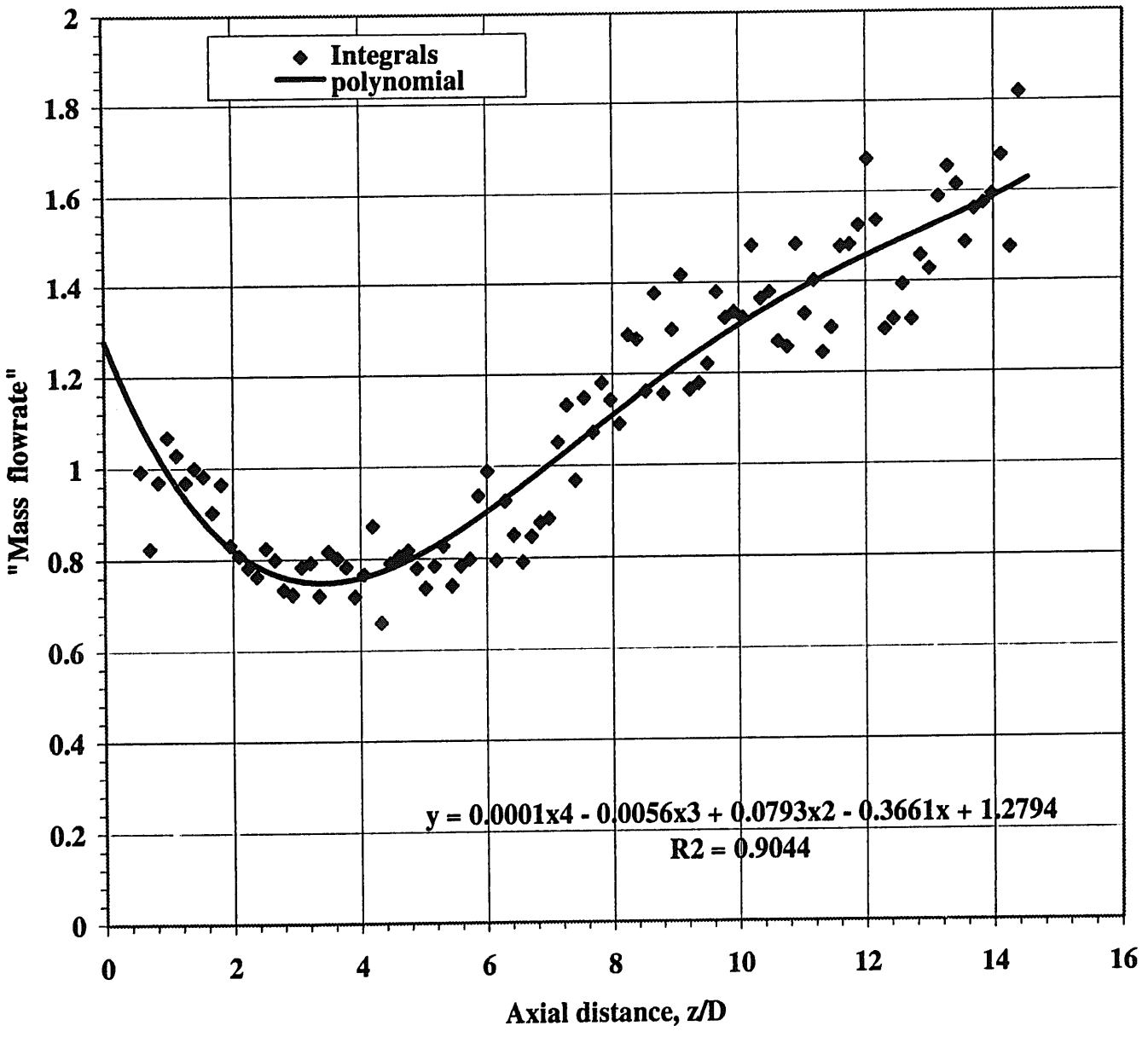

Figure 20(a). **Axial development of estimated "mass-flux" of single-jet.**

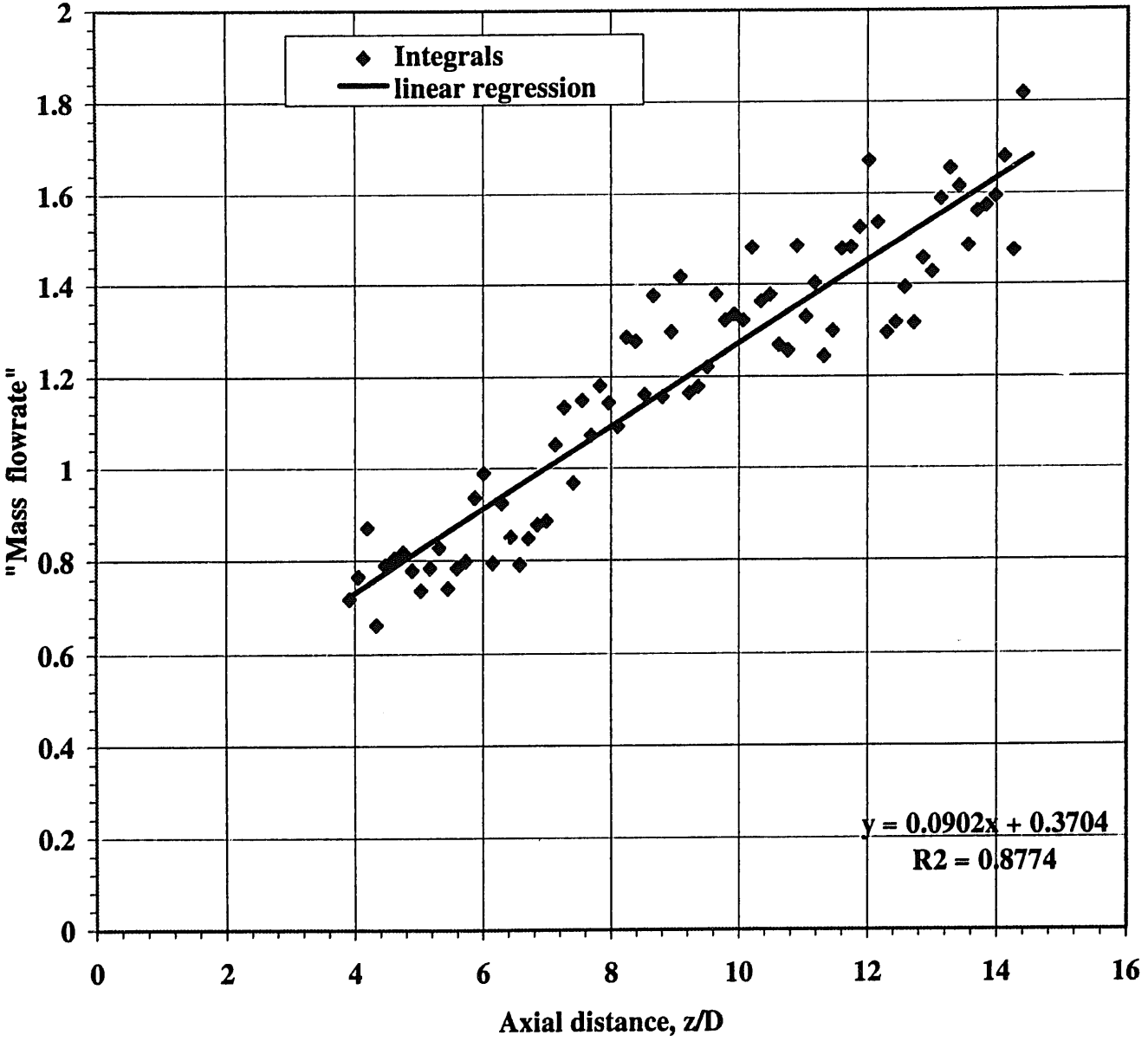

Figure 20(b). **Axial development of the estimated "mass-flux" beyond the core-length.**

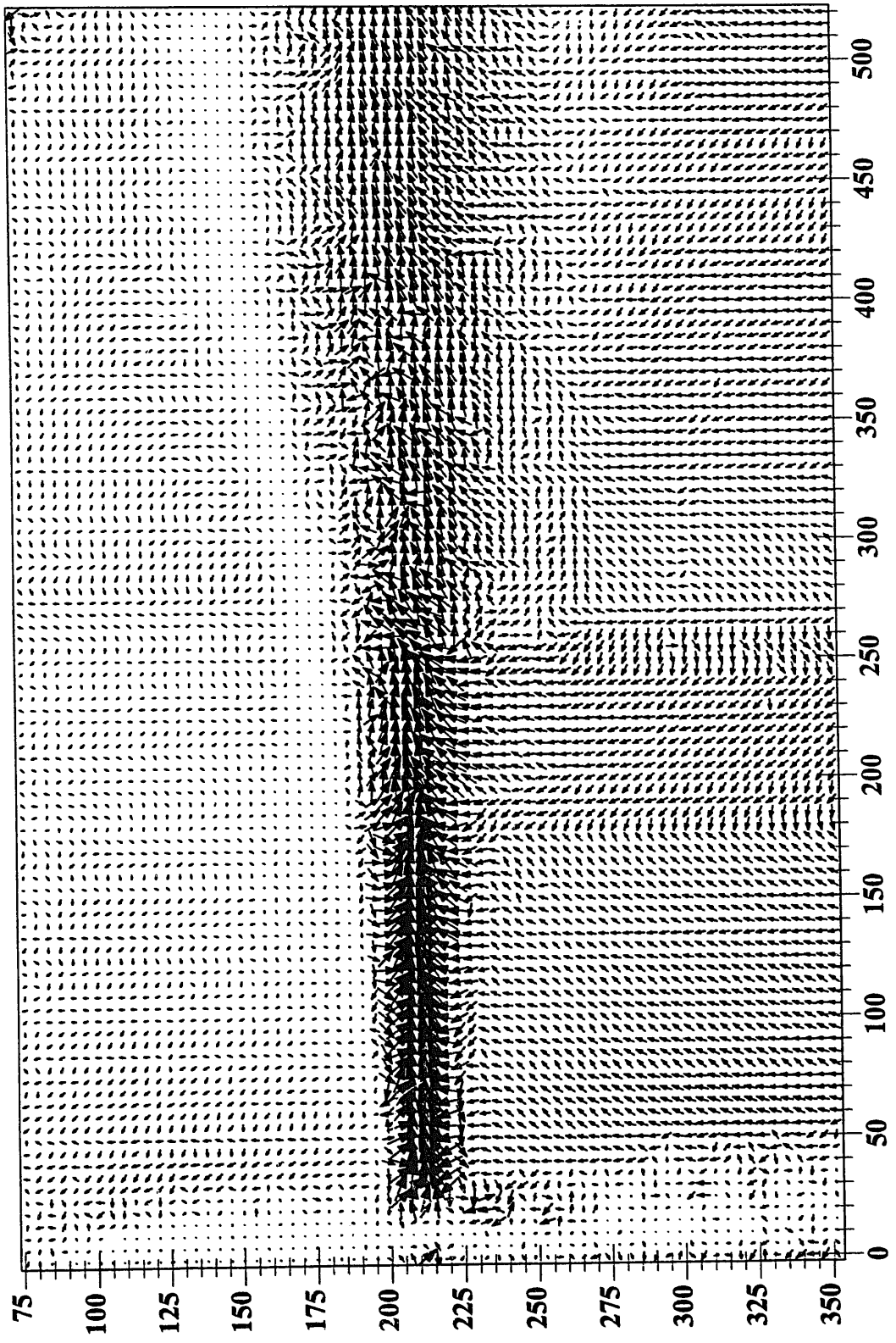
X-axis, spanwise
75
100
125
150
175
200
225
250
275
300
325
350
Z-axis, axial
0
50
100
150
200
250
300
350
400
450
500
-= 301.760

Figure 21

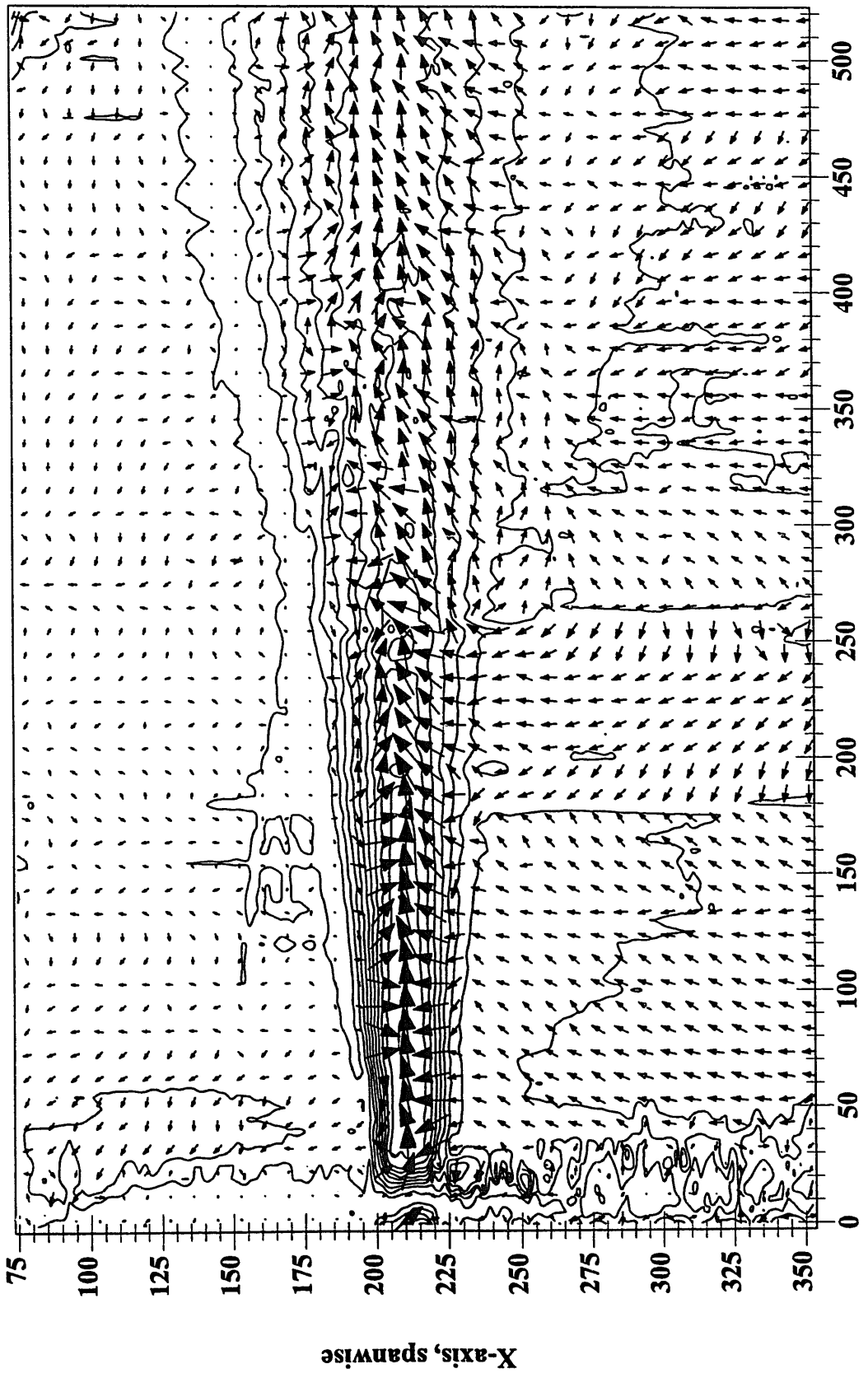
X-axis, spanwise
75
100
125
150
175
200
225
250
275
300
325
350
Z-axis, axial
0
50
100
150
200
250
300
350
400
450
500

Figure 22

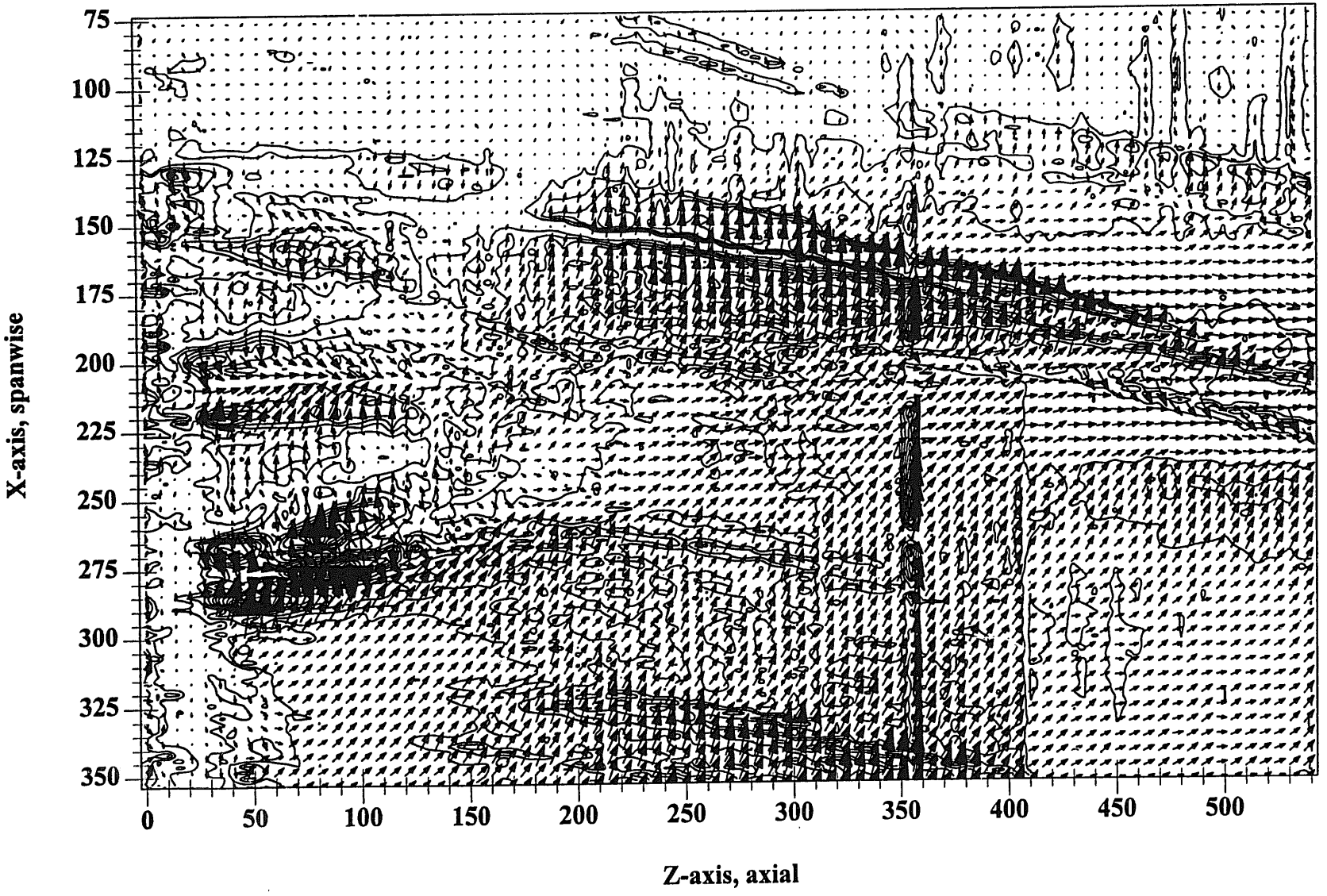
X-axis, spanwise
75
100
125
150
175
200
225
250
275
300
325
350
0
50
100
150
200
250
300
350
400
450
500
Z-axis, axial

Figure 23

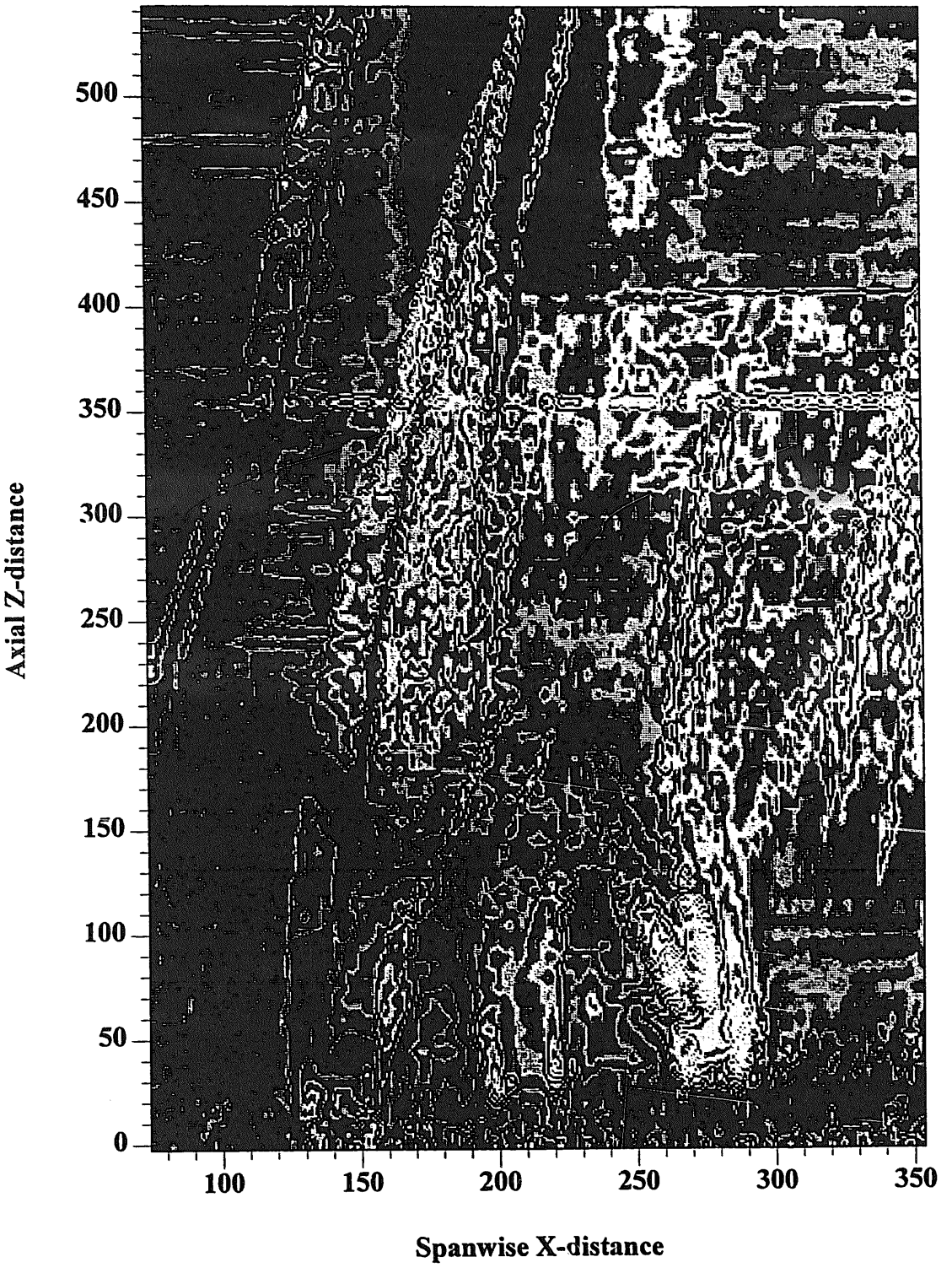
Axial Z-distance
500
450
400
350
300
250
200
150
100
50
0
100
150
200
250
300
350
Spanwise X-distance

Figure 24

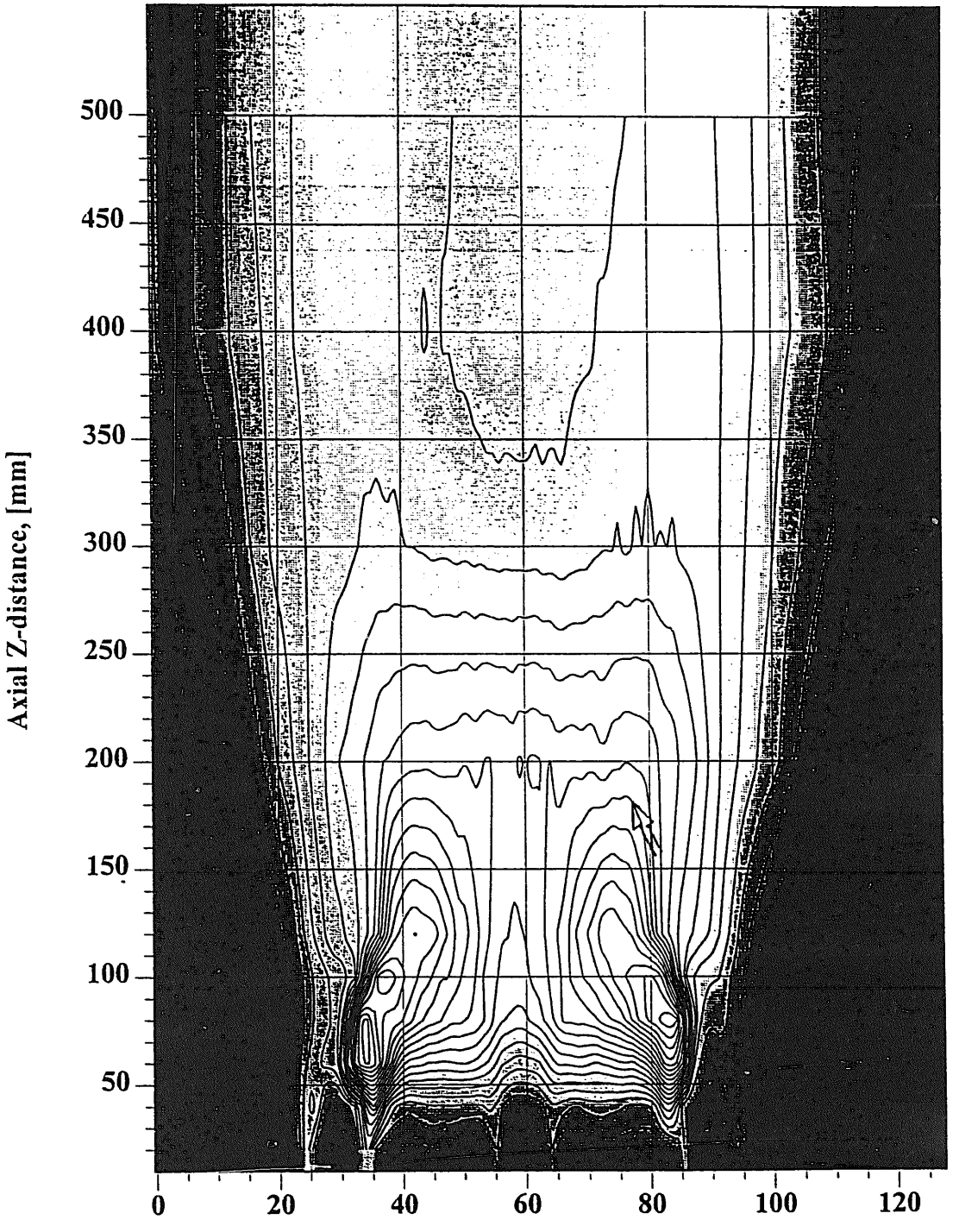

Figure 25(a). Standard deviation of velocity, of the transverse component, superimposed on isocontours of its magnitude with ΔT_{hc}=5°C.

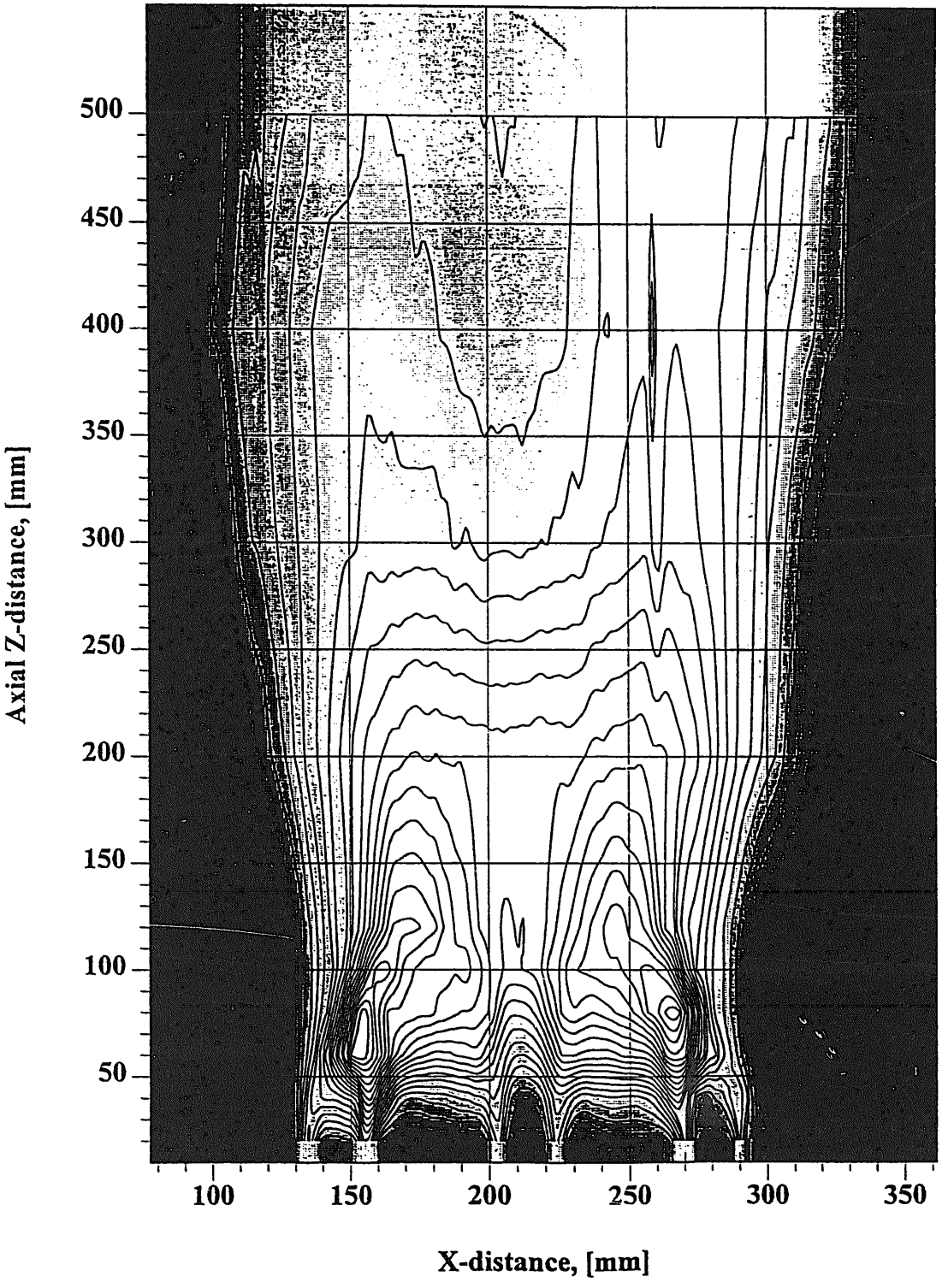

Figure 25(b). Standard deviation of velocity, of the transverse component, superimposed on isocontours of its magnitude with ΔT_{hc}=0°C.

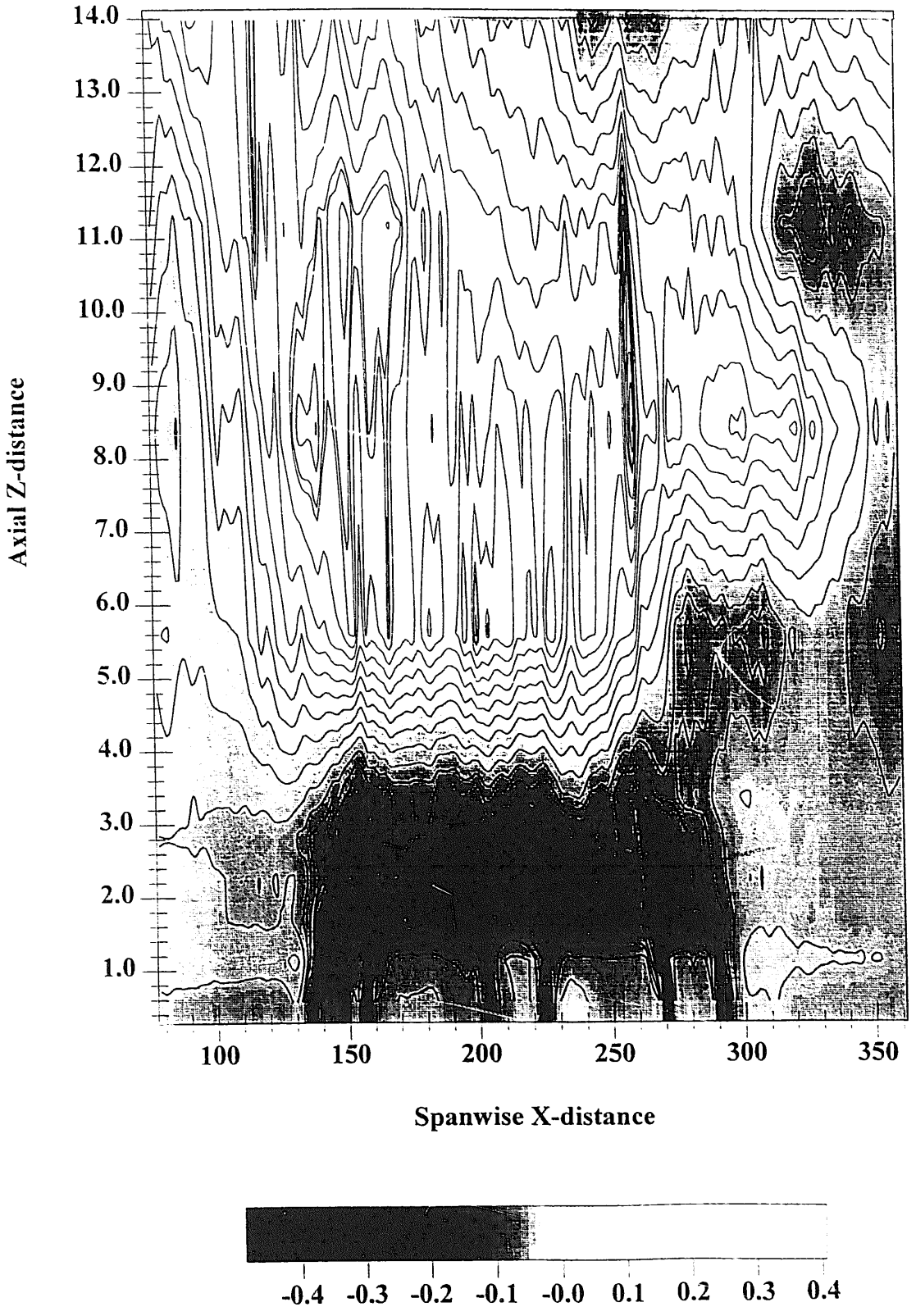

Figure 26. Difference in standard deviation of velocity, of the transverse component, superimposed on isocontours of its magnitude; [ΔT_{hc}=5°C - ΔT_{hc}=0°C]

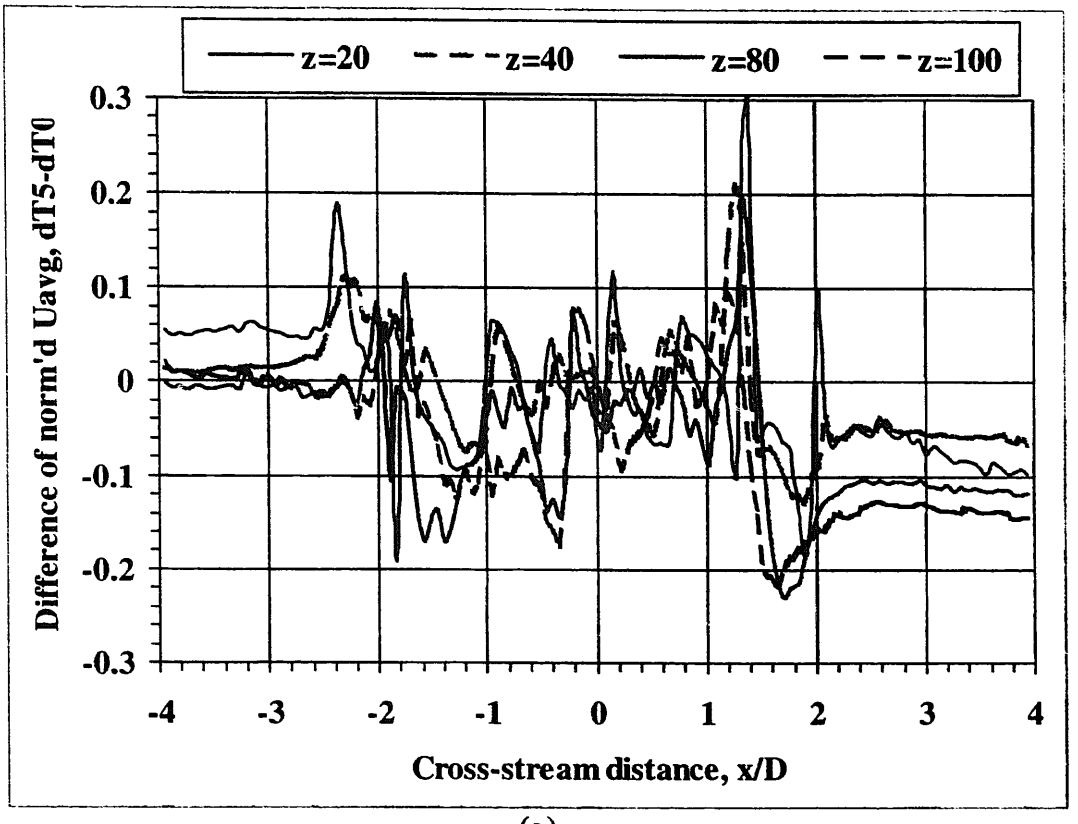

(a)

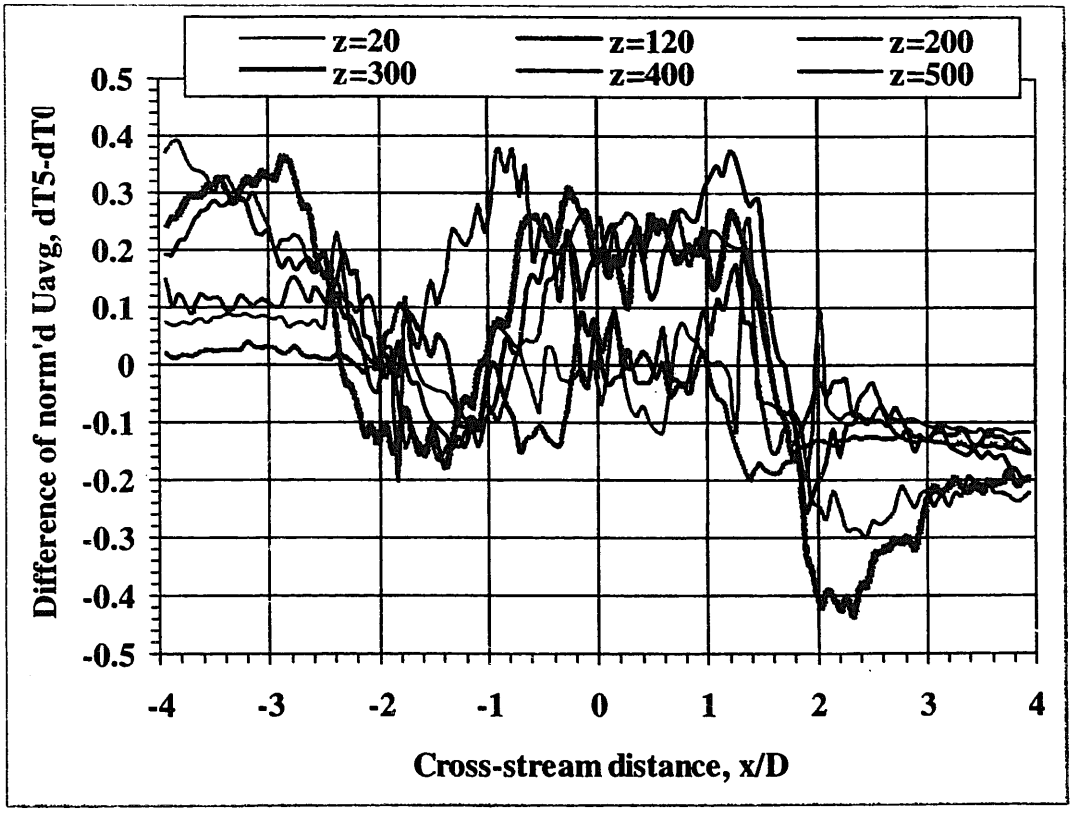

(b)

Figure 27(a) and (b).

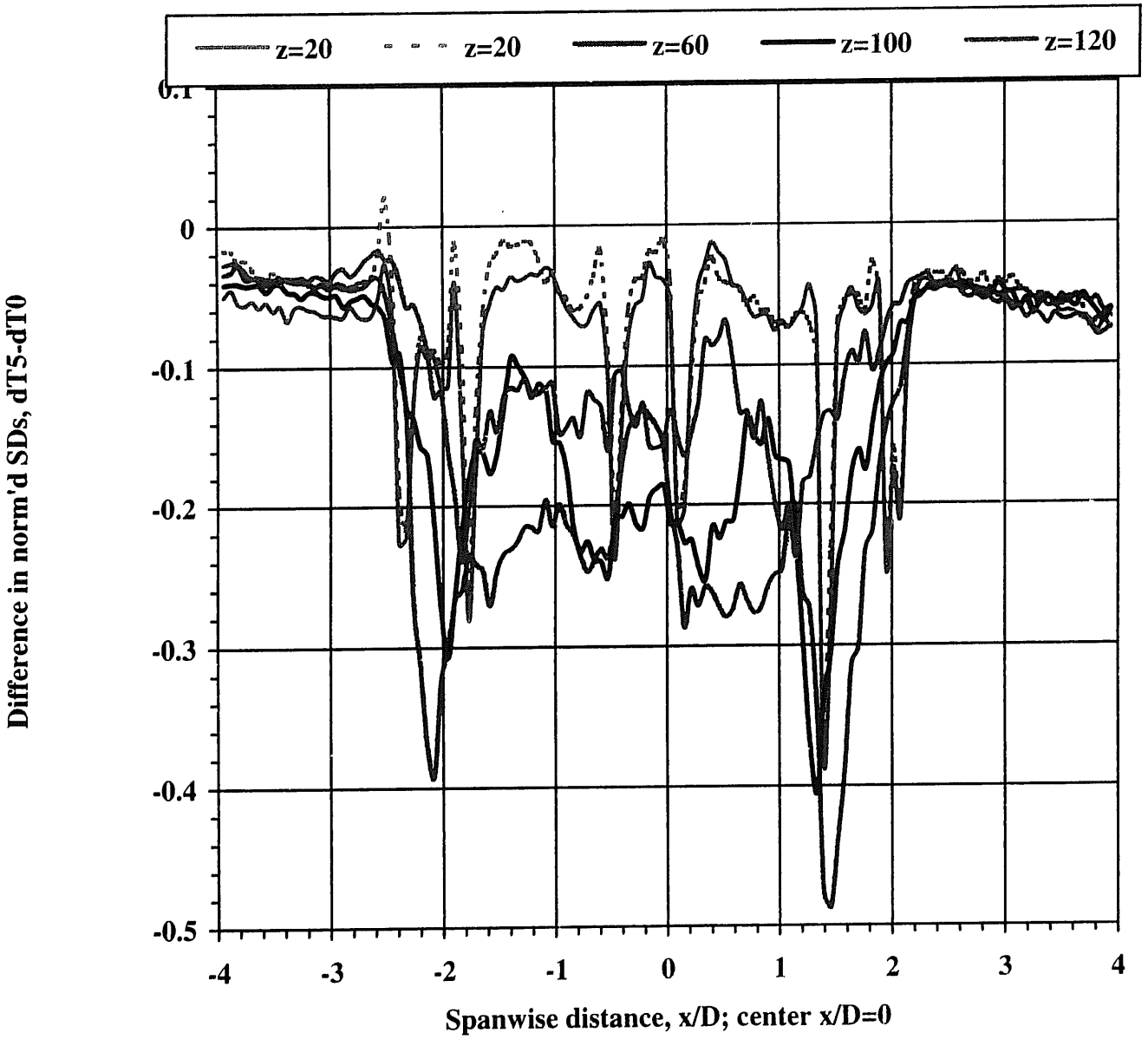

Figure 28(a). **Spanwise difference in normalized SD at various axial locations with and without jet-to-jet temperature difference (dT5-dT0).**

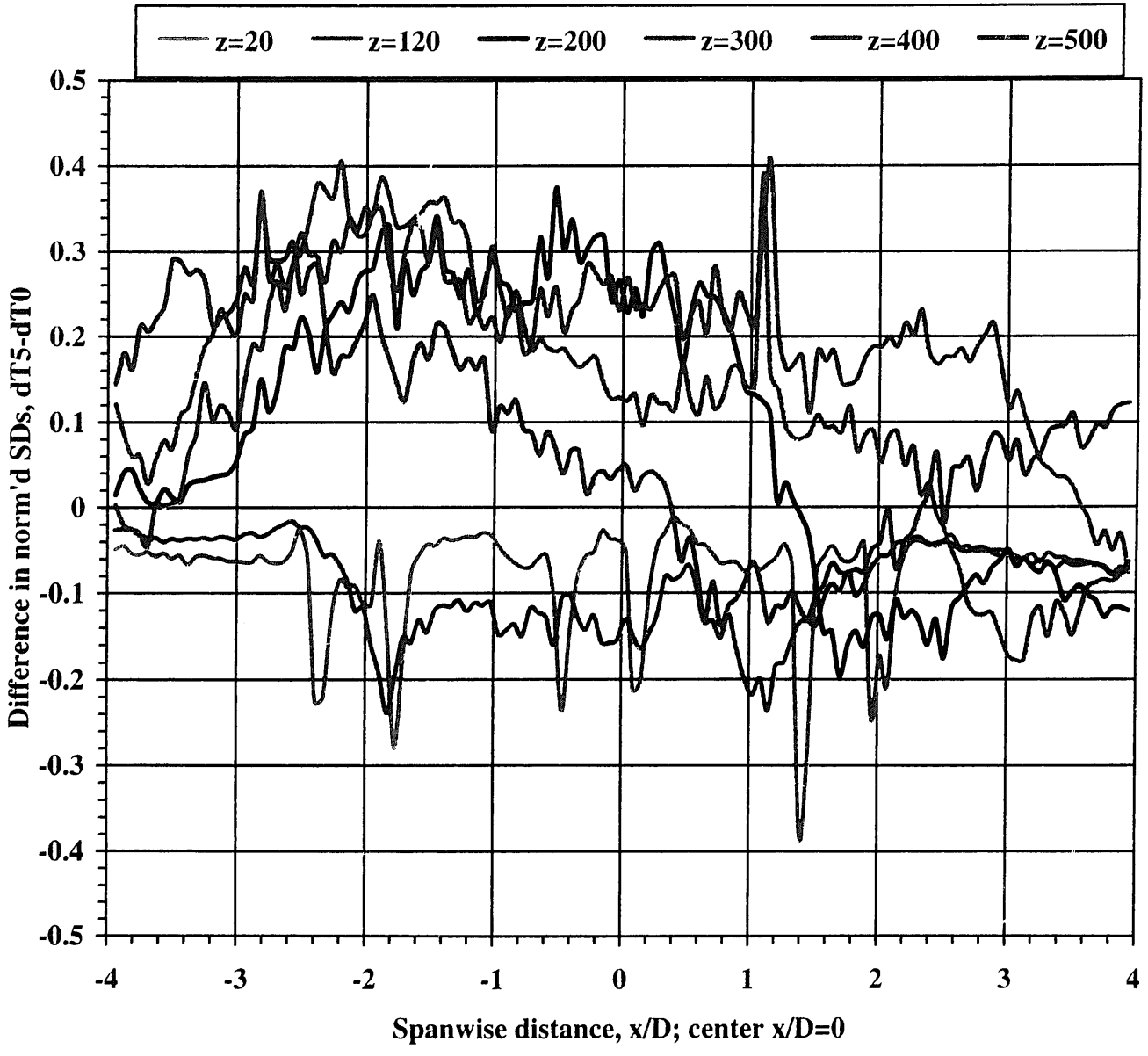

Figure 28(b). **Spanwise difference in normalized SD at various axial locations with and without jet-to-jet temperature difference (dT5-dT0).**

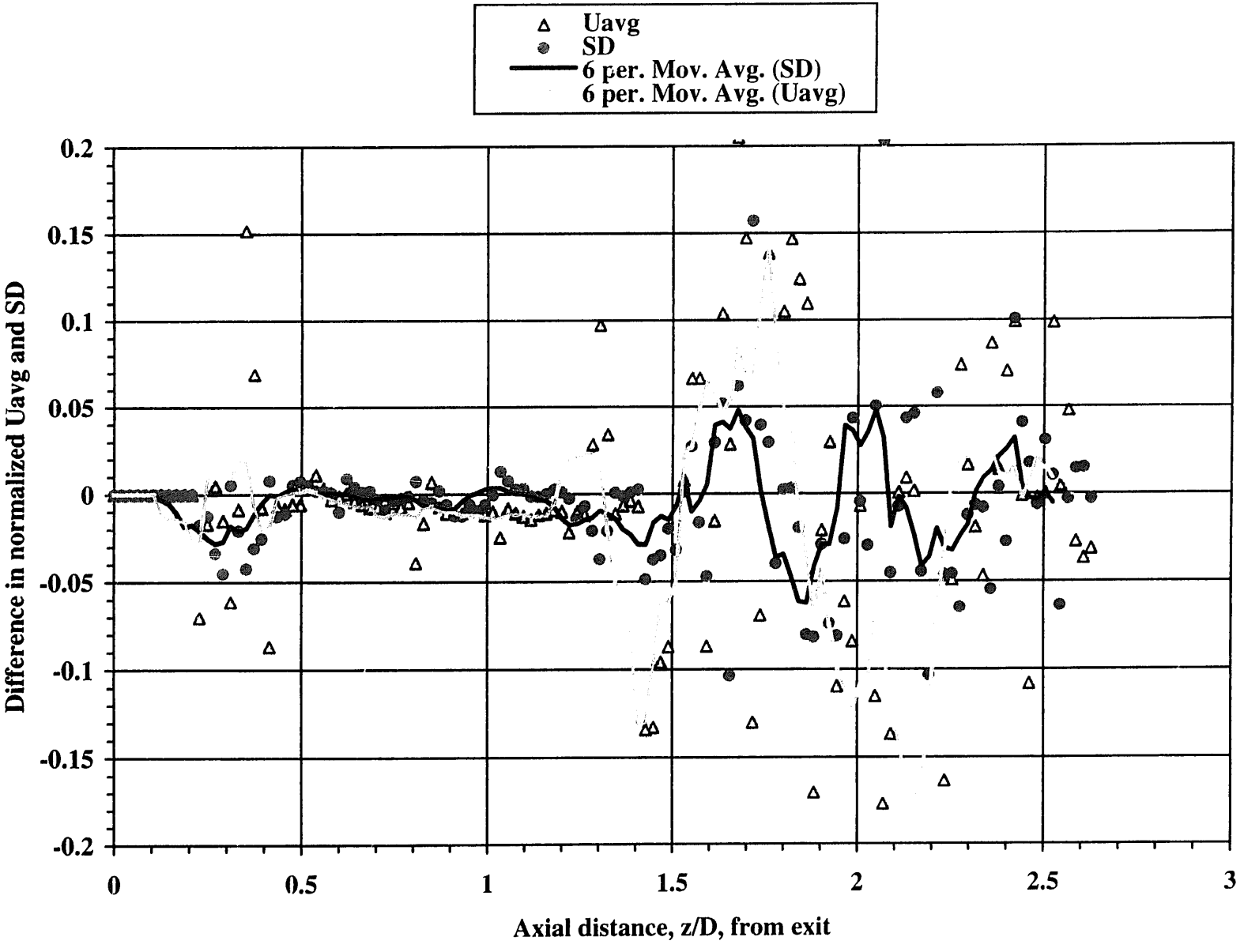

Figure 29. **Differences in normalized axial Uavg and SD of central jet in triple- and single-jet configurations.**

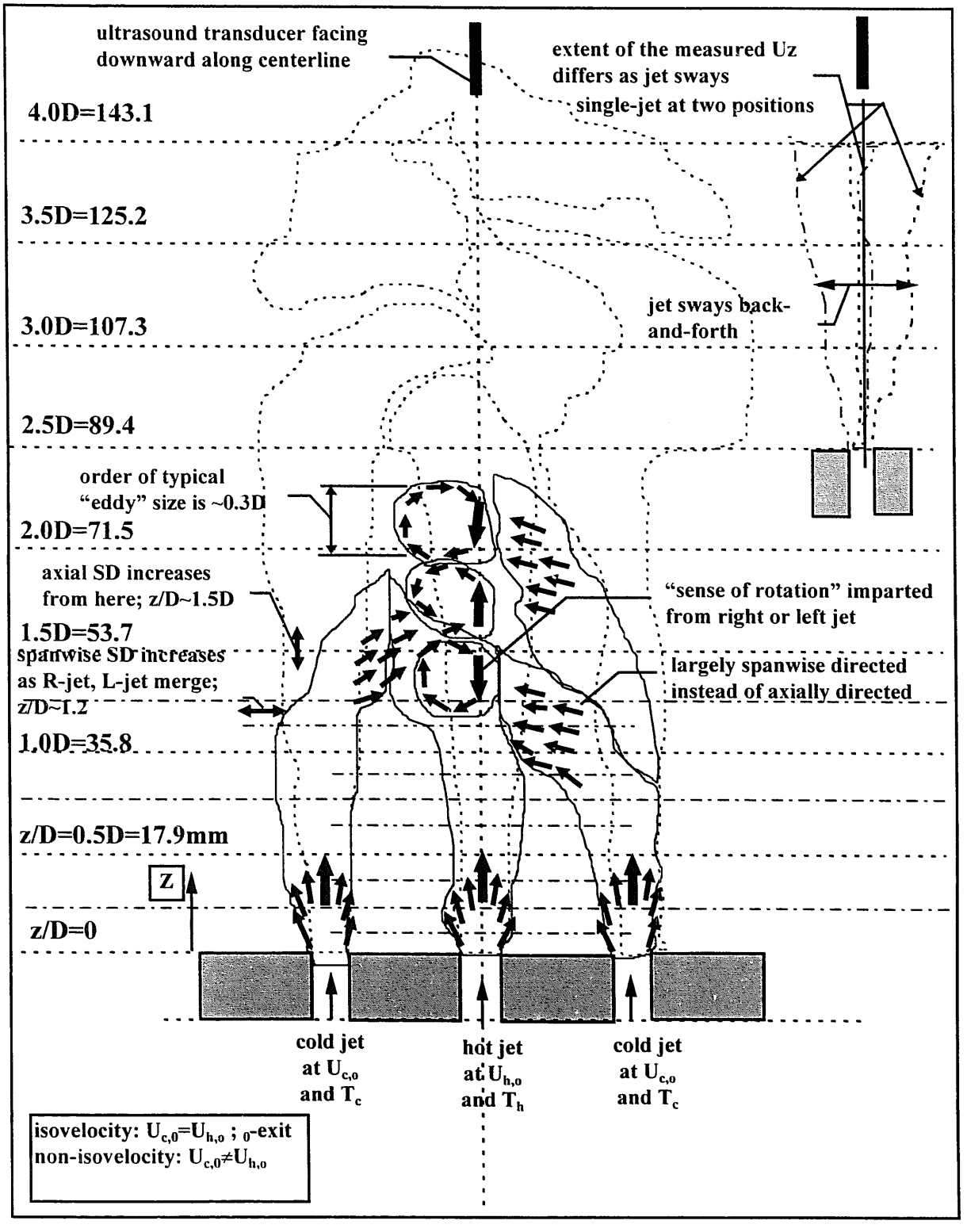

Figure 30. A schematic of the approximate flow development for the triple-jet with and without temperature difference.

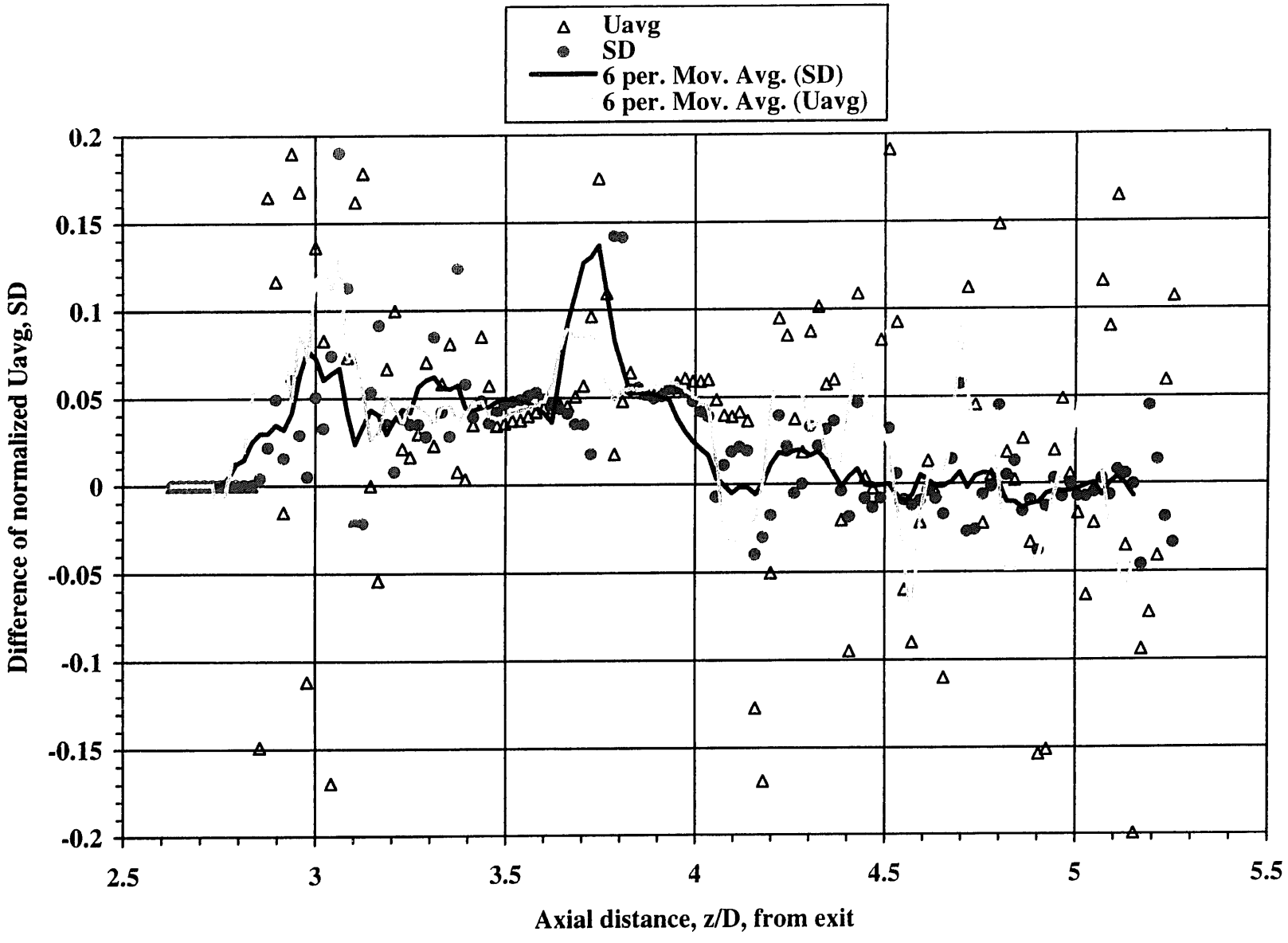

Figure 31. **Differences in axial Uavg and SD of central jet in triple- and single-jet configurations.**

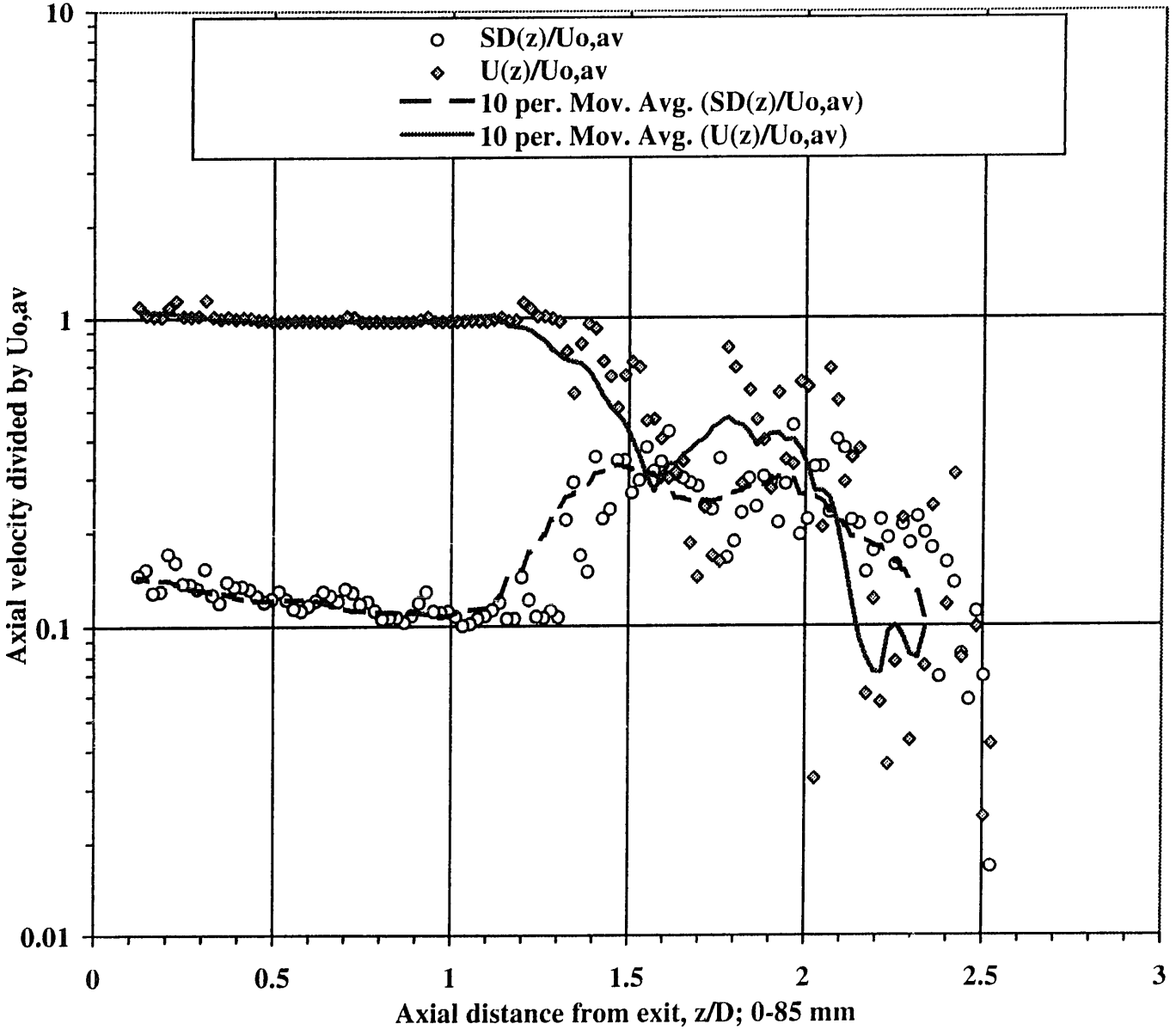

Figure 32. **Change in the axial average velocity and its deviation for x=0 to 85 mm from the exit.**

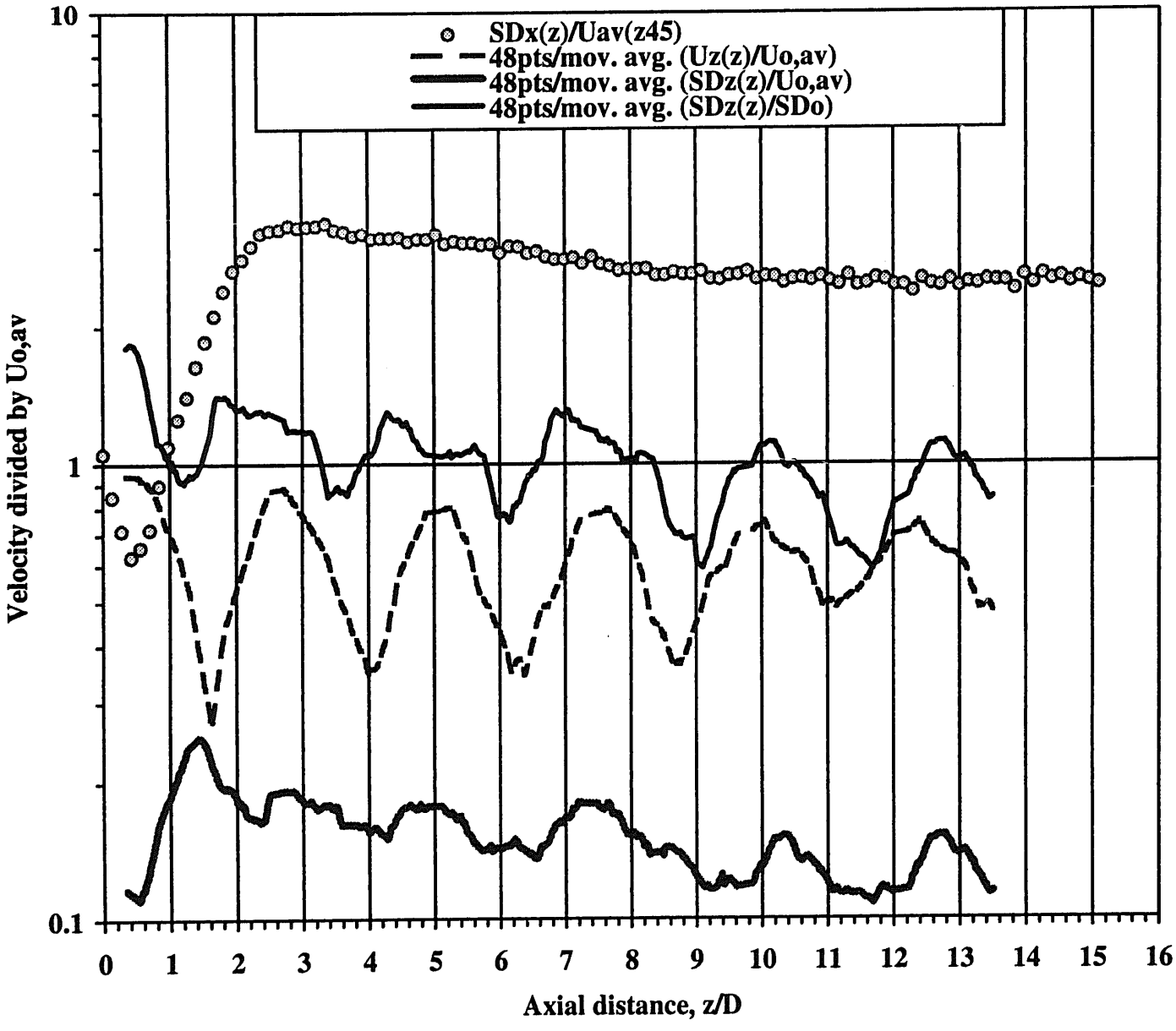

Figure 33. **Comparison of 20 pt average velocity and SD components against that measured from the side (left).**

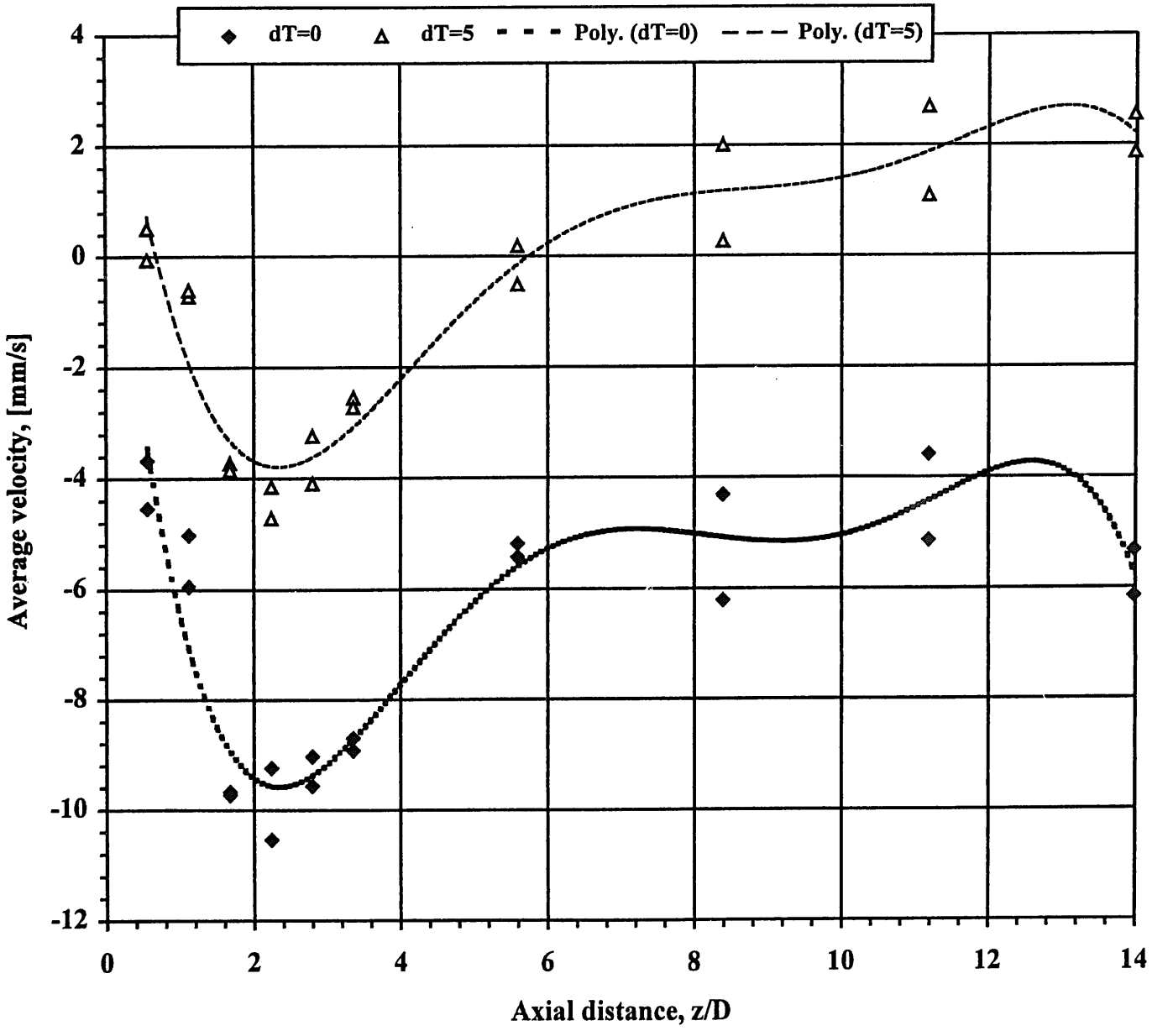

Figure 34. **Axial distribution of the average velocity with and without jet-to-jet temperature difference.**

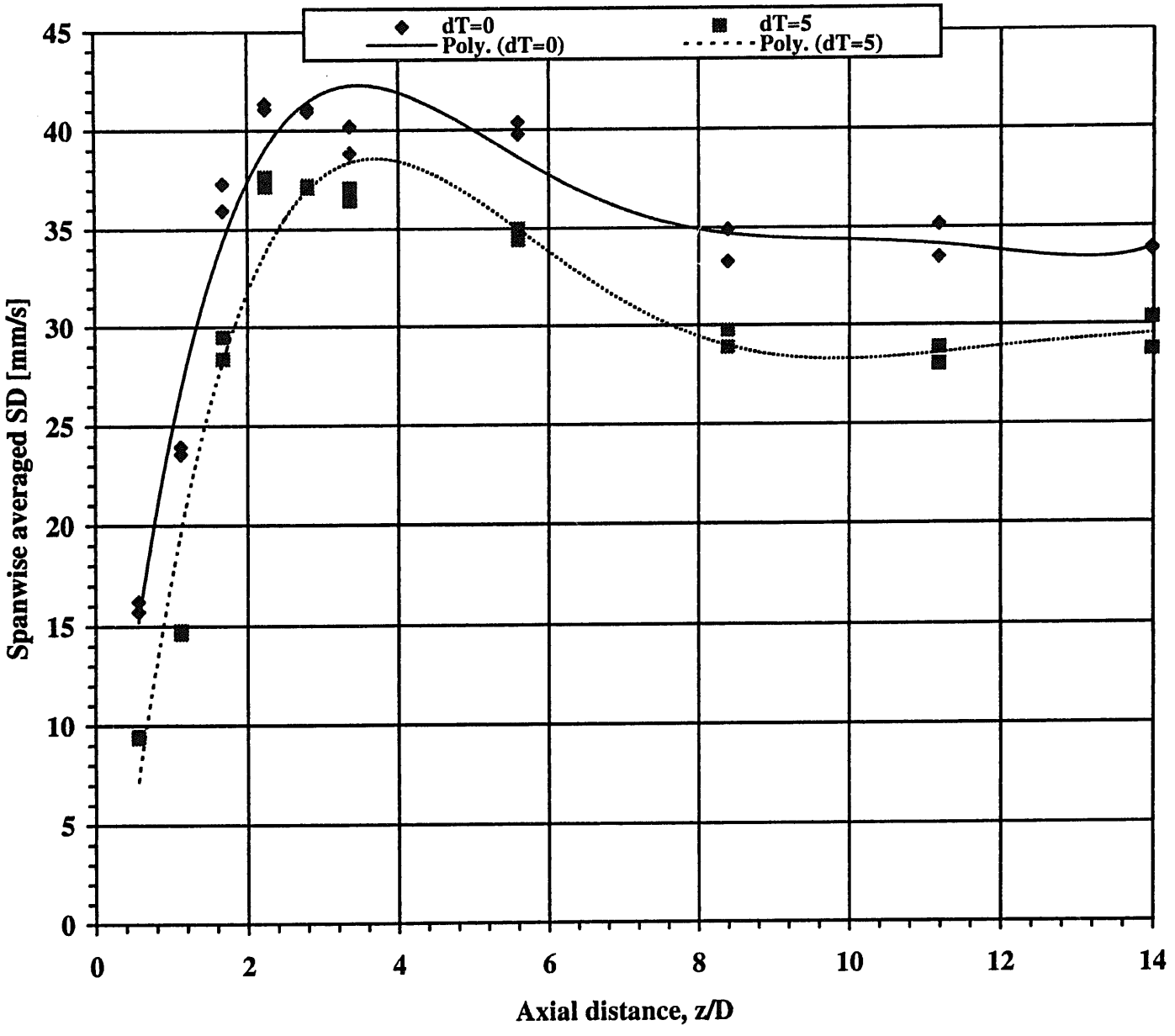

Figure 35. **Axial distribution of the average standard deviation (SD) with and without jet-to-jet temperature difference.**

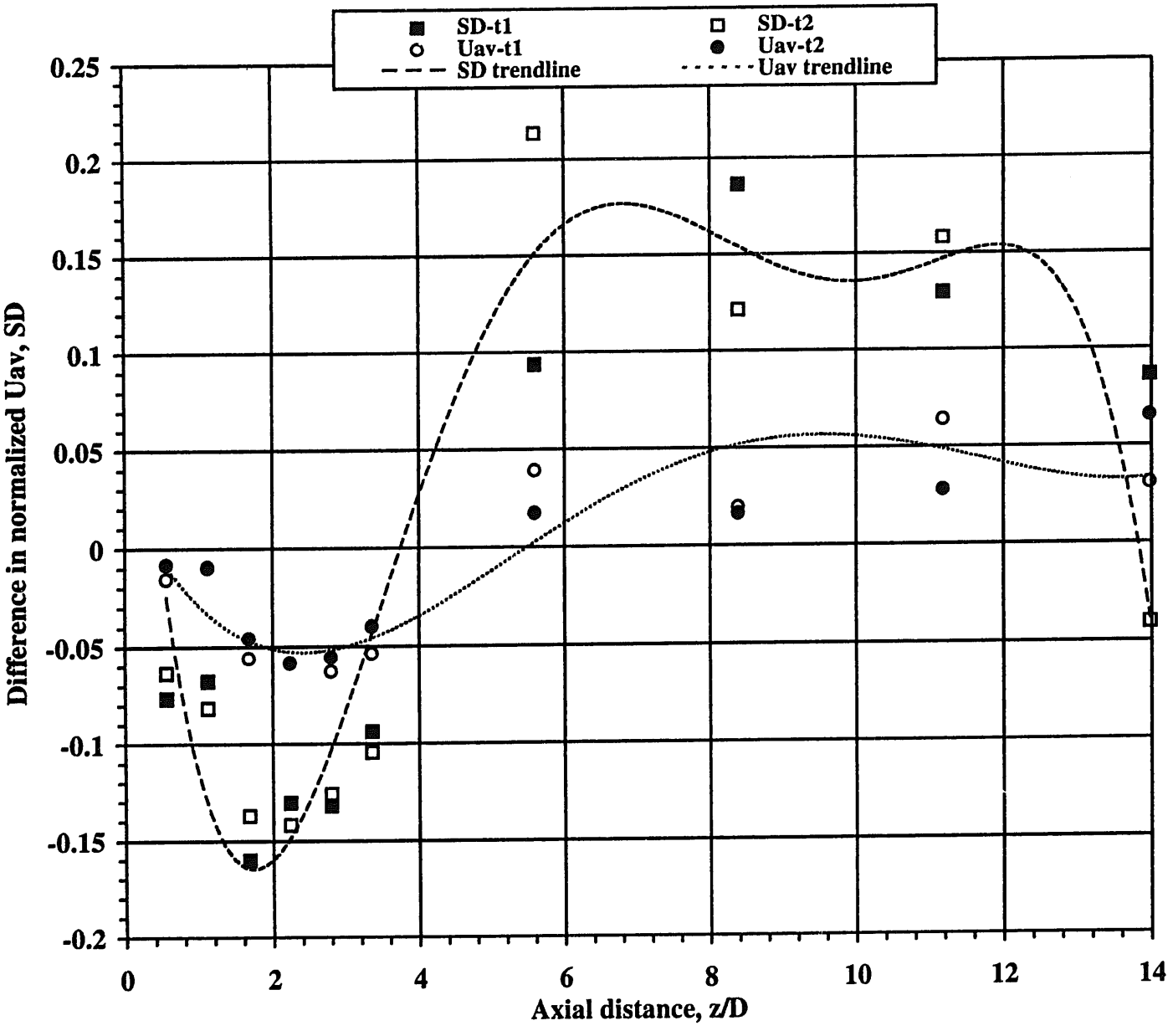

Figure 36. **Average differences in normalized Uavg and SD versus axial distance with and without jet-to-jet temperature difference.**

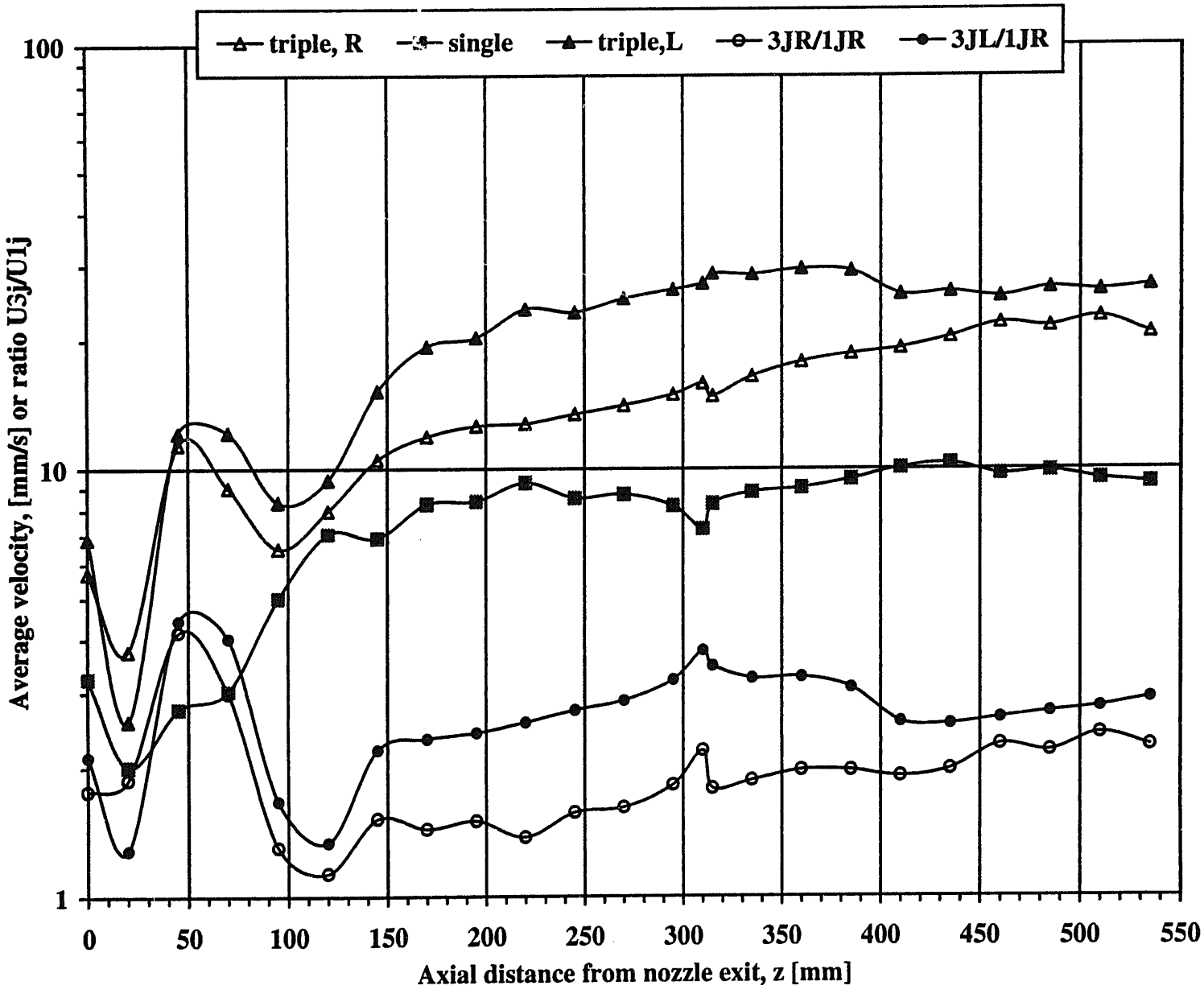

Figure 37. **Comparison of average velocity versus axial location for single- and triple-jets.**

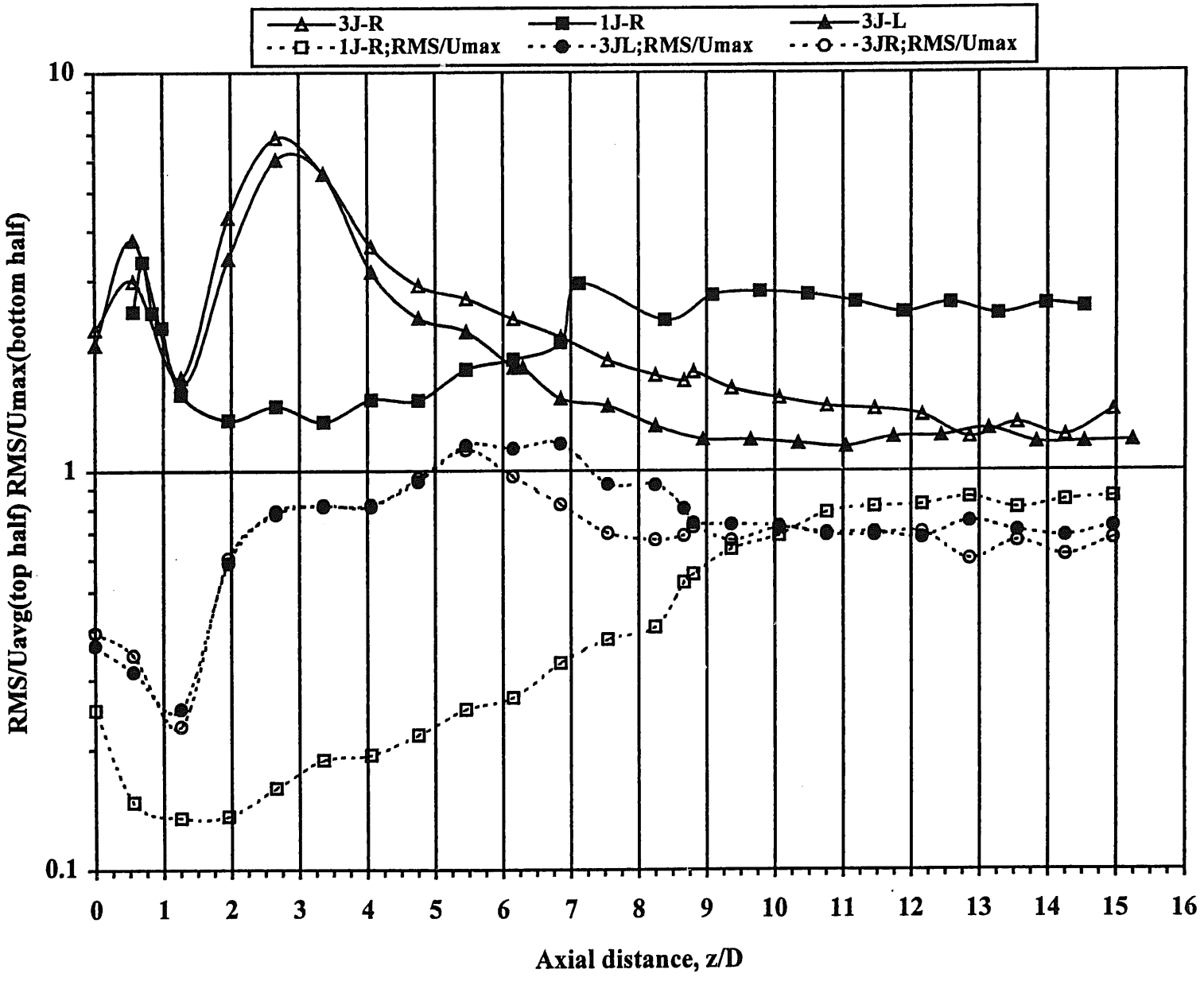

Figure 38. **Comparison of normalized RMS versus axial distance z/D for single- and triple-jets.**

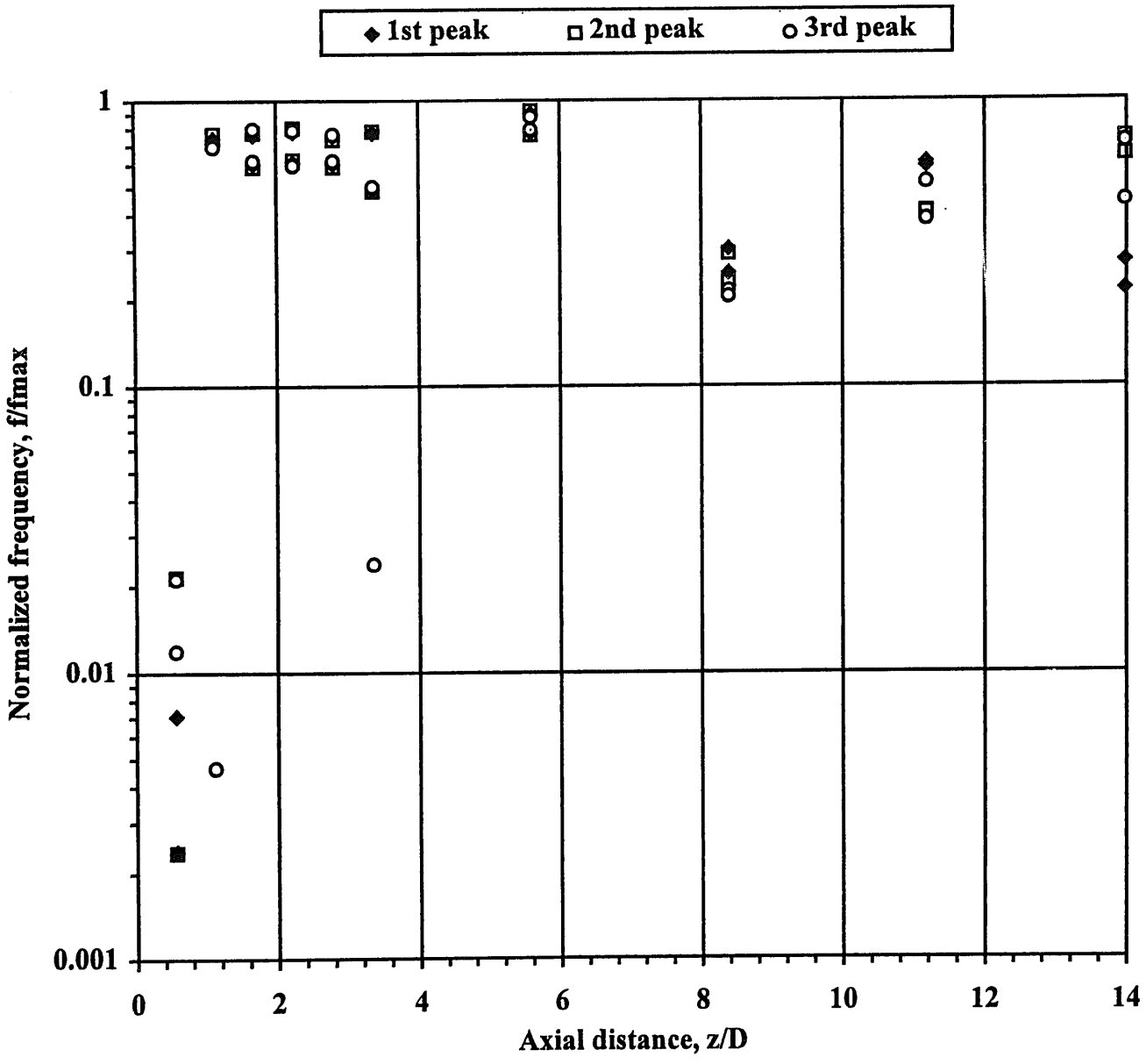

Figure 39. **Normalized frequency of spanwise velocity component versus axal distance for dT=0C.**

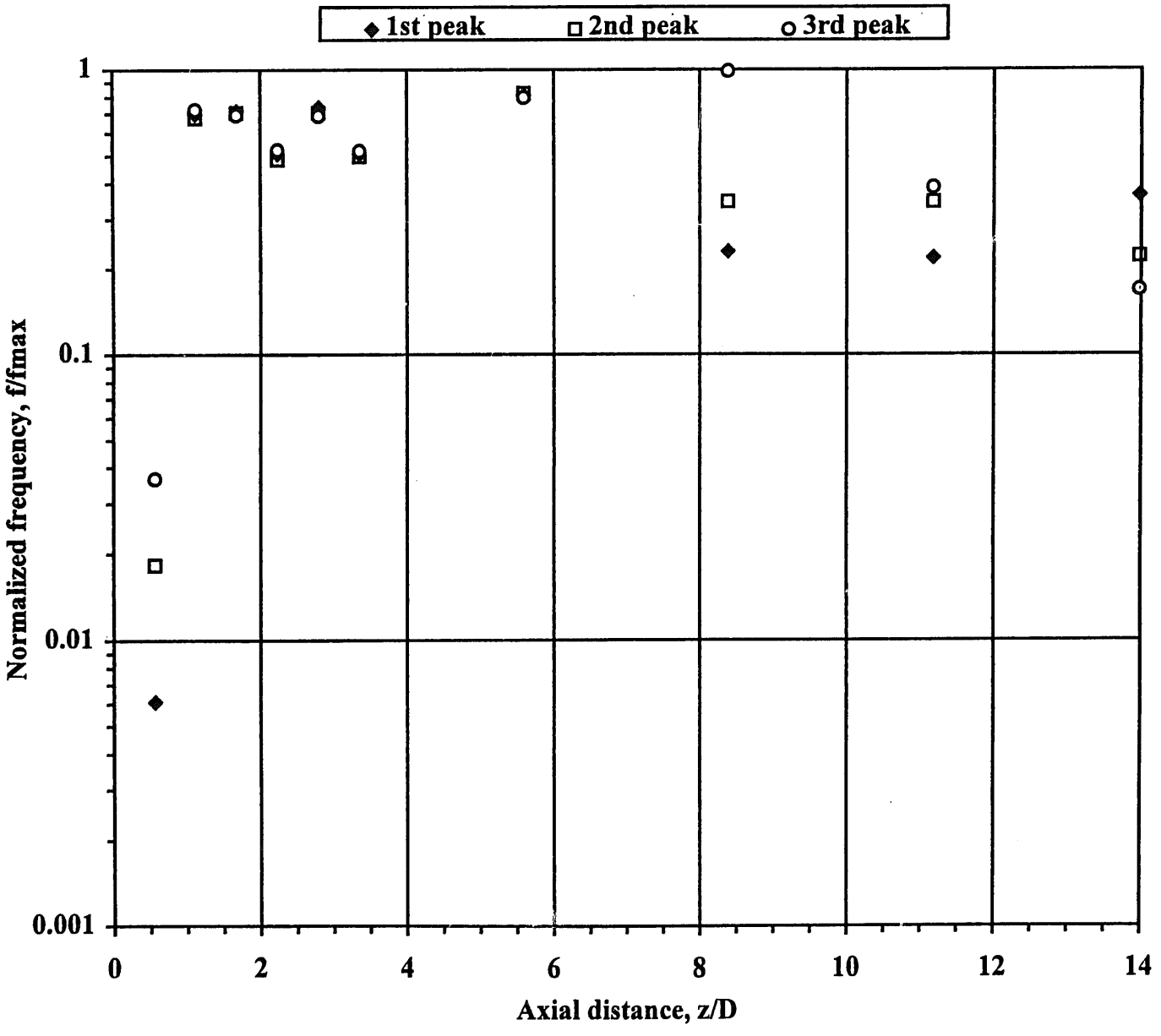

Figure 40. **Normalized frequency of spanwise velocity component versus axial distance for dT=5C.**

Appendix A

Ultrasound Doppler velocimetry principles and UVP operational parameters.

Ultrasound Doppler velocimetry

- **Principle works on ultrasound (acoustical) echography; time-of-flight measures position; Doppler shift enables calculation of velocity; sign of Doppler shift indicates direction of flow.**
- **Ultrasound transducer is pulsed; ultrasound is reflected from tracer-particles;tracer particles are added in to water; in sodium, *impurities* act as tracer-particles.**
- **Velocity profile constructed along 128 points; magnitude and sign.**
- ***Spatio-temporal* velocity data is recorded**

Device used; Met-flow SA; two models; UVP X-1 single TDX; X-3 up to 60 TDXs with multiplexor can be used for 2D and 3D measurements

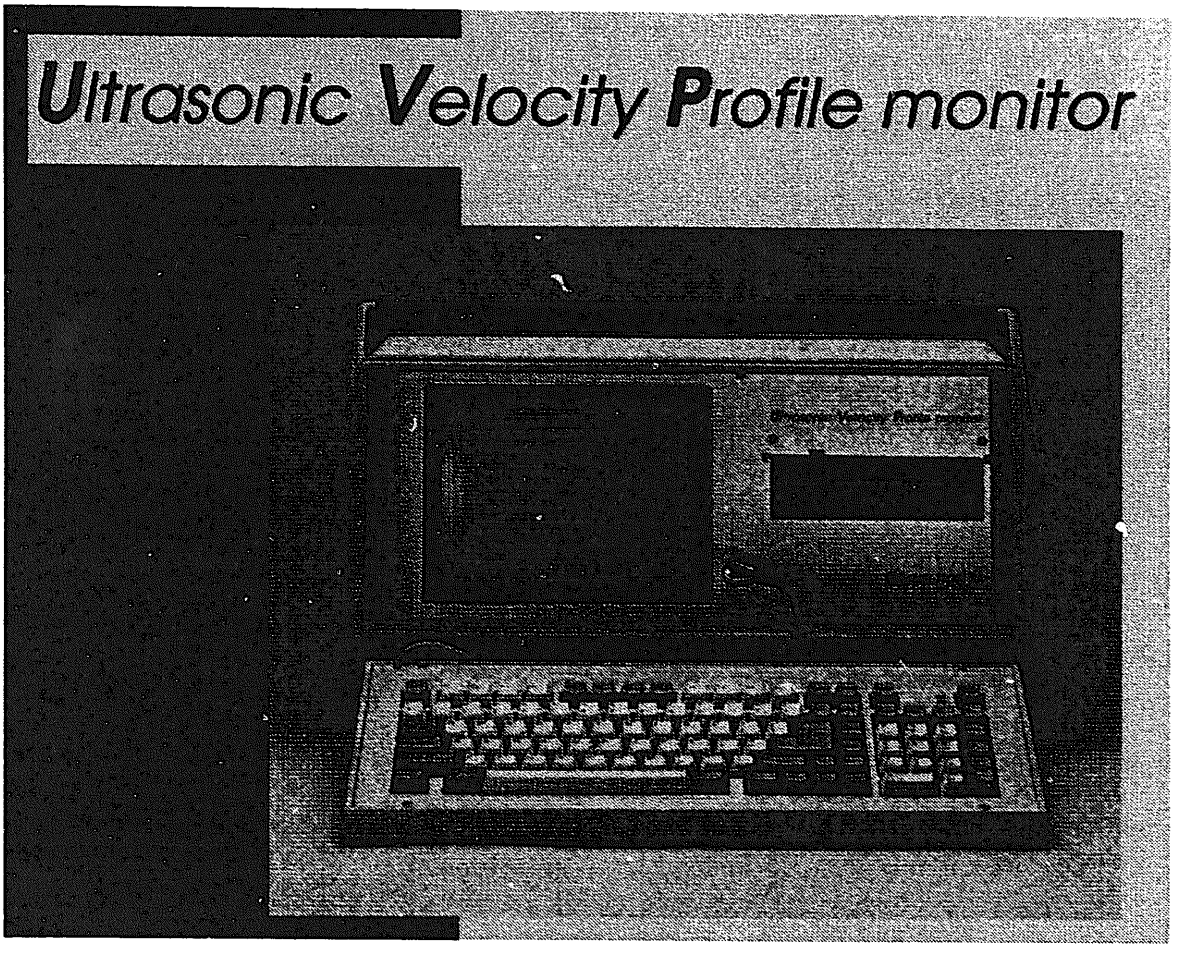

Figure A-1. ***Picture of Met-flow's UVP Model X-1***

The principle of operation of the UVP is explained with the aid of Fig. A-2 which shows flow in a horizontal pipe. An ultrasonic (US) signal is emitted through the excitation of a piezoelectric transducer element along a measuring line (ML). This burst wave, less some reflections from the walls (front and rear), propagates through the fluid (with time τ) where particles added to the fluid reflect these waves. These reflected waves (echoes) are then received by the same transducer and contain all the spatial and velocity information of the suspended particles moving with the flow. More specifically, the position of a suspended particle is calculated from the time-delay between the burst and reception signal and the velocity is determined from the Doppler-shift frequency at that instant. The sign of the Doppler-shift detects flow coming toward or away from the transducer. This enables one to produce the componental (*Vx*) velocity profile along the line of measurement. While additional details are contained in texts such as Krautkrämer [*cf:* J. Krautkrämer and H. Krautkrämer, Ultrasonic Testing of Materials, 4th ed., Springer-Verlag, Berlin, 1990] with its original emphasis on non-destructive testing of materials, this method has been adapted for velocity measurements in liquids. In particular, the UVP used here contains hardware/software development by Takeda [*cf:* Y. Takeda, Int. J. Heat Fluid Flow, 7, 1986, 313] in conjunction with Met-Flow SA. The device has been thoroughly tested in a number of experiments and liquids [*cf (example):* Y. Takeda, Nucl. Technol., 79, 1987,120] One representative velocity profile out of 1024 recorded per measurement run is shown in Fig. A-3 (of natural convection flow) .

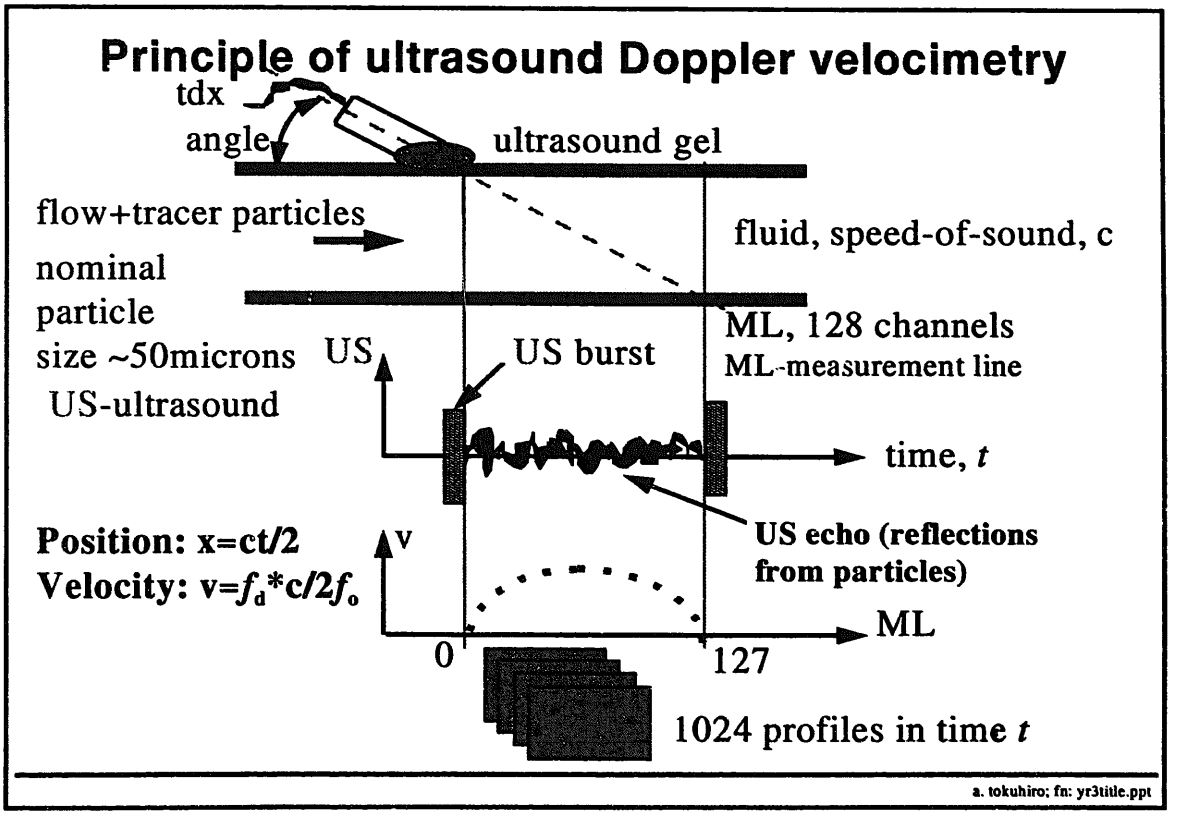

Figure A-2. Principle of ultrasound Doppler velocimetry.

Deciphering the UVP velocity profile

Figure A-3 shows a representative average velocity profile of the jet at z=0.045 m (x/D=1.258) from the exit. As mentioned the profile shows the velocity component at 10° to the horizontal; that is, nearly the spanwise (transverse) component. The measurement span corresponds to 0.284 m, with the centerline taken as the origin (x/D=0). The actual measured profile is the inverted image of the figure below since with respect to the transducer, flows coming toward it are "-" (negative) and those flowing away are "+" if one considers the sign of the Doppler shift. The inverted representation however, does not change the information content of the profile. We thus see that a prominent feature is the peaked, jet-like profile in the center. To the sides of the center are the entrained-flow regions, of approximately equal magnitude and *on-average* of opposite sign with respect to the transducer. We say *on-average* here because the mixing layer-induced entrained flow, to the right and left of the jet, does not flow uni-directionally, but fluctuates in magnitude and direction during the measurement period. Also displayed are the two peaks of the standard deviation distribution characterizing respectively, the edge and core of the jet.

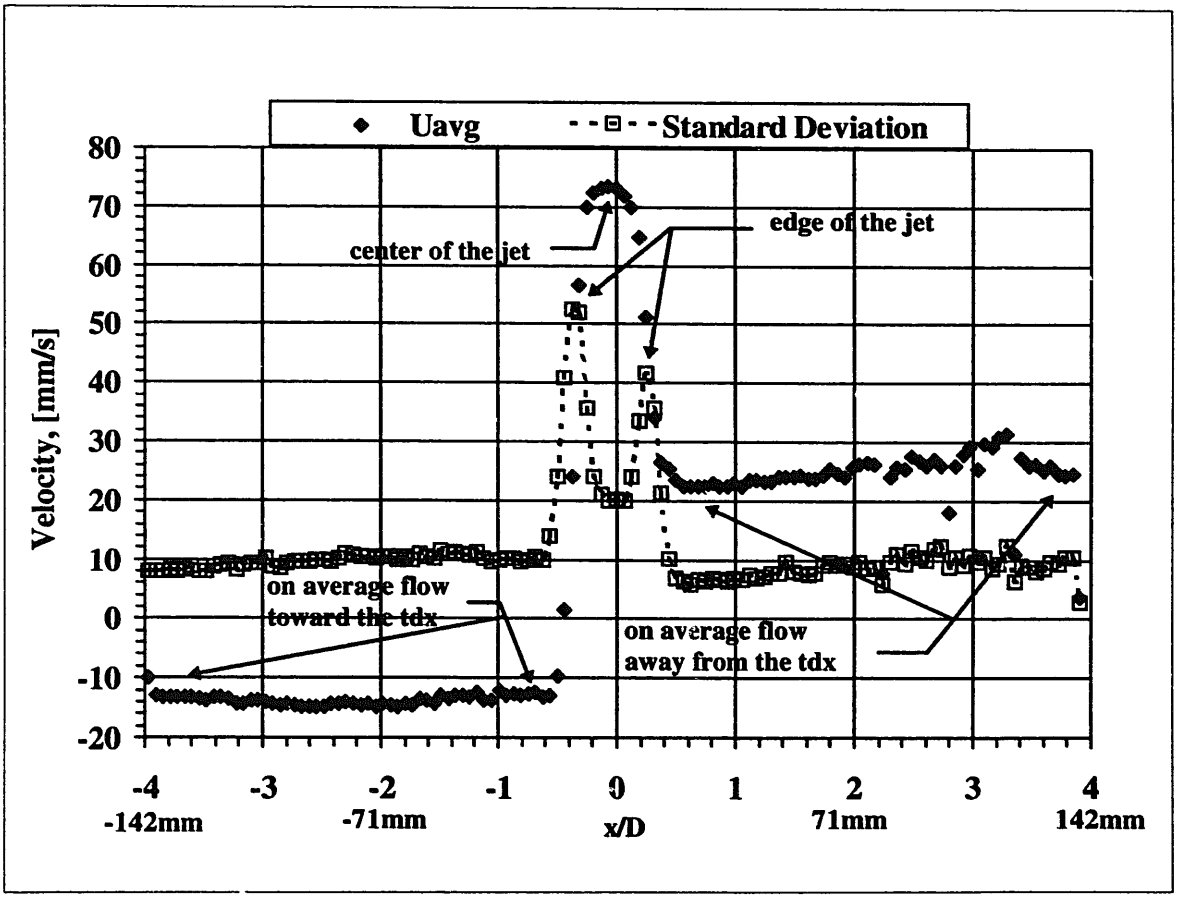

Figure A-3. Representative average velocity profile of the jet at z=0.045 m (z/D=1.258).

Table A-1. UVP operational parameters.

Typical set of UVP operational parameters used in this experiment. An explanation of each parameter is given in the UVP Model X-1 User's Manual.

mf: Reviewing Profiles from UVP		
File: auto.020		
UVP Parameters		
1) *Channel Distance:*	**2.22 (mm)**	
2) *Starting channel:*	**76.00 (mm)**	
3) *Ending channel:*	**360.00 (mm)**	
4) *Fprf:*	**1953 (Hz)**	
5) *Sound Velocity:*	**1480 (m/s)**	
6) *Storing interval:*	**0**	
7) *Trigger mode:*	**1**	
8) *Auto record mode:*	**1**	**Doppler Coef.: 7.63**
9) *Emission voltage:*	**160 (V)**	**Speed Coef.: 0.19**
10) *RF Gain Factor:*	**2**	**Velocity Conv. 1.41**
11) *Screen scale factor:*	**1**	
12) *Is this file OK? (Y/N)*		
MET-FLOW S.A. Lausanne Switzerland		

1) ***Channel Distance:*** describes the distance per channel; depends on the measured reange; there are 128 total channels; increments as follows in [mm]: 0.74, 1.48, 2.22, 3.70, 5.18 .

2) ***Starting channel:*** describes distance from the head of the transducer to the first channel or where the measurement should begin; used for example to eliminate the wall thickness in pipe-flow; 5 [mm] +n*12 [mm] where n=1,2,3...

3) ***Ending channel:*** describes the distance of the end channel; maximum of 75 cm with Model X-1; maximum depths are as follows [mm]: 91, 189, 378, 758.

4) ***Fprf:*** pulse repetition frequency; due to the Nyquist sampling theorem related to Fprf, the maximum detectable Doppler shift is limited. This limits the maximum measurable velocity, Vmax, and distance, Pmax, as follows: $V_{max}=cF_{prf}/4f$ and $P_{max}=c/2F_{prf}$. Here c and f are the acoustic velocity in the medium and the frequency of ultrasound emission (here 4MHz).

5) ***Sound Velocity:*** describes the acoustic velocity in the liquid medium, at a given temperature; equivalent to defining the test medium; 1480 [m/s] at 20°C; range from 1000<c<3000 [m/s] in 10 [m/s] steps

6) ***Storing interval:*** integer-wise varies the interval between stored profiles; variable by 40 [ms]

7) ***Trigger mode:*** sets whether the data acquisition is externally or manually triggered; Off or On modes

8) ***Auto record mode:*** sets recording mode for data, whether to HD or FD or to an external source; Off, Disk or Serial modes.

9) ***Emission voltage:*** sets the peak-to-peak voltage applied to the transducer; can be adjusted to compensate for lack of reflectors and/or attenuation within the medium; voltages are: 30, 60, 160 [V]

10) ***RF Gain factor:*** sets the approximately linear slope of amplification gain distribution over the 128 channels; can be set to compensate for apriori acoustic losses or to enhance the return signal; values are 0, 1, 2, 3

11) ***Screen scale factor:*** changes the velocity range of display; 1, 2, 3, 4

12) **Is this file OK? (Y/N):** simply asks whether data file and parameters as given are acceptable.

13) ***Doppler Coef.:*** appears when reviewing acquired data; the raw data that is recorded is in units of frequency detected during the measurement time. Thus the Doppler shift frequency can be calculated using the Doppler coefficient defined by, $C_{Doppler}=F_{prf}/(2x128)$.

14) ***Speed Coef.:*** appears when reviewing acquired data; converts data from frequency to speed from knowledge of the acoustic velocity as, $c_{speed}=c/2f$.

15) ***Velocity Conv.:*** product of 12) and 13), thus converting into [mm/s] units.

Appendix B:

Specifications of Expancel DU091-80 tracer particle

EXPANCEL®

Product Specification

Unexpanded Microspheres

EXPANCEL WU = Wet, Unexpanded microspheres.
Delivered as a wet-cake in fibre drums, net weight 70 kg.
EXPANCEL 820 also available as a 40 % slurry.

EXPANCEL DU = Dry, Unexpanded microspheres.
Delivered in fibre drums, net weight 50 kg.

EXPANCEL	Approx Solid Content % WU	Particle Size µm (1) (Weight Average Diameter)	ThermoMechanical Analysis (2) Tstart °C	Tmax °C	TMA-density kg/m³	Solvent (3) Resistance
820	65	10–16	75–80	115–125	< 25	*
642	67	10–16	84–90	125–133	< 17	**
551	65	10–16	93–98	135–143	< 17	***
551-20	63	6–9	93–98	129–137	< 25	***
551-80	63	18–24	93–98	138–148	< 20	***
461	60	9–15	98–104	137–145	< 20	****
461-20	60	6–9	98–104	133–141	< 30	****
051	65	9–15	106–111	138–147	< 25	****
053	75	10–16	95–102	137–145	< 20	***
053-80	75	18–24	95–102	140–150	< 17	***
091	70	10–16	118–126	161–171	< 17	*****
091-80	70	18–24	118–126	171–181	< 17	*****

(1) Technical Bulletin no 3
(2) Technical Bulletin no 5
(3) Technical Bulletin no 7

Issue 95.04

Expancel

Figures B-1 shows several typical attributes of Expancel powder, referred to as unexpanded micropheres. The powder is normally used in surface coating applications, so that the only specifications of relevance to us are the paricle size [µm]and temperature range. We have used Expancel DU091-80 in the present experiment which has a temperature range 130°-190°C.

Appendix C:

Table of documented photographs and video prints

Run Code	Number of jets	Average velocity	Film No.	No.	1st Expo. No.	End Expo. No.
J1E-02	1	1m/s	3746	1	2	4
NA			3747	2	2	12
NA	1	0.5	3747	2	13	24
J1E-01	1	0.5	3748	3	3	24A
J1E-02	1	1	3748	3	12	20
J1E-03	1	2	3748	3	20A	24A
J3E-02	3	1,1	3749	4	1	17
NA	3	1,0.5	3749	4	18	24
NA	3		3750	5	2	24
NA	3		4624	6	2A	24,E
NA	3		4623	7	1A	24,E
NA	3		4625	8	2	24
NA	3		4632	9	3	24,E
NA	3		4619	10	1A	24A,mu
NA	3		4622	11	1A	24A
NA	3		4621	12	2A	24A
J1E-01	1		0698			
J1E-02	1		0138		missing	
J1E-03	1		1060			
J3E-05	3		2048			
J3E-05	3		2377			
J3E-01	3		2585			
J3E-01	3		2588			
J3E-01	3		2594			
J3E-02	3		2897			
J3E-02	3		2926			
J3D-08	3		0053			
J3D-08	3		0064			
J3D-07	3		0510			
J3D-07	3		0536			
J3D-14	3		0898			
J3D-14	3		0946			
J3D-04	3		1282			
J3D-04	3		1299			
J3E-01	3	0.5,0.5	Sony print			
J3D-04	J1E-C; 3	0.5,0.5	Sony print	dT=5C		
J3D-07	J1E-B; 3	0.5,0.5	Sony print	dT=10C		
J3E-02	3	1.0,1.0	Sony print			
J3E-05	3	1.0, 0.5	Sony print			
J3D-08	J3E-B; 3	1.0,1.0	Sony print	dT=10C		
J3D-14	J3E-C; 3	1.0, 0.5	Sony print	dT=5C		

Table C-1. Documented list of photographs and video prints.

Appendix D:

A brief review of fundamental jet parameters

Jets, plumes and a combination of the two have been investigated for many years by various investigators. They have a wide range of applications and relevance in the engineering world. Here we use the terms "single-jet" and "triple-jet" in order to distinguish between the number of jets in our experiment. By a single jet we mean one fluid flowing into another at a different velocity than the "receiving" fluid which may be stationary or slowly flowing. A jet can naturally be injected vertically, horizontally or at some specific angle with respect to the receiving fluid. The two fluids can be of the same species (e.g. water-water), different species (water-oil) or even of different physical states (gas-liquid). There can also be a difference in density of the two fluids, due simply to one species jetting into a second species or in a thermally-stratified arrangement whereby a temperature (and therefore density) difference exists between the jet and receiving body of fluid. The results from a large number of investigations on jets, plumes and in this instance heated jets (a single-jet injected into a quiescent cold surrounding) have been compiled by Cheremisinoff [7]. We thus know from these studies that a number of parameters typically characterize (single) heated jets; that is, velocity and temperature (density) related parameters which appropriately describe the downstream change in the jet as compared to set entrance conditions. For example, three such parameters are the following: 1) U_o/U_m, a ratio of the entrance to centerline maximum average velocity, 2) $r_{1/2D}/D$, a ratio of the jet half-radius for velocity to the jet's characteristic nozzle diameter, and 3) $(T_o - T_\infty)/(T_m - T_\infty)$, a ratio of the initial temperature difference with respect to the ambient *to* the difference of the maximum with respect again to the ambient. We show in Figure E-1 a schematic diagram of a heated jet, its parameters and its coordinate system followed by, Figures E-2 to E-4, which show: 1) a plot of the axial decay of the centerline velocity and definition of velocity core length, 2) a plot of the axial variation of jet half-radius for velocity, and 3) a plot of the axial decay of the centerline temperature and definition of temperature core length.

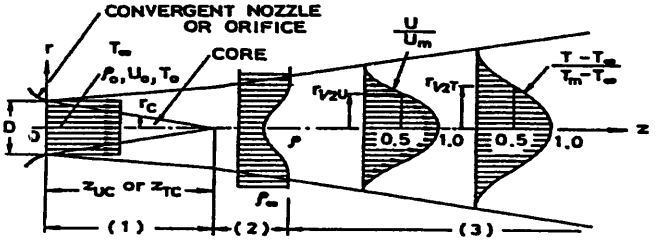

Figure 1. Schematic diagram of heated turbulent free jet and the coordinate system to be used: (1) potential core region, (2) transition region, and (3) fully-developed region.

Figure D-1 Schematic of heated jet, its parameters and coordinate system.

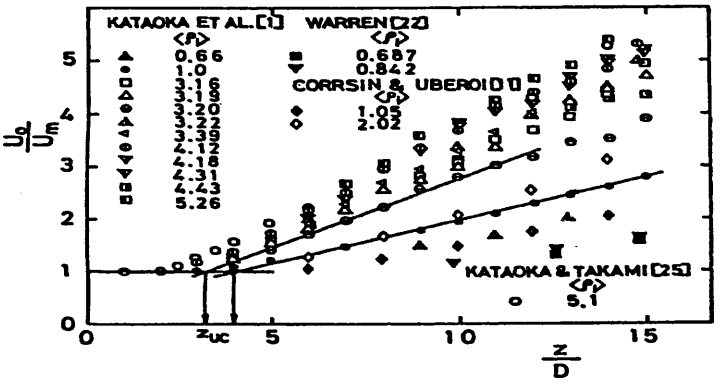

Figure D-2. Axial decay of centerline velocity and definition of velocity core length.

Figure D-1 schematically depicts the traditionally known (single) jet parameters. The jet is shown horizontally, but the jet parameters equally apply for a vertically-oriented flow. The jet initially at density, average exit velocity and temperature ρ_0, U_0, T_0 respectively flows from a nozzle fo diamter D with (r,z) coordinates as shown. The ambient temperature and density at T_∞ and ρ_∞ respectively, can of coures be other than T_0 and ρ_0. There are three flow regions: potential core, transition and fully-developed. The potential core region is defined by lengths, z_{UC} and/or z_{TC}, and radius r_c. The other parametes in the figuer are as follows: 1) ρ-density of the jet, 2) $r_{1/2U}$-the radius at which the jet velocity is one-half the centerline velocity (usually U_m), 2) $r_{1/2T}$-the radius at which the jet temperature is one-half the centerline to ambient difference (T_m-T_∞), 3) U/U_m-ratio of the velocity at r to maximum (centerline) and 4) $(T-T_\infty)/(T_m-T_\infty)$-ratio of the temperature at r to the difference, (T_m-T_∞).

Figure D-2 plots U_0/U_m versus the nozzle diameter no-dimensionalized axial distance, z/D. $<\rho_i>$ gives the ratio jet density to the density at the exit, ρ_0; thus $\rho_i > 1$ and $\rho_i < 1$ imply heated and cooled jets respectively. One can see the the ideal linearity in U_0/U_m versus z/D, beyond z_{UC}, as well the scatter and range of data.

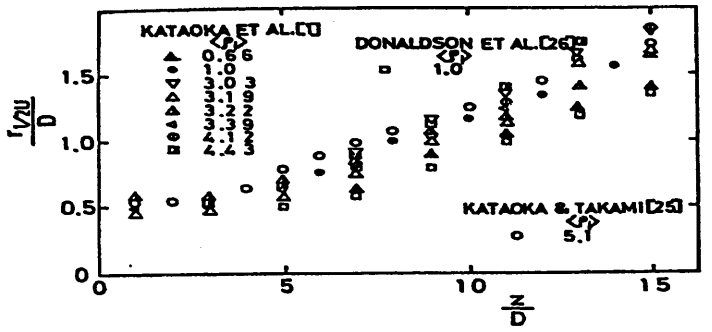

Figure D-3.Axial variation of jet half-radius for velocity.

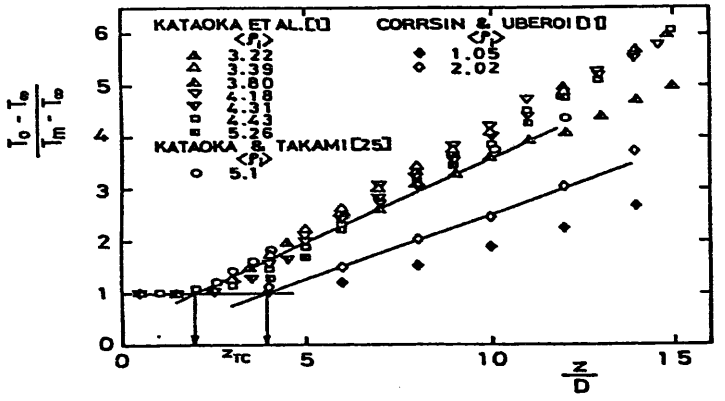

Figure D-4.Axial decay of centerline temperature and definition of temperature core length.

Figure D-3 shows the axial variation of the jet half-radius for velocity , $r_{1/2U}$, versus z/D. Here again the linearity in the data beyond z_{UC} is revelaed.

Figure D-4 depicts the axial decay of centerline temperature and definition of z_{TC} , in analogy to z_{UC} . This plot is only meaningful for non-isothermal jets and positive values; that is, for cases where both the numerator and denominator are positive or negative. So, implying that $(T_0-T_\infty)>0$ and $(T_m-T_\infty)>0$ *or* $(T_0-T\infty)<0$ and $(T_m-T_\infty)<0$.

Appendix E:

Appendix E: List and short description of test cases

*Single-jet trial data files

Case 3: J1E_R

Consists of 54 files, 2 files corresponding to each axial location and thus repeated. The axial distance corresponds to z=___ to ___. The specific UVP operational parameters are listed in App. A, Table A-1.

Case 4: J1E_R2

Consists of 78 files, 2 files corresponding to each axial location and thus repeated. The axial distance corresponds to z=___ to ___. The specific UVP operational parameters are listed in App. A, Table A-1.

Case 5: J1E_R3 and J1E_R4
The cases J1E_R3 and R4 consist of 68 and 90 files, respectively and correspond to an axial location above the exit nozzle. Each measurement at an axial location was repeated. The total axial distance traversed corresponds to z=0 to 390. The specific UVP operational parameters are listed in App. A, Table A-1. Generally, in contrast to J1E_R6 and R7, the UDV data here was taken over a larger span, some 668 mm across the jet (as compared to 360 mm). We thus refer to this data set as the "far-field".

A plot of the half-radius versus the axial distance is shown in Figure 17. The half-radius in this case was estimated from the data set using only the "positive" portion of the UDV signal containing both positively and negatively shifted, temporal Doppler components. By selectively filtering the mixed signal, a distinct positive or negative single-jet profile was obtained from which the half-radius could be estimated. The plot clearly shows a constant trend up to 3 diameters downstream of the nozzle, and a mostly linear trend up to 16 diameters.

Case 9: J1E_S1---T=30°C, V_{avg}=0.5 m/s; w-component of velocity from above.

Consists of 12 files, 2 files corresponding to each axial location and thus repeated. A single UVP transducer was placed facing vertically downward (for eaxmple see Fig. 30) at a 90° angle with respect to horizontal and thus measured the vertical velocity component of the single-jet.

Case 10: J1E_S2---T=30°C, V_{avg}=0.5 m/s; w-component of velocity from above.

Consists of 68 files, 2 files corresponding to each axial location and thus repeated.

Case 11: J1E_S3---T=30°C, V_{avg}=0.5 m/s; w-component of velocity from above.

Consists of 68 files, 2 files corresponding to each axial location and thus repeated.

*Triple-jet trial data files

Case 12: J3D_F1---T_{cold}=37-38°C, T_{hot}=42-43°C, ΔT_{hc}=5°C (target), V_{avg}=0.5 m/s; u-component of velocity from above, TDX at 0° orientation from the side.

Case 17: **J3E_F1**---T_{cold}=30°C, T_{hot}=30°C, ΔT_{hc}=0°C (target), V_{avg}=0.5 m/s; u-component of velocity from above, TDX at 0° orientation from the side.

Case 18: **J3E_S1**---T_{cold}=T_{hot}=30°C, ΔT_{hc}=0°C, V_{avg}=0.5 m/s; w-component of velocity from above, center jet only

III.3.4 Miscellaneous

Case 19: Work: no details are known.

Case 20: Work2: no details are known.

Figure E-1 on the following pages shows the case names of the UVP case name placed upon a simplified schematic of the flow configuration. The dark arrows indicate the direction of the ultrasound beamline while the position of the "boxed" case names indicate the right or left placement of the transducer. Additionally, if the transducer was at an angle with respect to the horizontal, this is given as "angle=" .

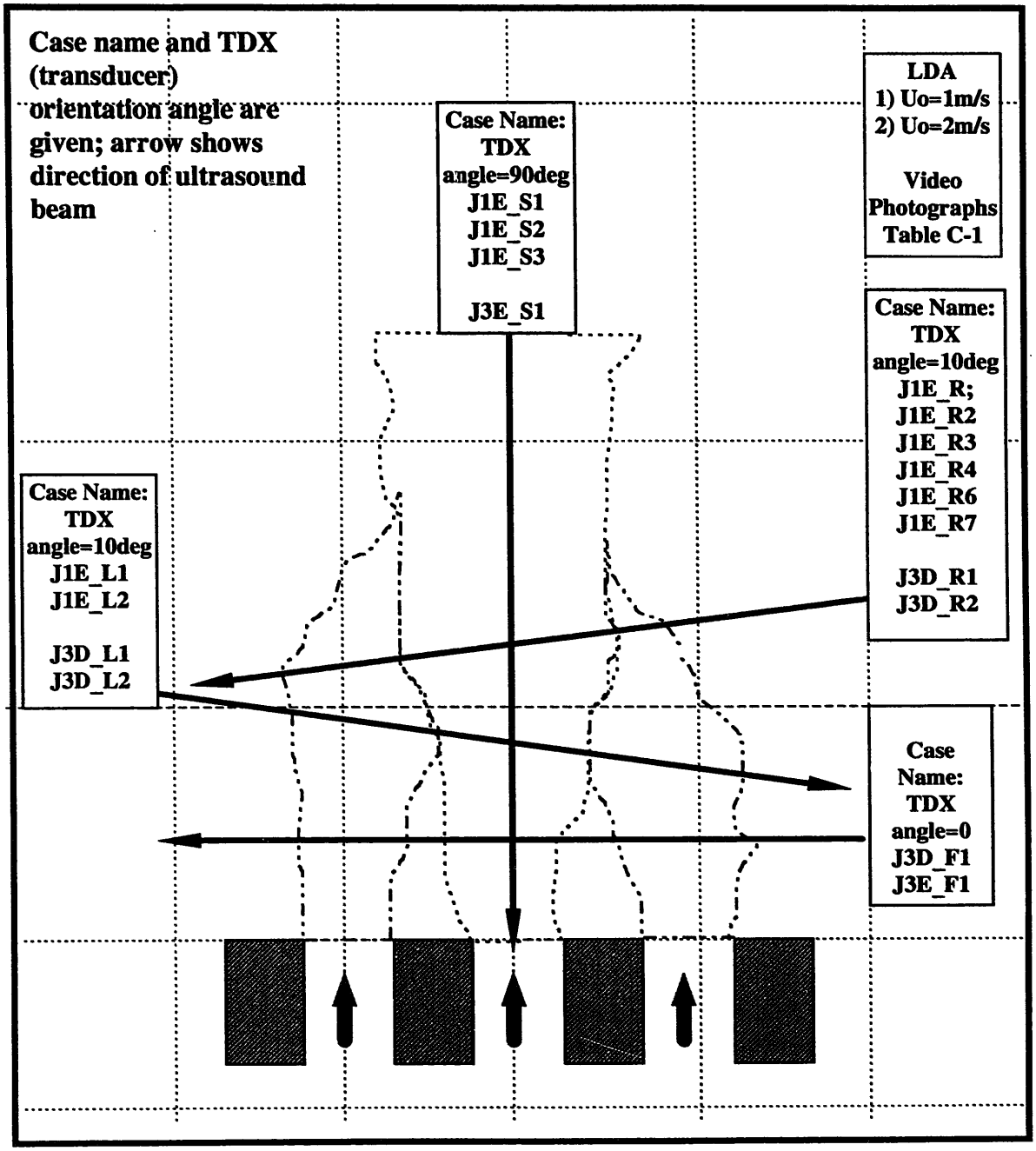

Figure E-1. Case Names of UVP data files with respect to the flow configuration.